Spring 2023

A PRIMAL TREATISE OF CONSTANT-FORCE COMPLIANT SEGMENT AND MECHANISM DESIGN WITH APPLICATIONS

Vamsi Lodagala
Missouri University of Science and Technology

A PRIMAL TREATISE OF CONSTANT-FORCE COMPLIANT SEGMENT AND

MECHANISM DESIGN WITH APPLICATIONS

by

VAMSI LODAGALA

A DISSERTATION

Presented to the Graduate Faculty of the

MISSOURI UNIVERSITY OF SCIENCE AND TECHNOLOGY

In Partial Fulfillment of the Requirements for the Degree

DOCTOR OF PHILOSOPHY

in

MECHANICAL ENGINEERING

2023

Approved by:

Dr. Ashok Midha, Advisor
Dr. Lokeswarappa R. Dharani
Dr. K. Chandrashekhara
Dr. Xiaoping Du
Dr. Edward Kinzel

ABSTRACT

The evolution of compliant mechanisms propelled the development of constant-force mechanisms (CFMs) for various applications because of their unique characteristics. Many research endeavors have presented different techniques that often involve some optimization to design the CFMs. However, the mechanics of the generation of constant force at the elemental level is not well understood. This research effort theorizes and validates that simple, compliant segments with different boundary conditions, subjected to axial loading, produce near-constant force without the need for design optimization. Analytical models are developed based on the pseudo-rigid-body model (PRBM) concept to predict their force-displacement behavior, and to establish that beams exert constant force in their post-buckling stage. The results are validated experimentally for these rudimentary compliant segment types, which exemplify that they are the very kernel for generating constant load by CFMs. With this premise, an investigation is conducted on the design of a novel compliant mechanism, the Canted Spring. A type synthesis of the canted spring identifies eight possible configurations. The PRBM concept, along with the virtual work principle, is utilized to predict their force-displacement behavior, as well as for dimensional synthesis. They exhibit nonlinear force-displacement characteristics, with two configurations showing the best potential for exerting constant load; these are optimized to produce more exact constant force. A methodology is formulated to help design a canted spring from these optimized mechanisms. CFM systems, i.e., modular units and array structures, are developed with examples for high load-bearing and uniform pressure distribution applications.

ACKNOWLEDGMENTS

TABLE OF CONTENTS

LIST OF ILLUSTRATIONS

LIST OF TABLES

NOMENCLATURE

Symbol	Description
l, L	Length of Compliant/Flexible (or Rigid) Segment
R_i	Initial Radius of Curvature f Compliant Segment
O	Origin and Characteristic Pivot Point on Beams
I	Area or Second Moment of Inertia
E	Modulus of Elasticity or Young's Modulus
K	Equivalent Torsional Spring Stiffness for Beam's Resistance to Bending
P	Transverse load at beam end
nP	Axial load at beam end
n	Load factor
F	Resultant force at beam end
ξ	Compliant- to rigid-segment length ratio
ϕ	Angle of resultant force on beam
θ_0	Beam end angle
Θ	Pseudo-rigid-body beam-end angle
Θ_i	Initial Beam-End Angle
γ	Characteristic Radius Factor
Δ, δ_y	Deflection
K_Θ	Stiffness Coefficient
w	Width of Compliant Segment
t	Thickness of Compliant Beam

P_{cr}	Euler's critical load for Buckling
η_c	Characteristic Load Factor
N	Normal Force
F_f	Frictional Force
σ_{cr}	Crtical Stress by Johnson's Formula
E_y	Eccentricity of the ground pin-joint from the slider base level
α	Constancy Ratio

1. INTRODUCTION

1.1. COMPLIANT MECHANISMS

This research endeavor is on the design and analysis of compliant constant-force segments and mechanisms. For facilitating a better understanding of the work presented in the dissertation, a brief introduction to compliant mechanisms and constant-force mechanisms is provided in this section. History and evolution of compliant mechanisms along with the nomenclature developed to design and analyze them are discussed below.

1.1.1. Definition and History. Compliant mechanisms are mechanical devices that gain some or all of their mobility from the deflection of their flexible members to transfer motion, force, or energy [1, 2]. The longbow and catapult used as hunting tools in ancient history could be well regarded as classic examples of compliant mechanisms, where the energy is stored in its flexible members when drawn and is provided at release. Compliant mechanisms integrate the form with function and typically necessitate large deflections to perform like the rigid-body mechanisms for the intended function(s). In fact, the rigid-body mechanisms can easily be converted into compliant mechanisms by replacing one or more rigid links/bodies with flexible members for their inherent advantages (discussed in the following sections). A few examples of compliant mechanisms/devices for a variety of applications are shown in Figure 1.1.

The compliant fishhook remover, also known as Compliers®, is a single-piece injection molded design equivalent to traditional fishhook remover [3]. The compliers® utilize the stored energy in the flexible link when deformed. This tool is more economical and beneficial than metal design (pliers) due to its simplicity in design and resistance to

corrosion. The SMINT® mint dispenser [4] in Figure 1.1 has a compliant segment that acts as a return spring to retract the plunger, which is a single-piece injection molded part, back to its initial position after dispensing a mint. It also provides sufficient reaction force to the user and ensures smooth motion with no noise while being operated.

(a)   (b)

Figure 1.1 (a) Compliant Fishhook Remover [3] (b) SMINT® Mint Dispenser [4].

1.1.2. Advantages and Challenges. There are many advantages for compliant mechanisms over the rigid-body mechanism because of reduced complexity in both design and manufacturing. The following are a few advantages:

- Reduced Part Count: as the flexible segments replace the springs and joints of the equivalent rigid-body mechanism

- Ease of Manufacturing and Assembly: fewer parts lead to simple manufacturing processes and fewer assembly steps

- Weight Reduction: due to the reduced total number of components with simpler or monolithic designs, the product's total weight can be minimized to a greater extent when compared to rigid-body mechanisms

- Cost Reduction: due to fewer parts, less material usage, simple designs, and reduced assembly time, the price of production will be much cheaper in comparison

- Improved Precision: due to no lash and reduced wear

- Improved Performance: due to no shock, energy storage, and no noise

- High Reliability: due to increase precision and performance

- Low Maintenance: no lubrication is needed

- Miniaturization of components: achieved with advanced manufacturing processes

Despite these advantages, there are a few challenges and disadvantages to compliant mechanisms due to the highly nonlinear nature of their large deflections and the use of plastics in their construction for plenty of applications, as listed below.

- Traditionally, the biggest challenge is the relative difficulty in analyzing and designing them for large deflections – however, several modeling techniques have been developed to overcome this issue

- Low fatigue life and creep due to large deflections of its flexible members, especially for the devices manufactured with polymers – recent development of integrating metal strips within the polymer beams addresses these issues, as shown in studies conducted by Kuber [5] and Crews [6]

- Replacing or repairing defective/deformed members of a compliant mechanism is often challenging and might lead to the disposal of the entire unit, as they are generally designed as integrated parts – often it is rare and inexpensive

1.1.3. Applications and Examples. Several applications implemented compliant mechanisms design successfully in diverse fields of engineering. A few of them are demonstrated in the following figures. Figure 1.2 illustrates compliant tires, which are

Flexure Wheels for NASA's Mars Exploration Rovers [7] and Michelin Tweel Airless Tires [8] for automotive applications. Figure 1.3 presents consumer products, Adidas® Springblade Shoes [9] for good comfort and support for runners, esp. in their recovery runs, and Flight Flexor® Footrest [10] for long flights to avoid numb feet and swelling.
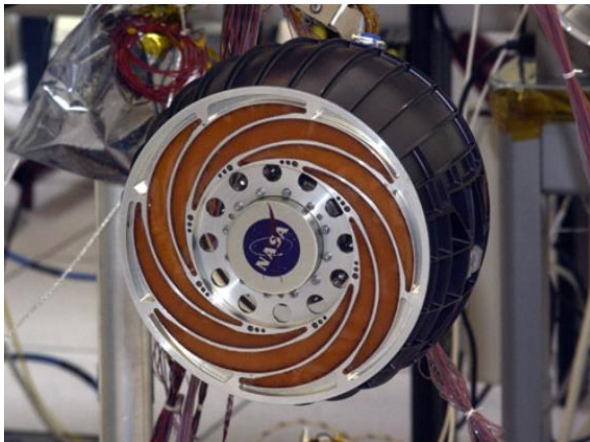
(a)   (b)

Figure 1.2 (a) NASA Mars Rover Wheels [7] (b) Michelin Tweel Airless Tires [8].

(a)   (b)

Figure 1.3 (a) Adidas® Springblade Shoes [9] (b) Flight Flexor® [10].

Another example is a compliant chair designed by Mettlach and Midha [11], where the flexible legs store energy and provide the user with extra support to egress. Also, it allows the chair to recline such that it provides an ergonomic posture position for better comfort, as shown in Figure 1.4. Flex-Foot Cheetah [12, 13], a prosthetic foot replacement design made with carbon fiber, depicted in Figure 1.4, for physically disabled people. This prosthetic foot can be helpful for them in performing day-to-day activities and sports, as it absorbs shock while running/walking and releases it for furthering their motion.

(a)   (b)

Figure 1.4 (a) Compliant Chair [11] (b) Ossur® Cheetah Blade [12, 13].

Bio-medical devices also have seen significant implementations of compliant mechanisms. A flexible spinal disc replacement designed to provide the natural movement of the spine in any direction is one of many examples. Figure 1.5 describes the spinal disc developed at BYU [14] to provide more natural movement and mimic the spine motion in six different directions. Halverson et al. [14] developed this disc out of titanium strips for improved life performance.

Other examples of medical devices are Trocar surgical tool developed by Nikolai Begg [15], which uses flexible members to accomplish precise motion during surgical procedures, and the compliant suturing instrument developed by Cronin et al. [16] for performing minimally invasive surgeries, which are illustrated in Figure 1.6.
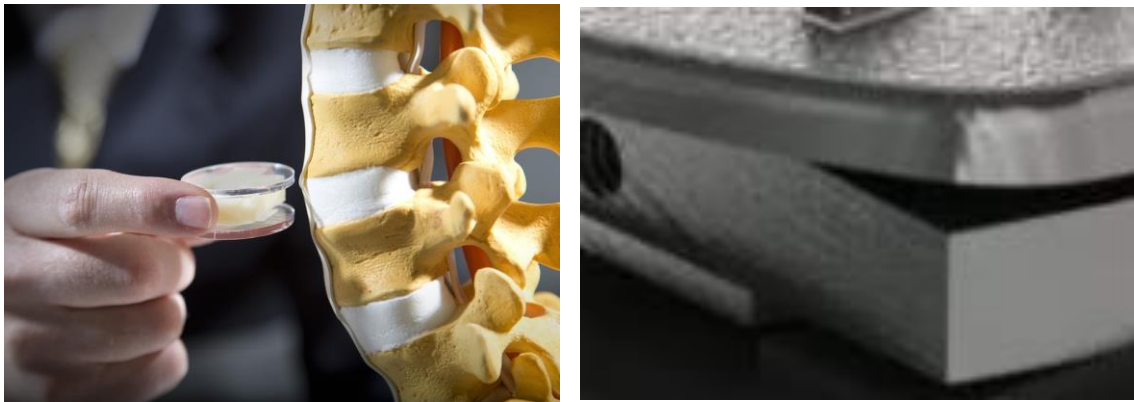
(a)   (b)

Figure 1.5 Artificial Spinal Disc Replacement – a) Prototype, b) Titanium Disc [14]

(a)   (b)

Figure 1.6 (a) TROCAR® Surgical Tool [15] (b) Compliant Suturing Instrument [16].

AMP Inc. has designed a few compliant tools for various applications, and a couple of them are presented in Figure 1.7, such as a compliant crimping tool and chip carrier extractor to reduce the cost of the tool and increase their precision and performance.

The abundant advantages of compliant mechanisms have also been useful in developing Microelectromechanical Systems (MEMS). It includes micro actuators, micro sensors, micro bistable mechanisms, electrical connectors, switches, self-closing gates, and product enclosures are good examples of compliant bistable mechanisms design.
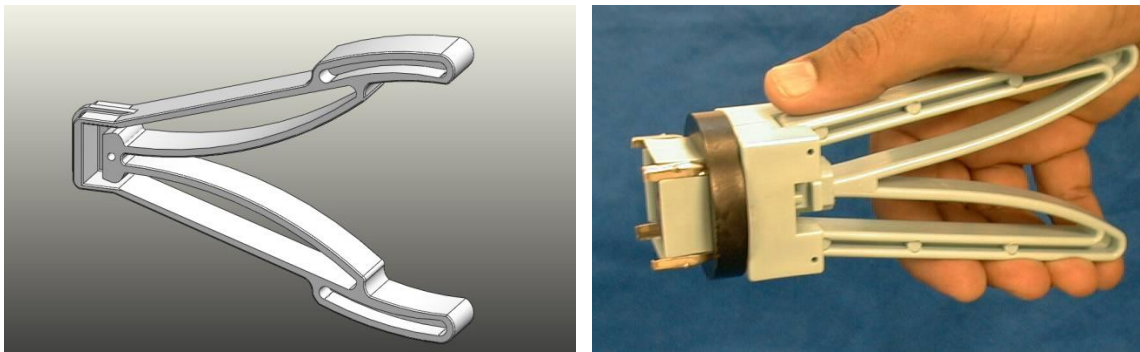
(a)   (b)

Figure 1.7 AMP Inc's (a) Compliant Crimping Tool (b) Chip Carrier Extractor [17].

Compliant mechanisms can also be found in the automotive sectors such as seating and suspension designs. The development of constant-force mechanisms is one of the prevalent areas where compliant mechanisms are successfully implemented. Their applications and history are further discussed in detail in section 1.2.

1.2. CONSTANT FORCE MECHANISMS

This section briefly reviews the history and current state-of-art of CFMs.

1.2.1. Definition and Evolution. A *constant-force spring* or *mechanism* may be defined as a device that exerts a constant or near-constant force over its entire or partial range of motion [18]. The evolution of constant-force mechanisms (CFMs) is propelled by a growing interest in the ability to exert constant or near-constant force for various applications. Compliant mechanisms have recently received much attention in the design of CFMs because of their unique characteristics, such as fewer parts, compact construction, natural energy storage, no backlash, etc.

One of the early inventions was the constant-force tension spring, also known as the "Neg'ator" spring [18, 19]. It is a pre-stressed strip of flat spring stock that is coiled around bushing or successive layers on itself. It is also worth noting that a certain arrangement of Belleville spring can produce a near-constant load over a portion of its deflection. Such constant-force springs have been around for a while and can be found in several day-to-day applications, e.g., inertia-reel seat belts, tape measures, and pull starts [20]. However, these springs have a few limitations, such as their inability to exert a constant force over a significant range of motion, unable to generate higher magnitudes of force and their intricate construction.

1.2.2. Current Methodologies to Design Constant-Force Mechanisms. There have been many research efforts in developing various techniques to design constant-force mechanisms for applications in diverse fields. Some of the pioneering efforts in constant force are instigated by Nathan [19] and Jenuwine and Midha [21, 22] in the development of rigid-body constant-force mechanisms. Nathan [19] developed a chain of four-bar-parallelogram, hinged-lever mechanisms with linear springs that exerted a constant, unidirectional force for any position. Jenuwine and Midha [21, 22] ushered a path to

synthesize a rigid-body, constant-force mechanism with two orthogonally placed linear springs by using the extension of the loop-closure method. A single-input port and multiple-output port (SIPMOP) mechanism configuration is used for specified energy absorption with displacement or a constant force value, leading to the design of an exact constant-force generating mechanism. A SIPMOP [21, 22], as shown in Figure 1.8, is a multi-loop mechanism with seven rigid links and two linear extension springs that has one degree of freedom. The two orthogonal springs of this bisymmetric mechanism with the same spring constants generate constant force.

Figure 1.8 SIPMOP Constant Force Mechanism [21, 22]

An accelerated pavement testing machine was developed at Purdue University based on the SIPMOP mechanism, as shown in Figure 1.9, to exert a constant nine-ton load with a super-single tire on the pavement aggregate under test [23]. It also shows the scaled

prototype of the mechanism. The force-displacement response of the pavement testing machine is presented in Figure 1.10.
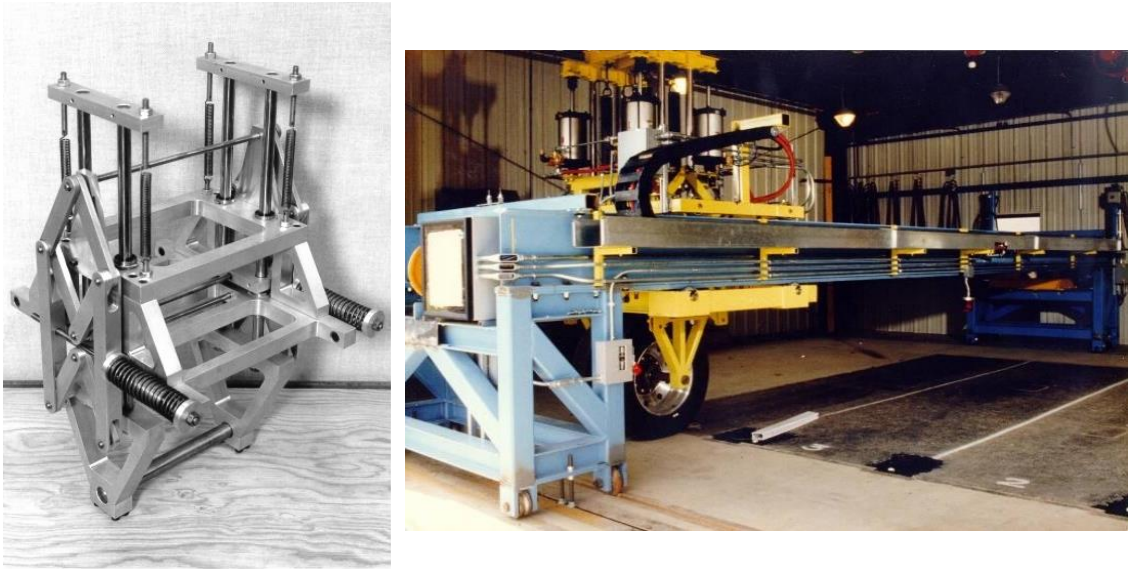
Figure 1.9 Accelerated Pavement Testing Machine at Purdue University [23]

Murphy [24] and Murphy, Midha, and Howell [25] have presented the design of one of the first compliant constant-force mechanisms (Compliant CFMs), which is based on the SIPMOP CFM. The type-synthesis methodology was employed to develop all the possible arrangements of the compliant CFM. Howell [26] and Howell, Midha, and Murphy [27] have modeled this compliant CFM using the pseudo-rigid-body model (PRBM) technique as a slider-crank mechanism with torsional springs. For several of the configurations of the compliant CFM, dimensional synthesis optimization was conducted to determine their PRBM parameters for the generation of constant force. This work has established the guidelines to design and develop compliant CFMs. Midha et al. [28] have presented all possible configurations of the compliant slider-crank CFMs, along with an

application for an electric connector. These configurations have a variety of compliant segment types for the slider-crank-based compliant constant-force mechanisms, and one such is presented in Figure 1.11.
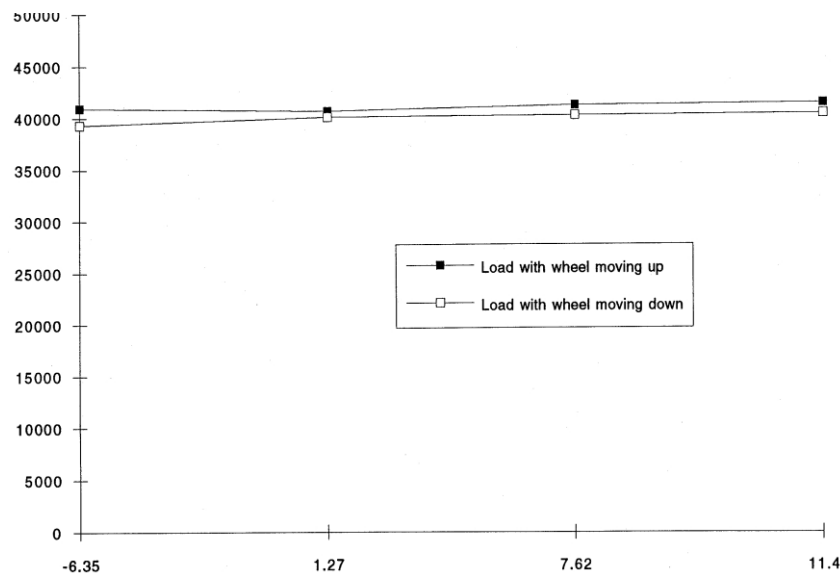
Figure 1.10 Force-Displacement Behavior of Accelerated Pavement Testing Machine [23]

Furthermore, several other design techniques [29-41] have been developed, which are either based on the pseudo-rigid-body model or topology optimization for developing compliant constant-force mechanisms. Some of these techniques were also for analyzing the dynamic behavior of the CFMs.

1.2.3. More Examples of Compliant CFM Applications. In more recent times, a growing interest in compliant CFMs has led to the furtherance of such mechanisms for various applications in diverse fields [42-63]. Constant-force end-effector mechanism designed by Evans and Howell can be used where the position control is not adequate, i.e.,

the work surface is varying, illustrated in Figure 1.12 [42]. Nahar and Sugar [45] developed a compliant constant-force mechanism with a variable output for micro/macro applications. A substantially constant-force exercise machine is designed by Howell and Magleby [47] that exerts constant force throughout the exercise, even during space travel, as shown in Figure 1.13. A compliant constant-force mechanism was designed for an adaptive robot end-effector operation by Lan et al. [48].
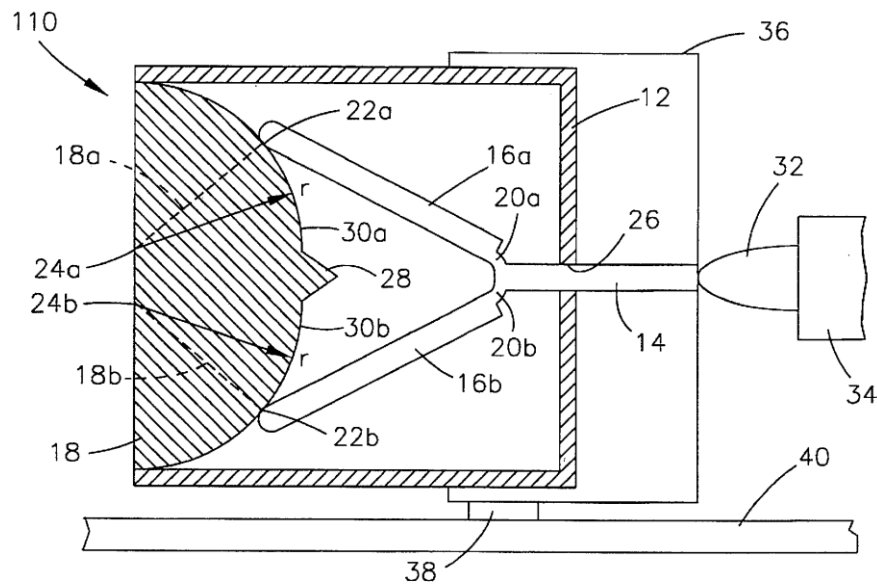
Figure 1.11 Compliant Constant-Force Mechanism with a Cam [28]

Pham and Wang [49] developed a constant-force bistable mechanism for force regulation and overload protection that can snap to its other stable equilibrium state to protect the device if the force exceeds its limit. Compliant constant-force micro-mechanism for enabling dual-stage motion for nano-injection, which delivers DNA into mouse zygotes, was developed by Zirbel et al. [52]. Parlaktaş designed a compliant constant-force mechanism for spatial applications [53].

Figure 1.12 Constant-Force Robot End Effector [42]

Figure 1.13 Constant-Force Exercising Equipment [47]

Karthik worked on the design of a nearly constant-force modular device based on a compliant slider mechanism for ease of use of CFMs [54]. Liu et al. [56] designed an adjustable cam-based constant force mechanism, where the constant force magnitude can be regulated by preloading the linear spring. Lambert and Herder designed an adjustable constant-force mechanism using pin joints and springs for reducing the effects of joints' friction on the quality of constant force, which may be miniaturized for medical applications [58].

Liu, Zhang, and Xu [59] designed a novel compliant constant-force gripper based on buckled fixed-guided beams. A load-adjustable constant-force mechanism was also developed by Hasara and Lusk [60] by introducing a second degree of freedom in the compliant crank-slider mechanism that allows for the rotation of the compliant beams as needed to alter their stiffness for adjustment to a specific range of constant output force. Jute [63] developed a generalized synthesis of nonlinear spring and designed a constant force spring based on it for space applications, as illustrated in Figure 1.14.

1.3. SCOPE OF THE INVESTIGATION

Many of the current techniques often require some level of design optimization in the mechanism synthesis to produce constant force over a desired yet limited range of motion. However, the mechanics of the generation of constant force is still not well understood at the elemental level, despite the advancements in the development of constant-force mechanisms (CFMs). This research theorizes and presents a vital principle that simple, compliant segments under axial loading are capable of generating constant force irrespective of their shape and size without any need for design optimization.
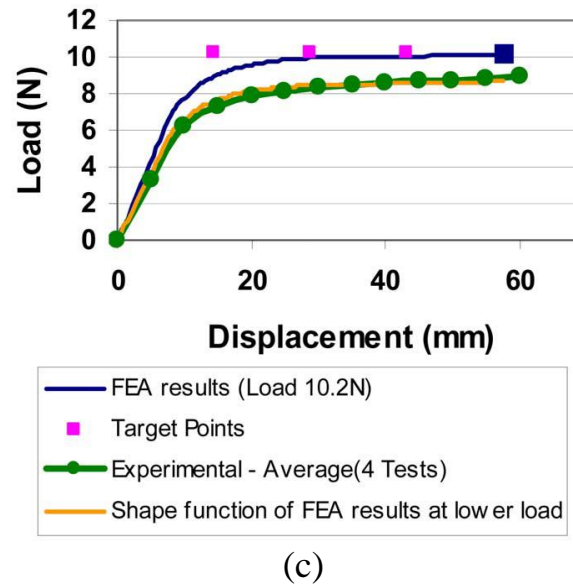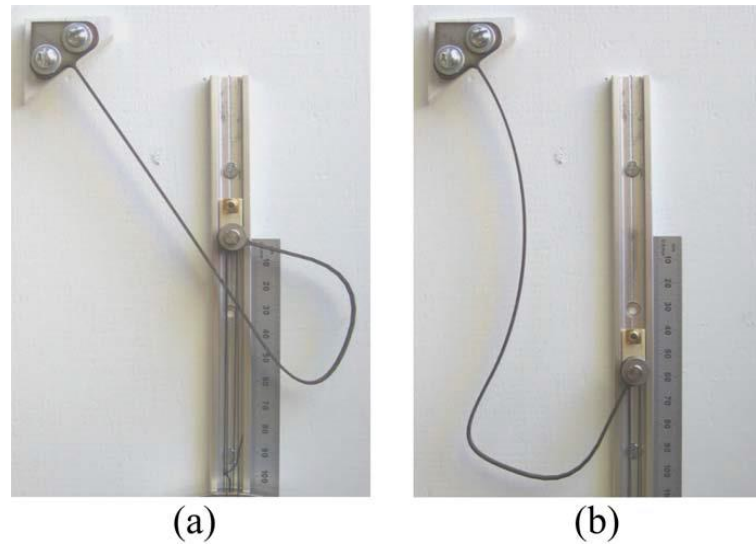
Figure 1.14 Nonlinear Spring to Generate Constant-Force [35, 63]
(a) Undeformed, (b) Deformed, (c) Resultant Load-Displacement Plot

This work demonstrates that various compliant beam types exert near-constant force over their significant range of deflection when subjected to axial loading, without the need for any optimization. The compliant segment types considered herein are fixed-free, pinned-pinned, and fixed-guided beams, along with a compound-compliant segment with a small-length-flexural pivot (SLFP) and a rigid-link system are investigated to determine

the mechanics of the generation of constant force. The force-characteristic behavior of the compliant beams is predicted by the analytical models that are developed by using the pseudo-rigid-body model (PRBM) approach [1-2, 26, 64-71]. The PRBM-based models establish that the beams exert constant force in their post-buckling stage.

The research endeavor commences by inspecting the fixed-free compliant beam under axial-compressive loading, and a model is developed using the PRBM technique to analyze its force-deflection characteristics. Likewise, the analytical models of pinned-pinned, fixed-guided compliant beams are also developed using the PRBM approach. Similar models are presented for the compound-compliant segment with an SLFP and an arrangement of rigid-link with a torsional spring to demonstrate their constant-force characteristics when subjected to axial loading. The theoretical results for the three rudimentary segment types are experimentally validated to accentuate that they exert constant force in their post-buckling stage. Additionally, this research exemplifies that the proposed theory is the very kernel for the generation of constant force by the existing CFMs.

A design and analysis of a novel compliant mechanism, a canted spring, is investigated in the context of constant force with the premise of the proposed theory. All the possible configurations of the canted spring are derived with a formalized type synthesis methodology. Two of them are identified to have the best potential to produce constant force, as they can have compliant segments under axial loading conditions. The PRBM concept and virtual work principle are utilized to predict their force-displacement behavior. Canted springs are determined to exhibit nonlinear force-displacement characteristics, with two configurations exerting near-constant force when their only

compliant beam is subjected to axial loading. Dimensional synthesis is developed for optimizing them to generate more exact constant force. A methodology is formulated to help design a constant-force canted spring from these optimized mechanisms.

CFM systems, i.e., modular units and array structures, are developed to serve high load-bearing and uniform pressure distribution applications. Design methodologies are presented to develop desired modular units and array structures with examples.

2. MODELING OF COMPLIANT MECHANISMS

2.1. INTRODUCTION

Compliant mechanisms profoundly rely on the deflections of their flexible members. The flexibility of members in traditional structural systems or rigid-body mechanisms is generally not desired to maintain its stability. For example, flexibility in high-speed machines causes vibrations leading to mechanical failure. Similarly, deflections are always undesirable in structures such as bridges and buildings. Hence, kinematic analysis of rigid-body mechanisms assumes that the links are rigid and that the deflections are small. The same assumption is valid for structural applications where the stresses are under the elastic limit. These small deflections in the members are predicted by Bernoulli-Euler equations, which are linear in nature. However, large deflections of compliant mechanisms cannot be solved by using these linear equations. So, several techniques have been developed to study the large-deflection behavior of compliant segments: This section briefly reviews small and large deflection analyses of the various beam types.

The Bernoulli-Euler equation states that the bending moment of the beam at any point is proportional to its curvature [26, 65, 71].

$$\mathrm{M} = EI\frac{d\theta}{ds} \tag{1}$$

where, M is the bending moment, E is the modulus of elasticity, I is the area moment of inertia, and $d\theta/ds$ denotes the change in angular deflection along the curvature of the beam.

$$\frac{d\theta}{ds} = \frac{d^2y/dx^2}{\left[1 + \left(dy/dx\right)^2\right]^{3/2}} \tag{2}$$

The slope (*dy/dx*) for small deflections is minute, therefore, its square term in the denominator of Equation 2 is assumed to be negligible. Now, the simplified Bernoulli-Euler equation is represented as follows.

$$M = EI\frac{d^2y}{dx^2} \tag{3}$$

For the large deflections of flexible segments, which introduce geometric nonlinearity, the assumptions of small deflections are not pertinent. If, however, utilized, it results in an error in the beam end locations. Hence, the appropriate methods for the design and analysis of compliant segments and mechanisms are discussed in the following sections.

2.2. CLOSED-FORM ELLIPTIC INTEGRALS

It is a classical method for solving nonlinear, large-deflection beam equations. Bisshopp and Drucker [72] have developed the initial formulations for large deflections of cantilever beams. Although this approach provides exact solutions, the derivations are complicated to use for the design and analysis of compliant segments, even when subjected to simple boundary conditions. Hence, they are only valuable for benchmarking purposes.

The methodology and closed-form elliptic integral equations for initially-straight and initially-curved compound compliant beams with small-length flexural pivots (SLFP) are demonstrated in section 3.

2.3. THE PSEUDO-RIGID-BODY MODEL (PRBM)

The pseudo-rigid-body model (PRBM) approach models the deflection of compliant members using rigid-body components such that the beam-end location is within a small acceptable error [1]. A simple, compliant fixed-free beam is modeled as two rigid members connected at a pin joint, also referred to as a characteristic pivot, shown in Figure 2.1. The beam's resistance to bending is represented by a torsional spring at the pivot (spring constant K), which has the equivalent force-deflection characteristics.

The elliptic-integral equations for large deflections compute that the compliant cantilever beam's end follows a near-circular path. Accordingly, the PRBM developed by Howell and Midha [67, 68] assumes two rigid links connected at a pivot to accurately model the near-circular path. The rigid-body link lengths are calculated using a *characteristic radius factor*, γ, which is a function of the load factor n, i.e., the ratio of the axial force, nP, to the transverse force, P. The product of γ and beam length, *l*, is the characteristic radius of the circular path traced by the end of the pseudo-rigid-body link, γ*l*, which is also its length. The factor, γ, is evaluated such that the error in the beam-end location predicted by the PRBM is within 0.5% of the coordinates provided by the elliptic integral formulation [67-69].

The modified PRBM parameters, i.e., the characteristic radius factor (γ), the parametric angle coefficient (c_θ), and the beam stiffness coefficient (K_θ) developed by Pauly and Midha [73], are presented below.

$$\gamma = \begin{cases} 0.855651 - 0.016438n, & -4 < n < -1.5 \\ 0.852138 - 0.018615n, & -1.5 < n \le 0.5 \\ 0.851892 - 0.020805n + 0.005867n^2 - 0.0000895n^3 \\ \quad +0.000069n^4 - 0.000002n^5, & 0.5 < n \le 10 \end{cases} \tag{4}$$
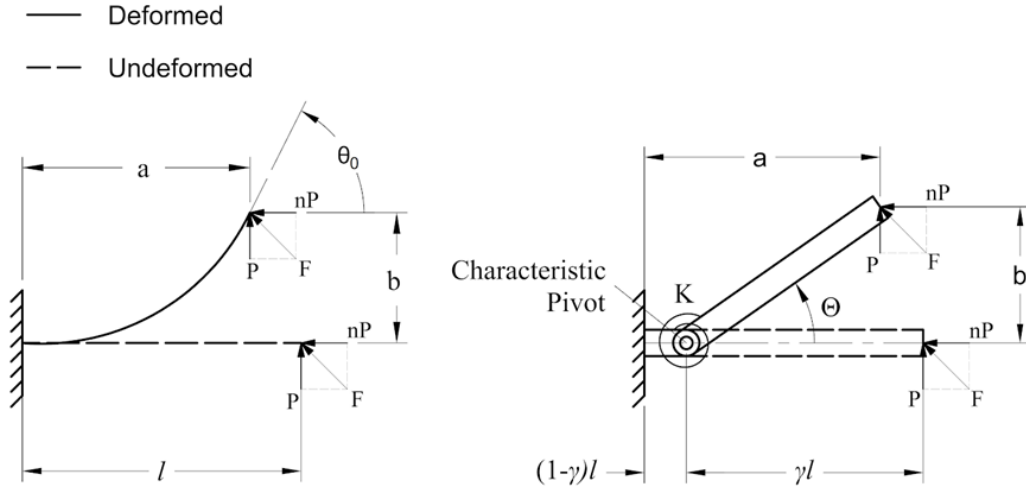
Figure 2.1 A Fixed-Free Compliant Beam and Its Corresponding PRBM [68].

$$c_\theta = \begin{cases} 1.238945 + 0.012035n + 0.00454n^2, & -4 \leq n \leq -0.5 \\ 1.238945 + 0.009113n - 0.001929n^2 + 0.000191n^3 \\ \quad -0.000007n^4, & -0.5 < n \leq -10 \end{cases} \qquad (5)$$

$$K_\theta = \begin{cases} 2.660461 + 0.069005n + 0.002286n^2, & -4 \leq n \leq -0.5 \\ 2.648834 - 0.074727n + 0.026328n^2 - 0.004609n^3 \\ \quad -0.00039n^4 - 0.000013n^5, & -0.5 < n \leq -10 \end{cases} \qquad (6)$$

where,

$$n = \frac{-1}{\tan \Phi} = \frac{nP}{P} \qquad (7)$$

The torsional spring constant and the parametric angle coefficient are computed respectively using Equations 8 and 9.

$$K = \gamma K_\theta \frac{EI}{l} \qquad (8)$$

$$\theta_0 = c_\theta \Theta \qquad (9)$$

The nondimensionalized transverse load index, which remains orthogonal to the beam throughout its deflection, is determined as follows,

$$(\alpha^2)_t = \frac{F_t l^2}{EI} \tag{10}$$

$$\text{and } \eta = \sqrt{1 + n^2} \tag{11}$$

where, F_t is the force tangential to the path of the beam end and is perpendicular to the pseudo-rigid link

$$F_t = F \sin(\Phi - \Theta) = \eta P \sin(\Phi - \Theta) \tag{12}$$

The beam end coordinates (a, b) of the deflected position and its pseudo-rigid-body angle are determined as follows.

$$a = l - \gamma l (1 - \cos \Theta) \tag{13}$$

$$b = \gamma l \sin \Theta \tag{14}$$

$$\Theta = \tan^{-1} \frac{b}{a - (1 - \gamma)l} \tag{15}$$

More recently, Midha et al. [74] improved the expressions for the stiffness coefficient (K_θ) as a function of the load factor (n) and the pseudo-rigid-body angle (Θ). The equations for compressive (positive) load factor and tensile (negative) load factor are presented below, respectively, which resulted in a significant improvement in the prediction of the beam end.

The PRBM concept demonstrated that this approach is simple, efficient, and accurate for modeling a variety of standard-compliant segment types: small-length flexural pivot (SLFP), fixed-free/pinned, pinned-pinned, and fixed-guided segments [65, 67-71].

$$K_\theta = \frac{1}{\Theta}(0.004233 - 0.012972n + 2.567095\Theta - 0.003993n^2$$

$$+ 0.037173\Theta^2 - 0.000297n^3 + 0.117997\Theta^3$$

$$+ 0.034678n\Theta + 0.003467n^2\Theta - 0.00947n\Theta^2)$$

$$for\ 0 \le n \le 10\ and\ 0 \le \Theta \le 65°$$

.   (16)

$$K_\theta = \frac{1}{\Theta}(0.000651 - 0.008244n + 2.544577\Theta - 0.004764n^2$$

$$+ 0.071215\Theta^2 - 0.000104n^3 + 0.079696\Theta^3$$

$$+ 0.006927n\Theta + 0.061507n^2\Theta - 0.347588n\Theta^2)$$

$$for\ -4 < n < 0\ and\ 0 \le \Theta \le 0.8\Phi$$

.   (17)

The key benefit of the use of the PRBM approach is modeling the compliant mechanisms as equivalent rigid-body mechanisms with characteristic compliance (springs), which enables the wealth of existing rigid-body mechanism analysis and synthesis knowledge to the treatment of compliant mechanisms. Hence, the PRBM is a valuable tool in the early design phases of compliant mechanisms as it provides the designer with a better understanding of designing them. Henceforth, the research effort will be utilizing the PRBM concept in the development of compliant constant-force mechanisms. The pseudo-rigid-body models of other relevant segment types are discussed in the respective sections.

2.4. CHAIN ALGORITHM AND FINITE ELEMENT ANALYSIS

Nonlinear finite element methods are common numerical alternatives to elliptic-integral solutions, and many commercial software programs are widely available. It

discretizes the beam into multiple segments, and appropriate boundary conditions are applied at each segment to evaluate the beam-end deflection. The chain algorithm, proposed by Midha, Her, and Salamon [75, 76], is a similar numerical procedure for the design and analysis of compliant mechanisms but uses a different technique to combine and solve the resulting equations for more efficient computations. However, designing compliant devices by both these approaches is an iterative process and hence best used for validating the solutions.

2.5. TOPOLOGY/STRUCTURAL OPTIMIZATION

The topology and structural optimization techniques [77-80] use the homogenization method. These approaches optimize the distribution of material or the size and shape of the continuum to satisfy the force-deflection constraints. Given the nature of this approach, it is not very useful for establishing design guidelines.

3. DESIGN ELUCIDATION AND VALIDATION OF PSEUDO-RIGID-BODY MODEL FOR SMALL-LENGTH FLEXURAL PIVOTS (SLFP) IN COMPLIANT MECHANISMS

3.1. INTRODUCTION

In a compound compliant beam, when the compliant segment is significantly shorter than the rigid segment, then it is referred to as a small-length flexural pivot (SLFP). A simple, compliant fixed-free beam, for example, is modeled as two rigid members connected at a pin joint, also termed as a characteristic pivot. The beam's resistance to bending, or beam compliance, is represented by a torsional spring at the pivot. For an SLFP, however, the characteristic pivot is assumed to be located at its center assuming a uniform cross-section segment [67]. An SLFP necessarily leads to the formation of a compound compliant beam, composed of two segments: a flexible or compliant segment (SLFP) and a rigid segment. Traditionally, the length of the rigid segment is assumed to be ten or more times larger than the length of the compliant segment.

With the ever-increasing interest and usage of SLFPs in modeling, it is deemed important to test the validity of the underlying assumptions and understand the congruent limitations. This paper investigates the efficacy of the PRBMs for both the initially-straight and initially-curved SLFPs, for varying compliant- to rigid-segment length ratio (ξ). This is accomplished by measuring the deflection error by an existing approach, reviewed herein. The error is assigned an acceptable value, a prerogative of the designer, in determining the corresponding limit value of ξ, and the fixed-free beam end deflections are experimentally supported.

3.2. RATIONALE FOR LOCATING THE CHARACTERISTIC PIVOT FOR SMALL-LENGTH FLEXURAL PIVOT

For an SLFP with a uniform cross-section, the assumption of the characteristic pivot's location at its center is valid only when the length of the compliant segment (SLFP) is significantly smaller than that of its adjacent rigid segment (Figure 3.1). Then the variation in the bending moment dM over the length dX of the SLFP is necessarily much smaller. Taking the average value of the bending moment across dX occurring at its midpoint, the characteristic pivot is assumed to be located there as well. This is consistent with assumptions made by Howell and Midha [67]. As the relative length of the compliant segment increases, the variation in the bending moment increases as well, rendering the assumption less valid. Figure 3.1 illustrates this with a bending moment diagram of a compound-compliant beam with an SLFP, subjected to a transverse load at its beam end.
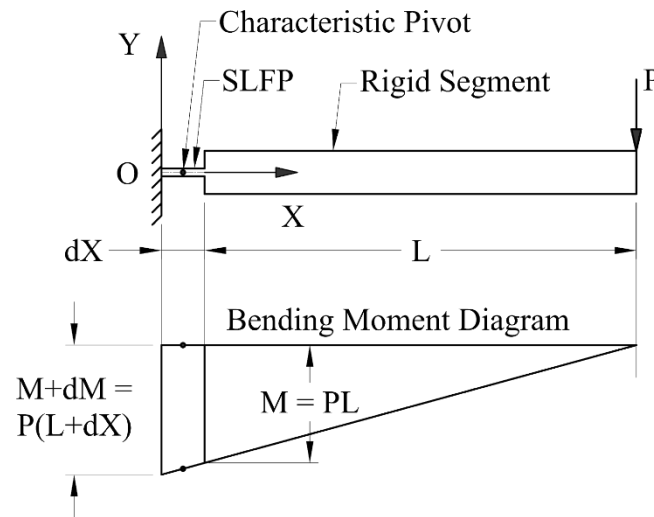
Figure 3.1 Bending Moment Diagram for Locating the Characteristic Pivot of an Initially-Straight SLFP.

3.3. INITIALLY-STRAIGHT SMALL-LENGTH FLEXURAL PIVOT

An initially-straight, compound, compliant, cantilever beam subjected to non-follower vertical and horizontal end loads, P and nP, respectively, is shown in Figure 3.2. The deflections of the compliant segment are predicted by using the closed-form elliptic integral method [72]. The forces and moments acting on the compliant segment due to the beam end loads are shown in Figure 3.1.

The displacement of the adjacent rigid segment is superimposed onto that of the compliant segment to obtain the total displacement of the beam. Thus, the beam end coordinates (a, b) and beam end angle θ_0 [81, 82] of the deflected position are derived from Equations 18 through 20.
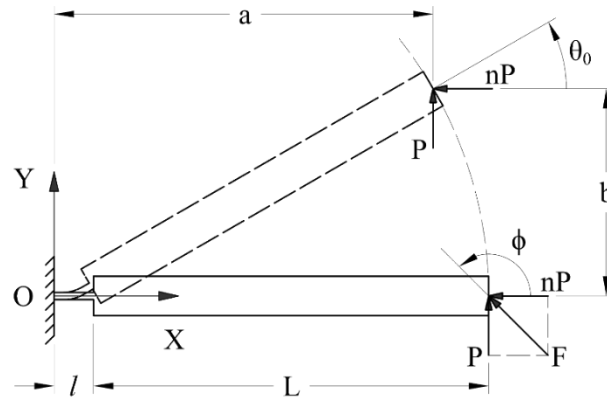
Figure 3.2 Initially-Straight SLFP

$$\alpha = \frac{1}{\sqrt{2}} \int_0^{\theta_0} \frac{d\theta}{\sqrt{\cos(\theta_0 - \phi) - \cos(\theta - \phi) + \lambda}} \tag{18}$$

$$a = \frac{l}{\sqrt{2}\alpha} \int_0^{\theta_0} \frac{\cos\theta \, d\theta}{\sqrt{\cos(\theta_0 - \phi) - \cos(\theta - \phi) + \lambda}} + L\cos\theta_0 \tag{19}$$
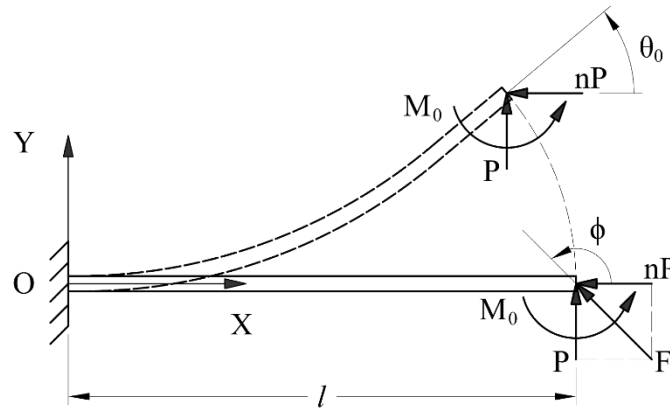
Figure 3.3 Equivalent Force and Moment on SLFP.

$$b = \frac{l}{\sqrt{2}\alpha} \int_0^{\theta_0} \frac{\sin\theta \, d\theta}{\sqrt{\cos(\theta_0 - \phi) - \cos(\theta - \phi) + \lambda}} + L\sin\theta_0 \tag{20}$$

where,

$$\alpha = \sqrt{\frac{Fl^2}{EI}} \tag{21}$$

$$\lambda = \frac{1}{2}\left(\frac{M_0}{EI}\right)^2 \left(\frac{l}{\alpha}\right)^2 \tag{22}$$

$$M_0 = FL\sin(\phi - \theta_0) \tag{23}$$

$$F = \sqrt{P^2 + (nP)^2} \tag{24}$$

$$\phi = \tan^{-1}\left(\frac{1}{-n}\right) \tag{25}$$

The PRBM method is utilized to estimate the deflections of the beam shown in Figure 3.3, which is illustrated in Figure 3.4. The beam is modeled as two rigid segments

pinned at the characteristic pivot; for an SLFP, it is located at the center of the compliant segment. The pseudo-rigid-body angle, Θ, describes the rotation of the rigid link.
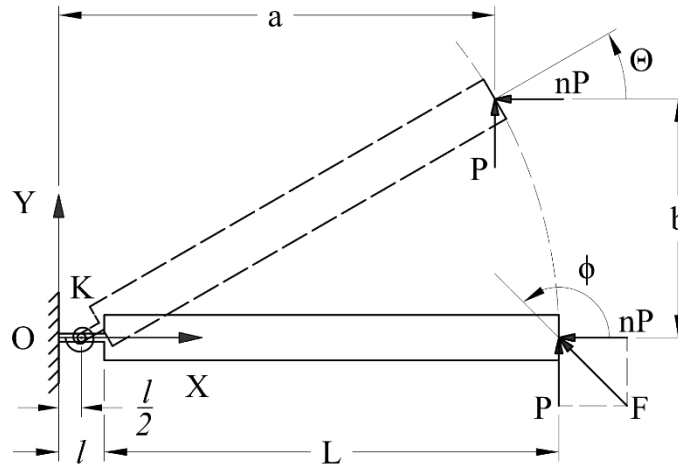
Figure 3.4 PRBM of Initially-Straight SLFP.

For an SLFP, the pseudo-rigid-body angle is assumed to be equal to its beam end angle, as the flexible segment is very small compared to the rigid segment, and the deflection occurs at the flexible segment.

$$\Theta = \theta_0 \qquad (26)$$

The resistance to bending of an SLFP is modeled as a torsional spring located at the characteristic pivot. The stiffness of the torsional spring is given by:

$$K = \frac{EI}{l} \qquad (27)$$

The beam end deflections obtained using the PRBM in Figure 3.4 are as follows

$$a = \frac{l}{2} + \left(L + \frac{l}{2}\right)\cos\Theta \qquad (28)$$

$$b = \left(L + \frac{l}{2}\right) sin\Theta \tag{29}$$

$$\mathrm{K} \cdot \Theta = \left(\mathrm{L} + \frac{l}{2}\right) \mathrm{F} \cdot sin(\phi - \Theta) \tag{30}$$

These deflections are compared against those obtained from the elliptic integral method [81], for the ratios, ξ ranging from 0.1 to 0.5, and for different loading conditions: i) tensile loads (n = -5 to -1), ii) transverse load (n = 0), and iii) compressive loads (n = 1 to 5). The maximum Pseudo-Rigid-Body (PRB) angle for the deflections that are within a predefined error of 3% are plotted in Figure 3.5 for various ratios, ξ, and loading conditions.
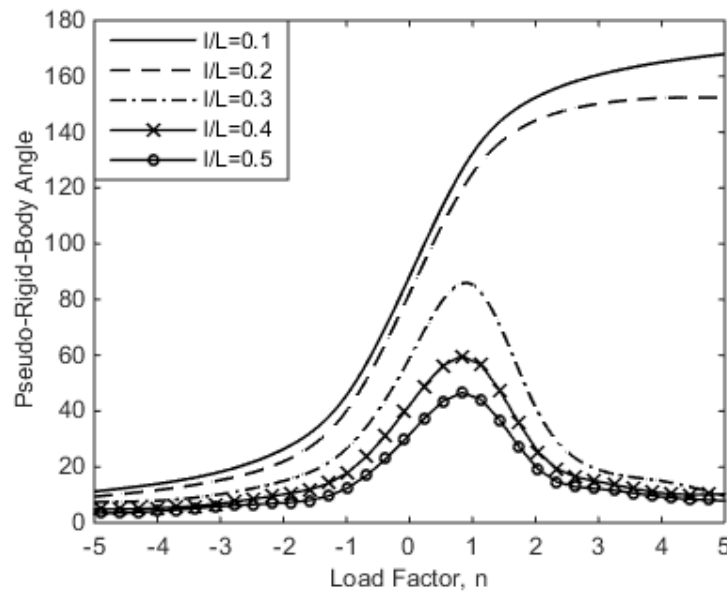
Figure 3.5 Allowable Maximum Pseudo-Rigid-Body Angle Θ for Different Loading Conditions and Segment Ratios.

Some of the plots that have been generated to study the PRBM results relative to the closed-form elliptic integral solutions are presented in Figures 3.6 to 3.10. Figures 3.6 & 3.7 shows the accuracy of the large deflections predicted, for respective ξ values 0.1 & 0.2, when subjected to various loading conditions. Whereas, for ξ values 0.3, 0.4 & 0.5,

the deflections predicted by PRBM diverge from those obtained by the closed-form elliptic integral method as shown in Figures 3.8, 3.9 & 3.10, respectively. These plots show the normalized deflected beam end coordinates.

It is observed from these plots, as expected, that the beam deflections are smaller for tensile loads and larger for compressive loads. The PRBM deflections tend to agree with the elliptic integral solution for tensile loads for all the given values of the ratio, ξ. However, for the transverse and compressive loads, the error tends to increase for higher values of the ratio, ξ. Hence, it can be concluded that in general, the PRBM can accurately predict the beam end coordinates for large deflections, subjected to any loads for ξ values of 0.1 and 0.2. For any ξ value, 0.3 and beyond, the PRBM of an initially-straight SLFP could not predict the large deflections under a 3% error.

3.4. INITIALLY-CURVED SMALL-LENGTH FLEXURAL PIVOT

Figure 3.11 shows an initially-curved, fixed-free compound compliant beam subjected to non-follower vertical and horizontal loads, P and nP, respectively at its end. The compliant segment of the beam has an initial curvature of $1/R_i$. The total displacement of the beam end is a superposition of the elastic deflection of the compliant segment and the displacement of the adjacent rigid segment.

The elastic deflection of the compliant segment is computed by the closed-form elliptic integral method, which is subjected to the equivalent forces and moment as shown in Figure 3.12. The displacement of the rigid segment is dependent on the beam end angle of the compliant segment.
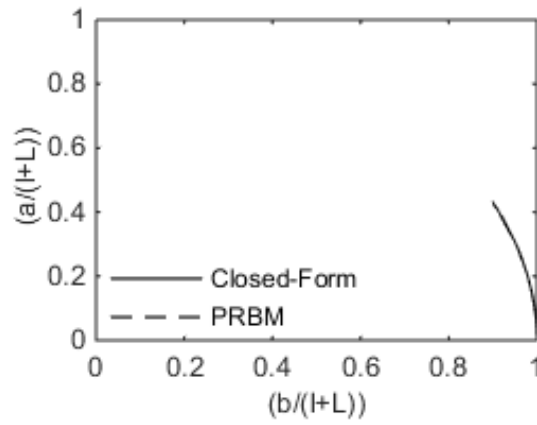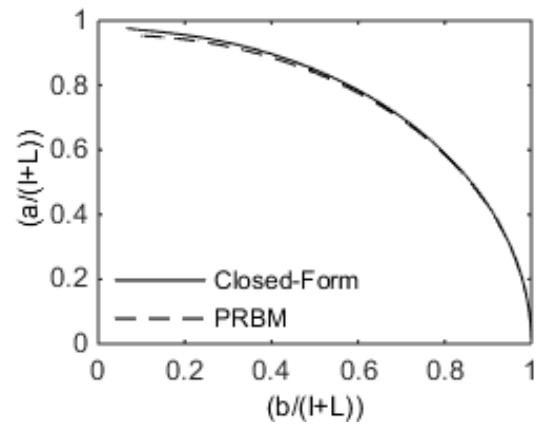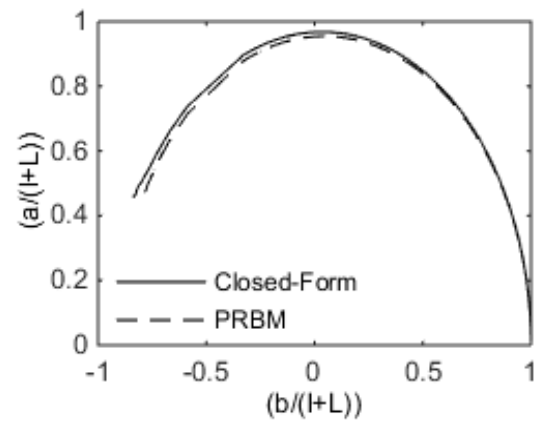
Figure 3.6 Deflections of Beam with Ratio, $\xi = 0.1$ for (a) Tensile Load, n = -2, (b) Transverse Load, n = 0, (c) Compressive Load, n = 2.
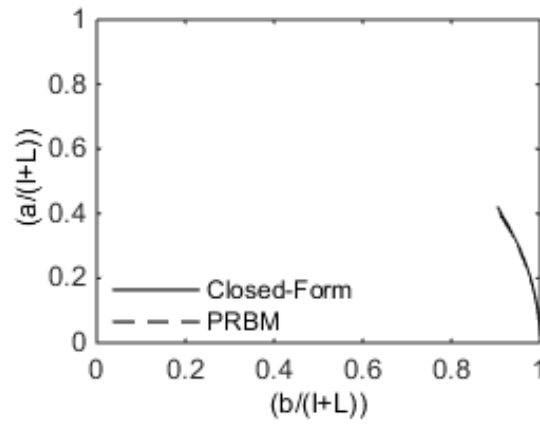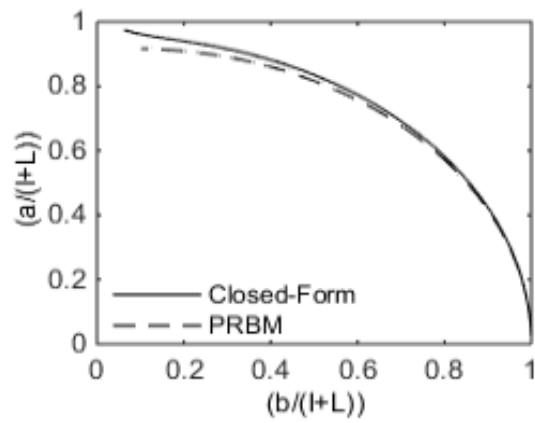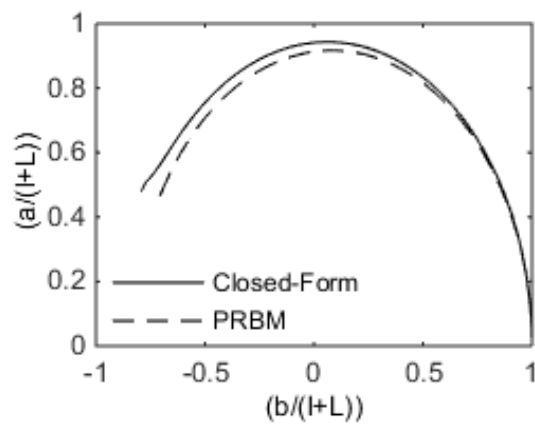
Figure 3.7 Deflections of Beam with Ratio, $\xi = 0.2$ for (a) Tensile Load, $n = -2$, (b) Transverse Load, $n = 0$, (c) Compressive Load, $n = 2$.
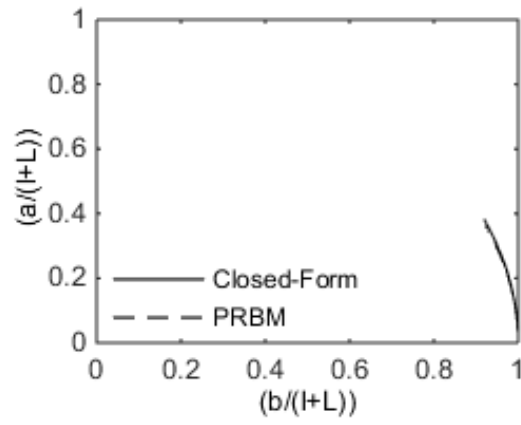
(a)
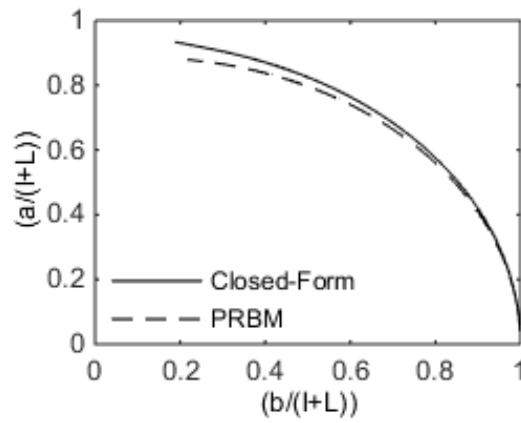
(b)
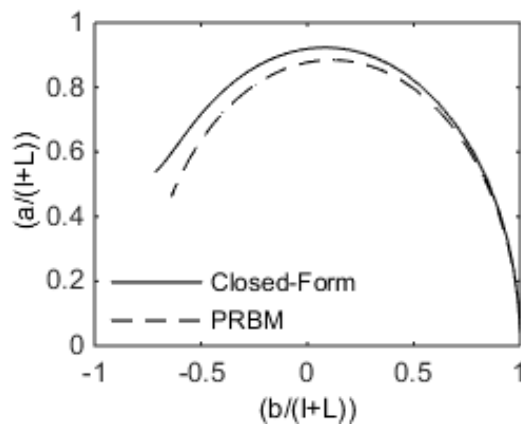
(c)

Figure 3.8 Deflections of Beam with Ratio, ξ = 0.3 for (a) Tensile Load, n = -2, (b) Transverse Load, n = 0, (c) Compressive Load, n = 2.
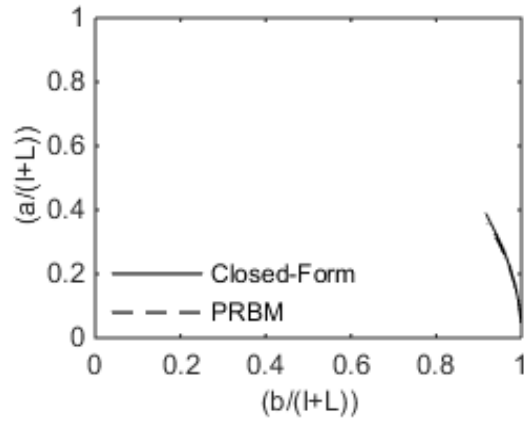
(a)
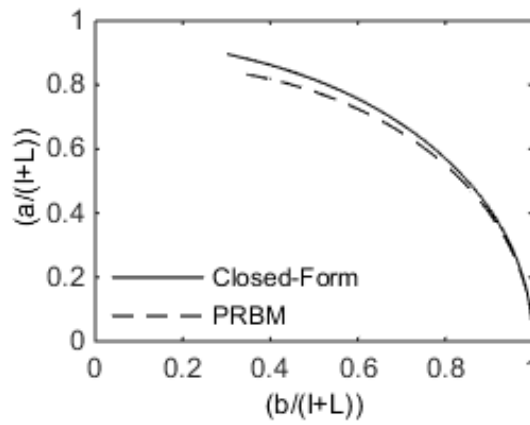
(b)
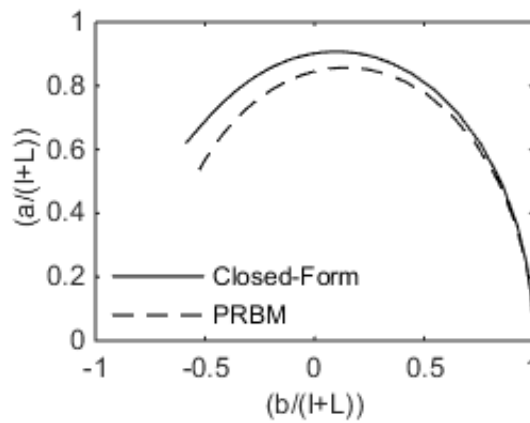
(c)

Figure 3.9 Deflections of Beam with Ratio, ξ = 0.4 for (a) Tensile Load, n = -2, (b) Transverse Load, n = 0, (c) Compressive Load, n = 2**.**
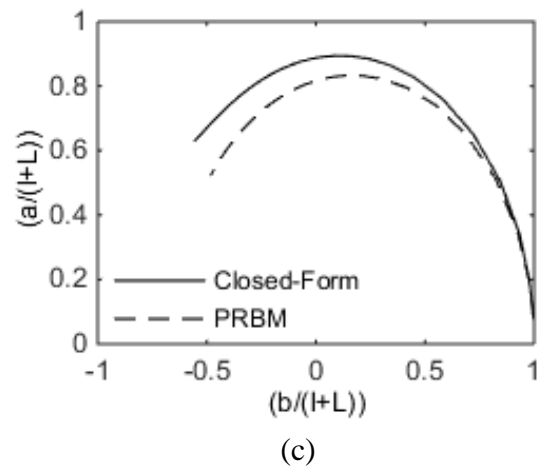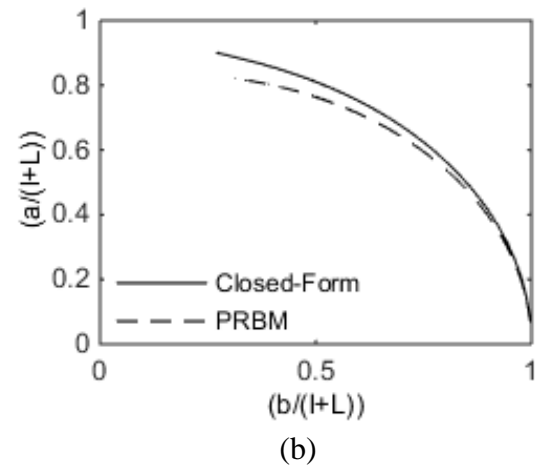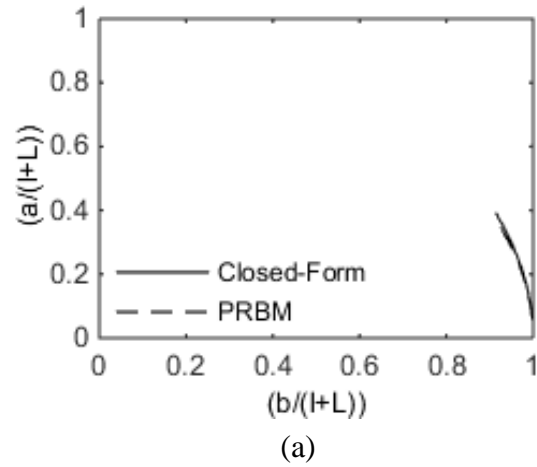
Figure 3.10 Deflections of Beam with Ratio, $\xi = 0.5$ for (a) Tensile Load, $n = -2$, (b) Transverse Load, $n = 0$, (c) Compressive Load, $n = 2$.

The equivalent force, F, and the moment, M_0, acting on the compliant segment are shown below along with the tangential component of the force, F_t:

$$F = \sqrt{P^2 + (nP)^2} \tag{31}$$

$$F_t = F \cdot \sin(\phi - \theta_0) \tag{32}$$

$$M_0 = F_t \cdot L \tag{33}$$

where,

$$\phi = \tan^{-1}\left(\frac{1}{-n}\right) \tag{34}$$
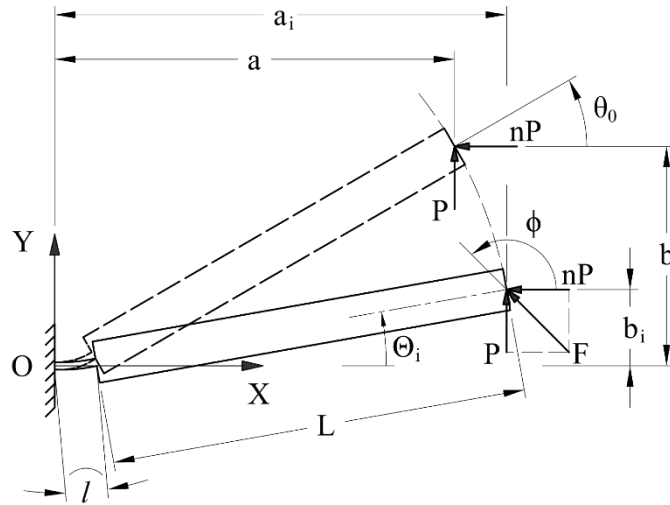
Figure 3.11 Initially-Curved SLFP.

The closed-form elliptic integral equations used to solve for the beam end coordinates [81, 82] are expressed as follows:

$$\alpha = \frac{1}{\sqrt{2}} \int_0^{\theta_0} \frac{d\theta}{\sqrt{\cos(\theta_0 - \phi) - \cos(\theta - \phi) + \lambda}} \tag{35}$$

$$a = \frac{l}{\sqrt{2}\alpha} \int_0^{\theta_0} \frac{\cos\theta \; d\theta}{\sqrt{\cos(\theta_0 - \phi) - \cos(\theta - \phi) + \lambda}} + L\cos\theta_0 \qquad (36)$$

$$b = \frac{l}{\sqrt{2}\alpha} \int_0^{\theta_0} \frac{\sin\theta \; d\theta}{\sqrt{\cos(\theta_0 - \phi) - \cos(\theta - \phi) + \lambda}} + L\sin\theta_0 \qquad (37)$$

where,

$$\alpha = \sqrt{\frac{Fl^2}{EI}} \qquad (38)$$

$$\lambda = \frac{1}{2}\left(\frac{M_0}{EI} + \frac{1}{R_i}\right)^2 \left(\frac{l}{\alpha}\right)^2 \qquad (39)$$

The PRBM of the beam in Figure 3.11 is demonstrated in Figure 3.13. The beam is modeled as two rigid links pinned at the characteristic pivot located at the center of the compliant segment along its curvature. The initial radius of curvature of the compliant segment can be related to its length with a non-dimensional parameter, κ_0. For the beams with an SLFP, the pseudo-rigid-body angle, Θ, is assumed to be equal to the beam end angle, θ_0.

$$\kappa_0 = \frac{l}{R_i} \qquad (40)$$

$$\Theta = \theta_0 \qquad (41)$$

The initial beam end coordinates and the pseudo-rigid-body angle of the beam are expressed as follows:

$$a_i = \frac{l}{\kappa_0}\sin\kappa_0 + L\cos\kappa_0 \qquad (42)$$

$$b_i = \frac{l}{\kappa_0}(1 - \cos \kappa_0) + L \sin \kappa_0 \tag{43}$$

$$\Theta_i = tan^{-1}\left(\frac{b_i - \frac{l}{2\kappa_0}(1 - \cos \kappa_0)}{a_i - \frac{l}{2\kappa_0}\sin \kappa_0}\right) \tag{44}$$
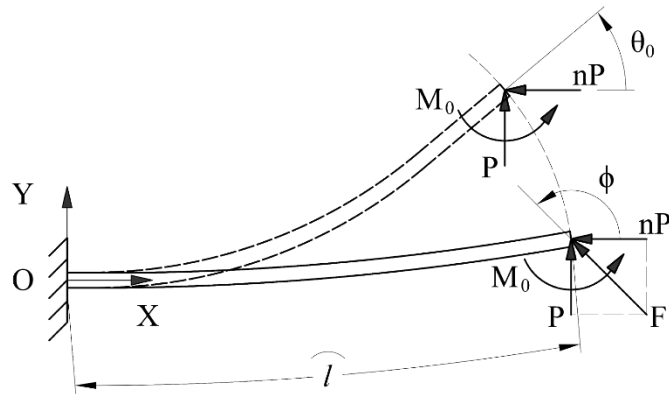
Figure 3.12 Initially-Curved SLFP with Equivalent Loads.
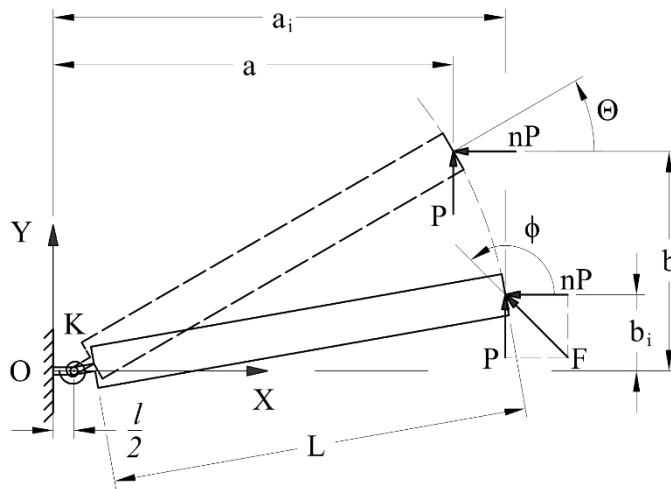
Figure 3.13 PRBM of Initially-Curved SLFP.

The beam end deflections predicted using the PRBM method are expressed as follows:

$$a = \frac{l}{2\kappa_0}\sin\kappa_0 + \left(L + \frac{l}{2}\right)\cos\Theta \tag{45}$$

$$b = \frac{l}{2\kappa_0}(1 - \cos\kappa_0) + \left(L + \frac{l}{2}\right)\sin\Theta \tag{46}$$

also,

$$K(\Theta - \Theta_i) = \left(L + \frac{l}{2}\right)F \cdot \sin(\phi - \Theta) \tag{47}$$

Where, K is the stiffness of the torsional spring located at the characteristic pivot that represents the resistance of the compliant segment,

$$K = \frac{EI}{l} \tag{48}$$

The deflections of the PRBM of an SLFP are computed for ξ values ranging from 0.1 to 0.5. Figure 14 shows the plot of the maximum pseudo-rigid-body angle predicted for the deflections within the predefined error, 3% when subjected to different loading conditions for various compliant- to rigid-segment ratios, ξ.

From the above plot, it is observed that the PRBM of an initially-curved SLFP can predict large deflections accurately for ξ values of 0.1 and 0.2 when subjected to either compressive or tensile loads. For ξ value of 0.3, the PRBM predicts the beam end coordinates within the 3% error for considerably large deflections, however, as the compressive load increases the pseudo-rigid-body angle for a 3% error decreases. Hence, it is recommended to use the PRBM technique for ξ value of 0.3 with caution, especially when subjected to extremely high compressive loads. For ξ values of 0.4 and beyond, the

PRBM of an initially-curved SLFP is not recommended as the error is more than 3% for the predicted deflections.
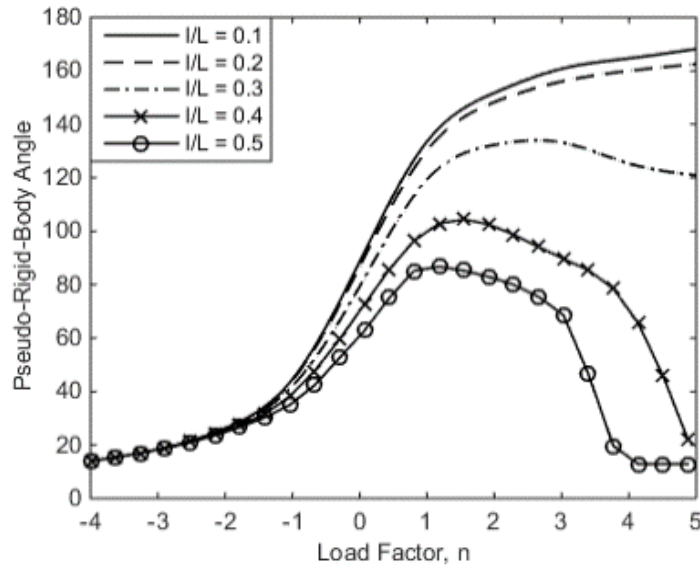
Figure 3.14 Max. Pseudo-Rigid-Body Angle at Different Loading Conditions, for 3% Error.

Plots have been generated to evaluate the performance of the PRBM when compared to the closed-form elliptic integral method. Figures 3.15, 3.16, & 3.17 demonstrate the accuracy of the large deflections predicted when subjected to different loading conditions, for ξ values 0.1, 0.2 & 0.3, respectively. On the other hand, for ξ values 0.4 & 0.5, the PRBM deflections diverge from those obtained by using a closed-form elliptic integral method as shown in Figures 3.18 & 3.19, respectively. The plots show the normalized deflected beam end coordinates.

(a)

(b)

(c)
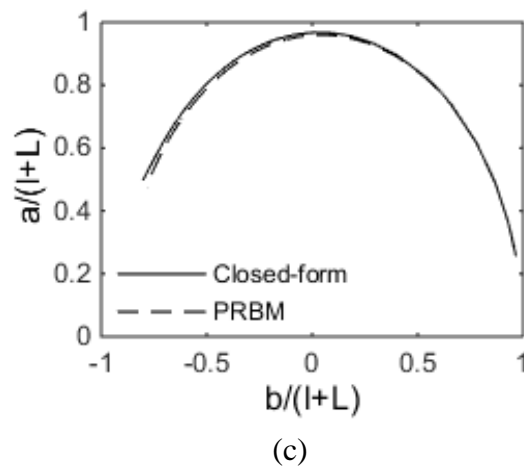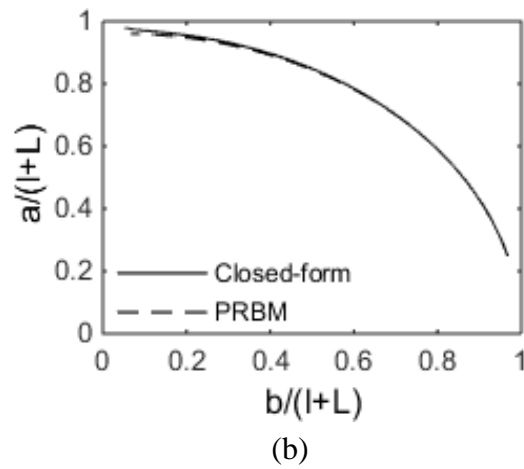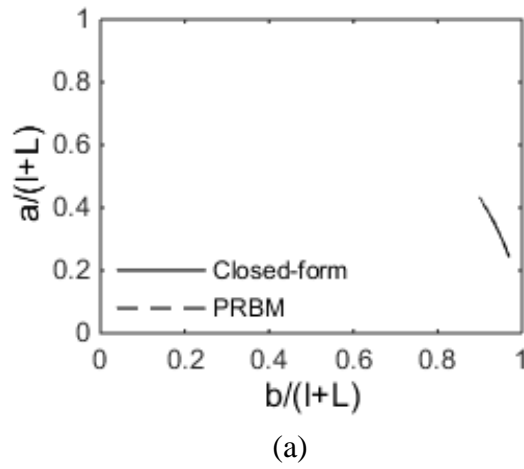
Figure 3.15 Deflections of Beam with Ratio, ξ = 0.1 for (a) Tensile Load, n = -2, (b) Transverse Load, n = 0, (c) Compressive Load, n = 2.

(a)

(b)

(c)
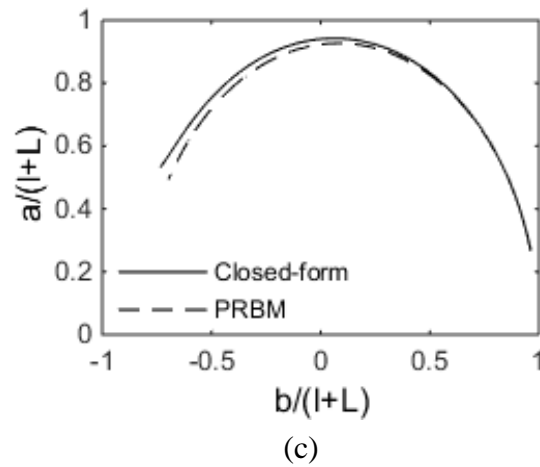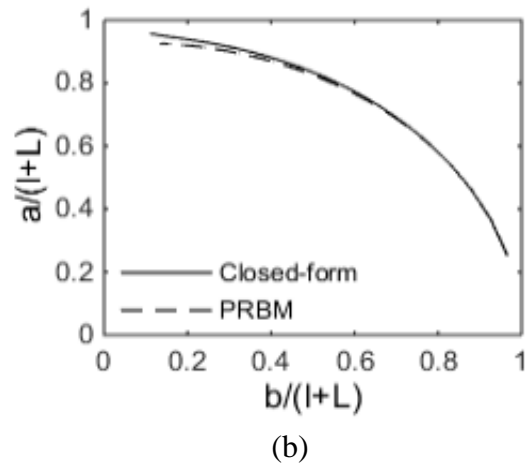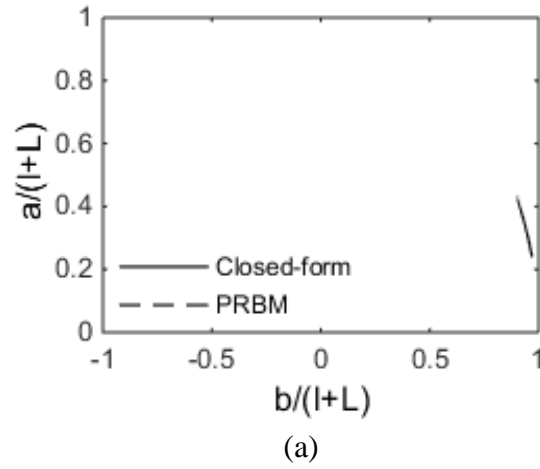
Figure 3.16 Deflections of Beam with Ratio, ξ = 0.2 for (a) Tensile Load, n = -2, (b) Transverse Load, n = 0, (c) Compressive Load, n = 2.
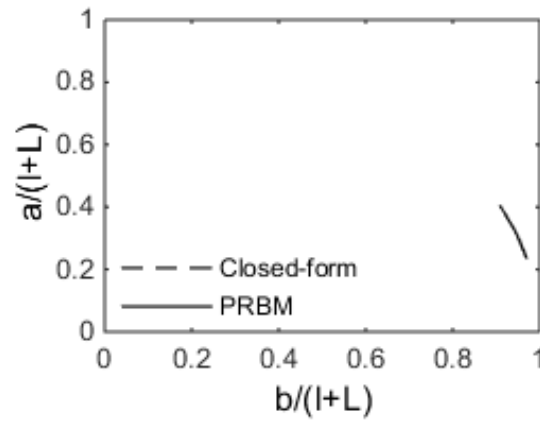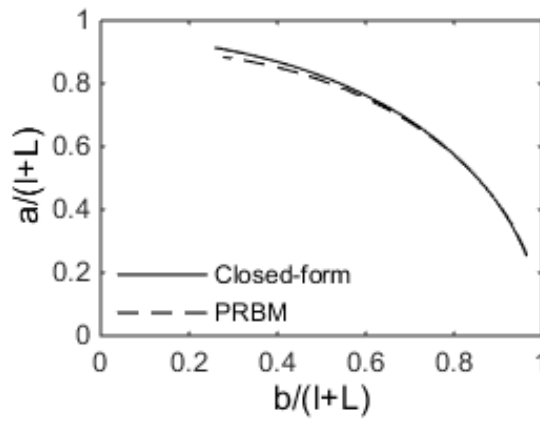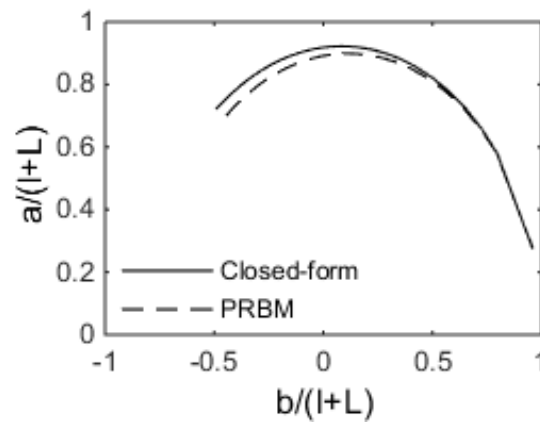
Figure 3.17 Deflections of Beam with Ratio, ξ = 0.3 for (a) Tensile Load, n = -2, (b) Transverse Load, n = 0, (c) Compressive Load, n = 2.
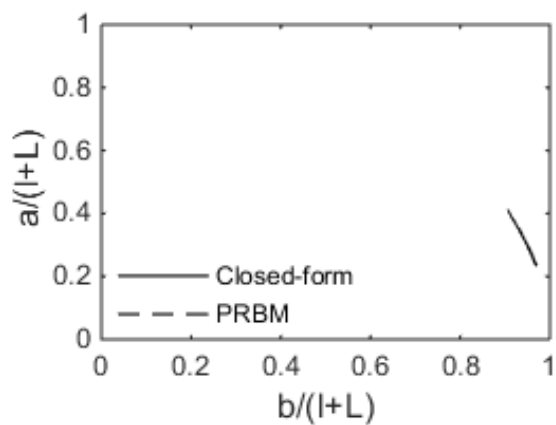
(a)
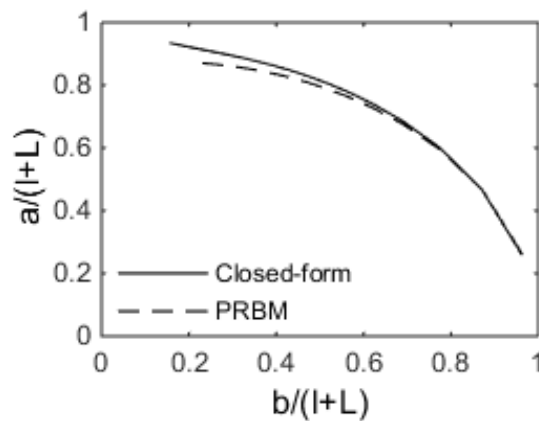
(b)
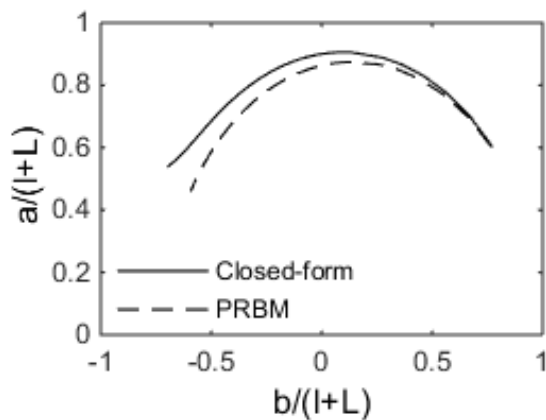
(c)

Figure 3.18 Deflections of Beam with Ratio, $\xi = 0.4$ for (a) Tensile Load, $n = -2$, (b) Transverse Load, $n = 0$, (c) Compressive Load, $n = 2$.

(a)

(b)

(c)
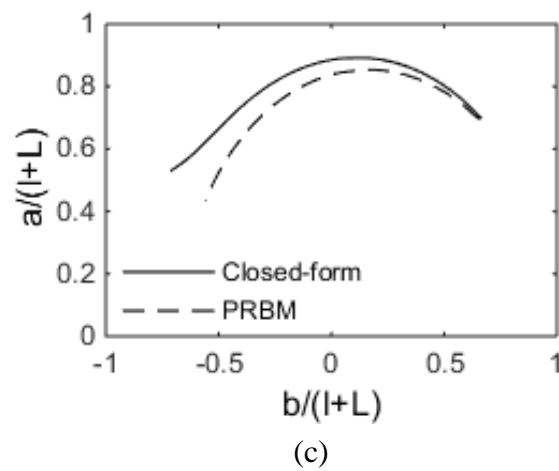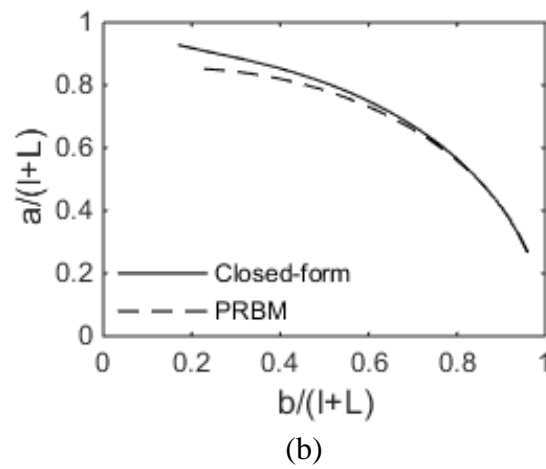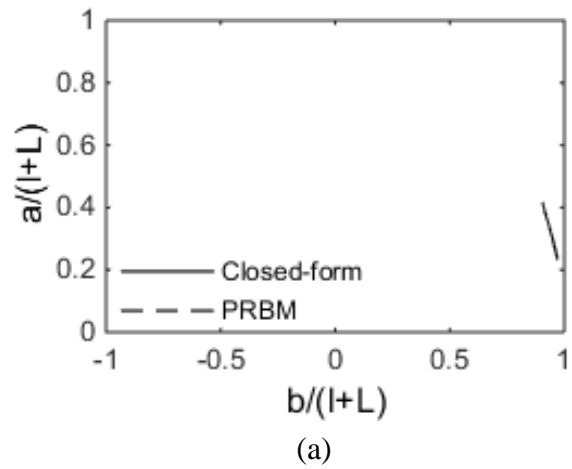
Figure 3.19 Deflections of Beam with Ratio, $\xi = 0.5$ for (a) Tensile Load, n = -2, (b) Transverse Load, n = 0, (c) Compressive Load, n = 2.

3.5. DEVIATION OF ERROR, AND CAUSES FOR VARIATIONS IN ERROR

The beam-end coordinates of the deflected position obtained from the closed-form elliptic integral method (a, b), and PRBM method are presented in Figure 3.20 along with its initial coordinates. The vector joining these coordinates with the un-deflected beam end, $((L+l), 0)$, also shown in Figure 3.20, is stated in Equation 49.
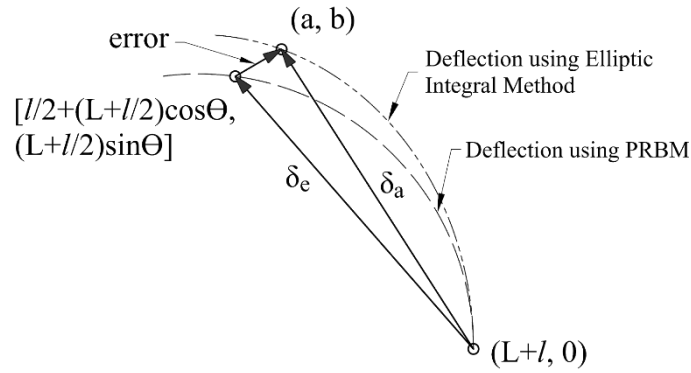
Figure 3.20 Error Definition.

$$\delta_a = \sqrt{(L + l - a)^2 + b^2} \tag{49}$$

The vector from the un-deflected beam end to the deflected beam-end coordinates predicted by the PRBM (Figure 3.20), can be expressed as follows:

$$\delta_e = \sqrt{\left[\left(L + \frac{l}{2}\right)(1 - \cos\Theta)\right]^2 + \left[\left(L + \frac{l}{2}\right)(\sin\Theta)\right]^2} \tag{50}$$

The error, defined relative to the deflection predicted by the closed-form elliptic integral method, is represented by a vector joining the beam end coordinates of the deflected positions predicted by the two methods. The relative error is computed as,

$$error = \frac{\sqrt{\left\{a - \left[\frac{l}{2} + \left(L + \frac{l}{2}\right)\cos\Theta\right]\right\}^2 + \left\{b - \left(L + \frac{l}{2}\right)\sin\Theta\right\}^2}}{\sqrt{(L + l - a)^2 + b^2}} \tag{51}$$

It can be observed that the error in the deflections predicted by PRBM of an initially-straight SLFP is larger than that of an initially-curved SLFP for the same ξ values and loading conditions. This can be predominantly attributed to the buckling mode of an initially-straight beam. The pre-existing curvature of an initially-curved beam alleviates the buckling mode and aids the beam with rotation for the same loading conditions as for an initially-straight beam, which results in lower errors. Hence, for a higher value of ξ for an initially-curved SLFP, the PRBM method qualifies to predict its beam end coordinates accurately within the specified error.

The analysis is conducted for different lengths of the compliant segment, $l = 1, 2, 3, 4, \& 5$ while maintaining the rigid segment's length constant, $L = 10$ to achieve various ratios, ξ ranging from 0.1 to 0.5. The beam end deflections presented in this paper are normalized w.r.t the length of the beam. However, for a given ξ value, it is observed that the error decreases when the lengths of the compliant and rigid segments are reduced and vice-versa. Hence, the error is directly proportional to both the absolute length of the segments and the ratio ξ.

In Figures 3.5 and 3.14, a change in trend can be observed for ratios, ξ, 0.3 & beyond for the initially-straight beam, and 0.4 & beyond for the initially-curved beam. This is because the error in the large deflections increases as the ratio increases, and these plots present only the maximum pseudo-rigid-body angles for the deflections predicted under the 3% error. The reader has a choice to use the PRBM of an SLFP to predict large deflections for higher values of ξ, by allowing a higher error percentage.

3.6. EXPERIMENTAL VALIDATION

Experiments were conducted to validate the performance of the PRBM of initially-straight and initially-curved SLFPs, in compound-compliant beams for the ξ ratios greater than 0.1. As noted earlier, the PRBM for initially-straight SLFP effectively predicts the beam's behavior, for ξ values 0.1 and 0.2. Similarly, the PRBM for initially-curved SLFP effectively predicts the beam's behavior, for ξ values 0.1, 0.2, and 0.3. The experiments were conducted on the compound-compliant beams with higher ξ ratios that are subjected to high compressive loads to validate the theoretical results presented in this section.

The experiments were performed on the experimental set-up developed by Bapat et al. [83]. The set-up has been slightly modified to accommodate long beams, subjected to compressive loads. The beams were held vertically down, unlike in the original arrangement, to minimize the effect of gravity load on the results. The experiments are demonstrated below.

3.6.1. Initially-Straight Small-Length Flexural Pivot. The ξ ratio is 0.2 for this compound-compliant beam and subjected to compressive loads, $\phi = 136.29°$ (n = 1.04). The length of the SLFP is 2 in. and the length of the rigid segment is 10 in. The load is applied at the beam end with a pulley system, as shown in Figure 3.21. The beam-end deflection is traced onto a graph sheet by a pencil that has been attached to it.

The beam end deflections obtained from the experiment, the PRBM method, and the elliptic integral method are plotted, as shown in Figure 3.22. The relative error of the deflection obtained from the experiment at the beam end is 0.91% with respect to the closed-form solution. It is observed that the deflections from the experiment match the closed-form deflections.
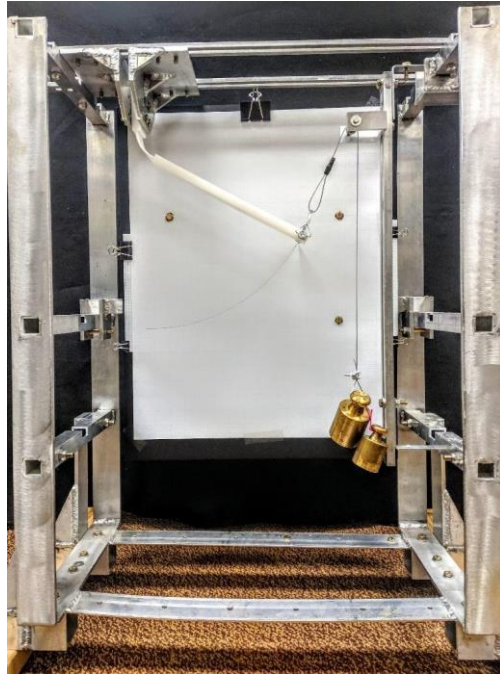
Figure 3.21 Experimental Setup for Initially-Straight Compound Compliant Beam.
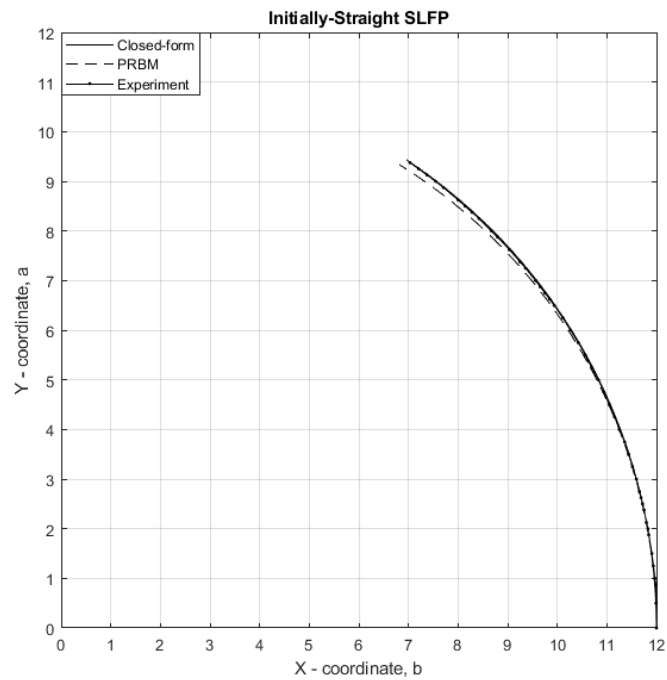
Figure 3.22 Comparison of Beam-end Deflections from the Experiment compared to
Closed-form and PRBM Results for Initially-Straight SLFP.

3.6.2. Initially-Curved Small-Length Flexural Pivot. The ξ ratio is 0.3 for this compound-compliant beam and subjected to compressive loads, $\phi = 136.29°$ (n = 1.04). The length of the curved SLFP is 3 in. and the length of the rigid segment is 10 in. The load is applied at the beam end with a pulley system, as shown in Figure 3.23. The beam end deflection is similarly traced onto a graph sheet by a pencil attached to it.
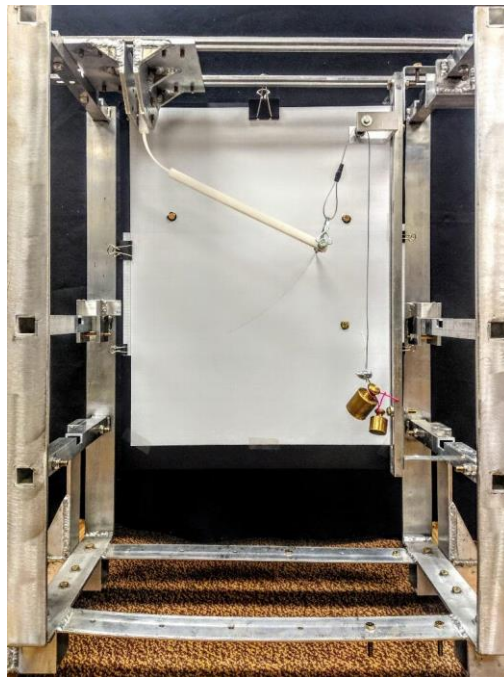
Figure 3.23 Experimental Setup for Initially-Curved Compound Compliant Beam.

The beam end deflections obtained from the experiment, the PRBM method, and the elliptic integral method are plotted in Figure 3.24. The relative error of the deflection obtained from the experiment at the beam end is 2.02% with respect to the closed-form solution. It is observed that the relative error is slightly more than the previous experiment results, it could be due to the machining imperfections associated with water-jet cutting the initially-curved SLFP, and probably due to human error while conducting the experiment.
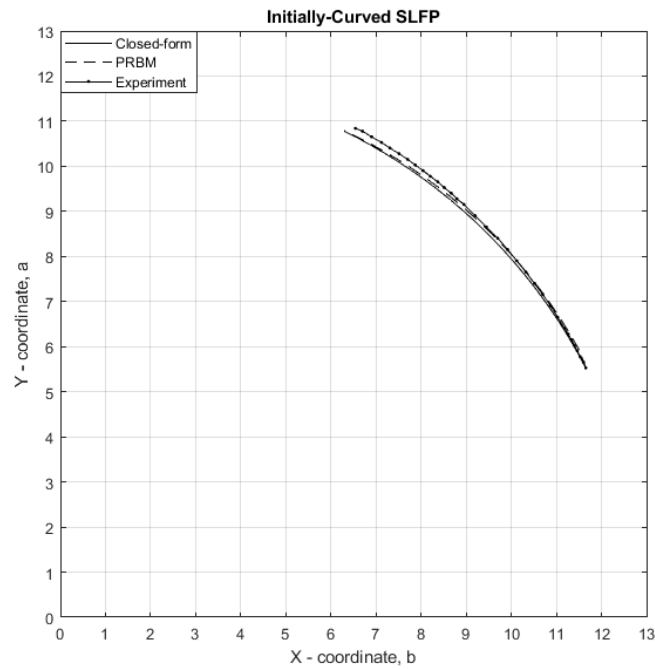
Figure 3.24 Comparison of Beam-end Deflections from the Experiment to Closed-form and PRBM Results for Initially-Curved SLFP.

3.7. SUMMARY

The PRBM of an SLFP method has been examined by comparing the deflections predicted with those generated by the closed-form elliptic integral method for both initially-straight and initially-curved compound compliant beams for the ξ values 0.1, 0.2, 0.3, 0.4, and 0.5. From this investigation, it is concluded that the PRBM for an initially-straight SLFP effectively predicts the beam end deflections for ξ values 0.1 and 0.2, when subjected to various loading conditions.

Similarly, the PRBM for an initially-curved SLFP accurately predicts the beam end deflections for ξ values 0.1, 0.2, and 0.3, under different loading conditions. However, for ξ value 0.3, the PRBM may not predict large deflections for a 3% error, when subjected to

very high compressive loads (n ≥ 4). Tables 3.1 & 3.2 show the corresponding pseudo-rigid-body angles for the deflections predicted for 3% error, respectively for initially-straight and initially-curved SLFP. For the other ξ values that are not presented in tables 3.1 and 3.2, it is recommended to use PRBM of the fixed-fixed beam to model that compound-compliant segment to predict the deflections accurately.

The experiments validate that the PRBM method effectively predicts the behavior of a fixed-free compound compliant beam for the ξ ratios up to 0.2 for initially-straight SLFP and ξ ratios for up to 0.3 for initially-curved SLFP. It is noted that the PRBM method effectively predicts any tensile and transverse loading. However, for the compressive loads, the designer needs to be aware that the PRBM effectively predicts up to 150 degrees of deflection for initially-straight SLFP and up to 120 degrees for initially-curved SLFP.

Table 3.1 Max Θ Values for Initially-Straight SLFP

	n	-5	-4	-3	-2	-1	0	1	2	3	4	5
ξ =0.1	Θ	11.21	13.95	18.30	26.90	44.28	88.14	133.95	151.89	160.41	165.05	167.94
ξ =0.2	(degrees)	9.40	11.70	15.38	22.45	38.67	82.16	126.75	143.70	150.00	152.24	152.28

Table 3.2 Max Θ Values for Initially-Curved SLFP

	Θ_i (deg)	n	-4	-3	-2	-1	0	1	2	3	4	5
ξ =0.1	13.99		14.03	18.34	26.44	44.52	88.68	133.69	151.65	160.79	164.64	168.20
ξ =0.2	13.68	Θ (degrees)	14.03	18.37	22.40	44.10	86.79	130.38	148.22	156.00	159.97	162.57
ξ =0.3	13.40		14.02	18.33	26.05	41.84	79.23	119.82	131.99	133.37	125.13	120.94

4. DESIGN AND ANALYSIS OF CONSTANT-FORCE COMPLIANT SEGMENTS

4.1. INTRODUCTION

This work demonstrates the fundamental behavior of simple compliant segments with different boundary conditions, under axial loading, that they produce near-constant force [84]. The compliant segment types considered herein are fixed-free, pinned-pinned, and fixed-guided beams, along with a compound-compliant segment with a small-length flexural pivot (SLFP). Analytical models are developed based on the pseudo-rigid-body model (PRBM) concept to derive the force equations and predict their force-displacement characteristic behavior. The models are extended to study the behavior of a rigid-body arrangement of a pivoted link with a torsional spring under axial loading.

4.2. FIXED-FREE COMPLIANT BEAM

A simple, compliant segment fixed at one end and free at the other end, subjected to axial-compressive loading, is presented in Figure 4.1. The beam has to be preloaded or slightly perturbed from its axis before loading to allow it to deflect in the desired direction. This arrangement of fixed-free compliant beam generates near-constant force over its deflection without the need for any design optimization, as illustrated in Figure 4.2. It is scalable in size and the magnitude of the output force profile.

The constancy of the force generated by the compliant beam is independent of its geometric and material properties. It is, however, dependent on the initial beam-end angle, and the constancy of the force increases as the angle tends to zero degrees. For non-zero or large initial angles, the output force profile is similar to that of a soft spring.
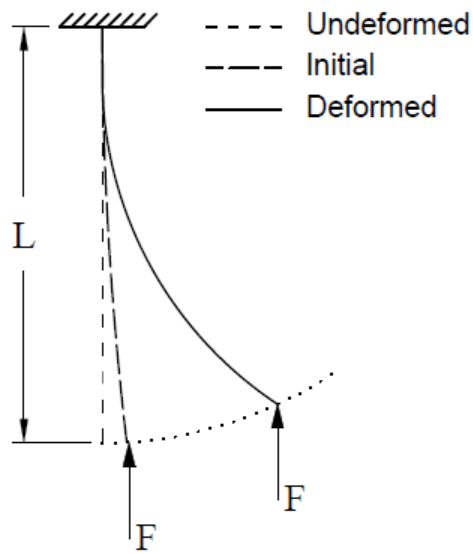
Figure 4.1 Fixed-Free Compliant Beam.
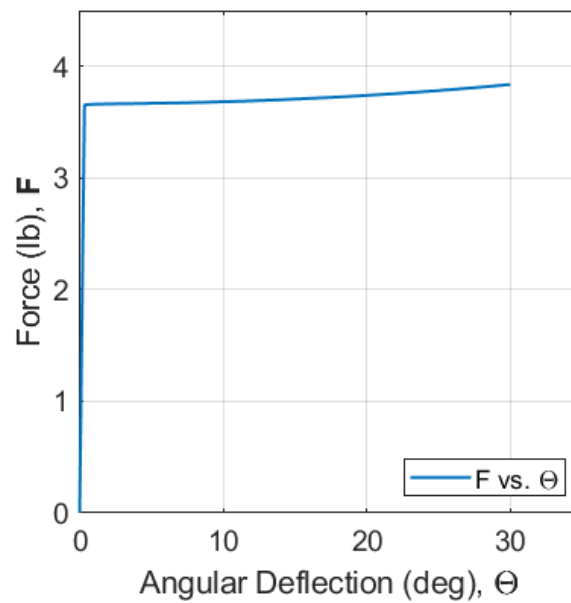
Figure 4.2 Force Vs. Deflection of Fixed-Free Compliant Beam.

The PRBM technique [65, 68-71] is used to model the compliant beam and analyze its force-characteristic behavior.   The force equations are derived from the static

equilibrium position of the pseudo-rigid-body (PRB) model of the fixed-free compliant

beam shown in Figure 4.3 to determine its force-displacement characteristics

.
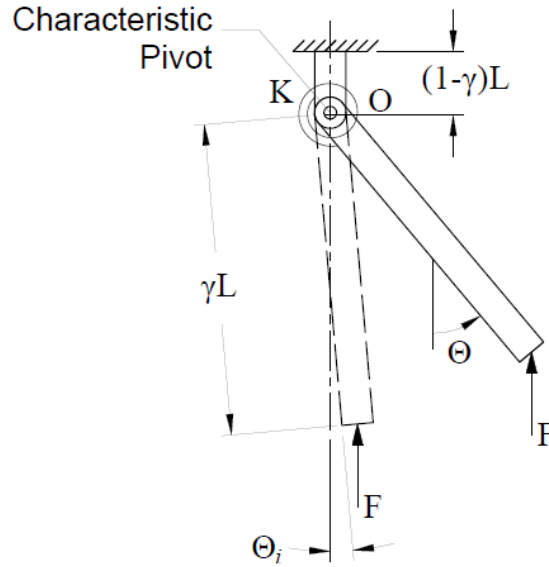
Figure 4.3 PRBM of Fixed-Free Compliant Beam.

$\sum M_O = 0$:

$$F. \gamma L \sin \Theta = K(\Theta - \Theta_i) \tag{52}$$

$$F = \frac{K(\Theta - \Theta_i)}{\gamma L \sin \Theta} \tag{53}$$

where,

$$K = \gamma K_\Theta \frac{EI}{L} \tag{54}$$

$$I = \frac{wt^3}{12} \tag{55}$$

The force equation is simplified with the Taylor/ Maclaurin series [85, 86],

$$F = \frac{K(\Theta - \Theta_i)}{\gamma L \left(\Theta - \frac{\Theta^3}{3!} + \frac{\Theta^5}{5!} - \frac{\Theta^7}{7!} \right)} \tag{56}$$

It is simplified furthermore with the Taylor/Maclaurin series [85, 86] as the initial beam-end angle tends to zero,

$$F = \frac{K}{\gamma L}(1 + 0.1667\Theta^2 + 0.0194\Theta^4) \tag{57}$$

The *characteristic load*, henceforth, defined as the first value of the force exerted by the beam at zero deflection, of the fixed-free compliant beam is as follows:

$$F_c = \frac{K}{\gamma L} = 3.67 \; lb \tag{58}$$

For this example, Delrin is the material of choice for the fixed-free beam. Table 4.1 lists the compliant beam parameters for the force-deflection plot in Figure 4.2.

Table 4.1 Fixed-Free Compliant Beam Parameters

$E = 420,000 \; psi$	$L = 3.5 \; in$	$b = 0.5 \; in$
$h = 0.1 \; in$	$\gamma = 0.8156$	$K_\Theta = 2.56597$
$\Theta_i = 0.01°$		

It is well known that a member under compressive axial loading buckles when the force reaches a critical level, i.e., Euler's critical load [87-89]. Upon investigation, it is observed that the beam's characteristic load is almost identical to its critical buckling

load. The Euler's critical load of a segment is dependent on its boundary conditions, so the formula for the fixed-free compliant beam is as follows.

$$P_{cr} = \frac{\pi^2 EI}{(2L)^2} = 3.525\ lb \qquad (59)$$

The ratio of the characteristic load and the critical load of the beam is, henceforth, termed as the *Characteristic Load Factor, η_c*.

$$\eta_c = \frac{F_c}{P_{cr}} = \frac{4K_\Theta}{\pi^2} = 1.039 \qquad (60)$$
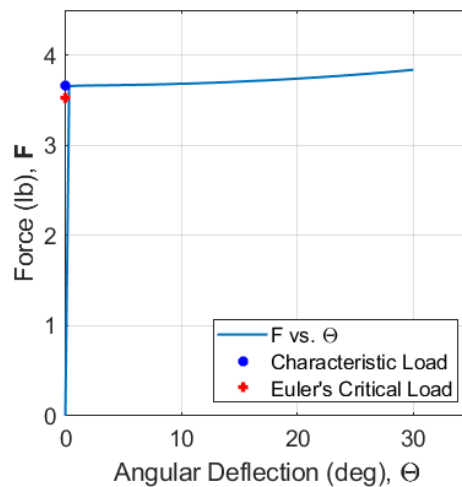
Figure 4.4 Force Vs. Deflection of Fixed-Free Compliant Beam, With its Characteristic and Critical Load.

It may be noted that these values are nearly the same, and their ratio near unity signifies that the beam generates near-constant force in its post-buckling stage, as demonstrated in Figure 4.4. It lends interesting insight into the generation of constant force by compliant beams and the existing constant-force mechanisms.

The difference between F_c and P_{cr} is probably due to the assumptions made in Euler's equation. Beam's characteristic load is probably more reliable because it is derived based on the PRBM concept, which is developed off the elliptic integral solutions with an error of less than 0.5%.

It is now established that the fixed-free, compliant beam generates constant force when subjected to axial loading. The investigation is extended to examine the performance of the pinned-pinned and fixed-guided compliant beams under compressive axial loading. The force characteristics of these two segment types are expected to be similar to that of the fixed-free beam.

4.3. PINNED-PINNED COMPLIANT BEAM

A pinned-pinned compliant beam, displayed in Figure 4.5, is pivoted at both ends and allowed to translate axially/vertically at least at one end, if not both, but is constrained in the transverse direction. The PRBM of the pinned-pinned beam, which consists of two characteristic pivots with torsional springs, is illustrated in Figure 4.6 [26, 68-71, 90]. Similar to the fixed-free beam, it, under axial loading, generates near-constant force without any need for design optimization. The force equation is derived from the half model of its PRBM, shown in Figure 4.7, due to symmetry.

$$\sum M_O = 0 :$$

$$F . \frac{\gamma L}{2} \sin \Theta = K(\Theta - \Theta_i) \tag{61}$$

$$F = \frac{2K(\Theta - \Theta_i)}{\gamma L \sin \Theta} \tag{62}$$
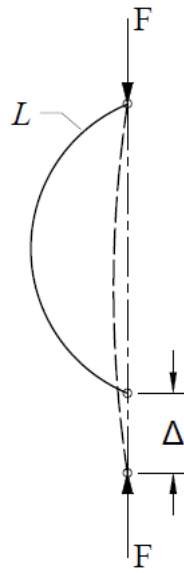
Figure 4.5 Pinned-Pinned Compliant Beam.
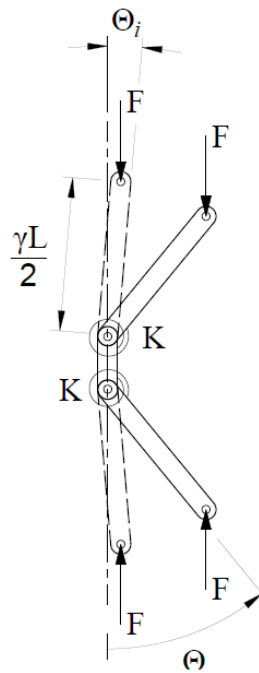
Figure 4.6 PRBM of Pinned-Pinned Compliant Beam.
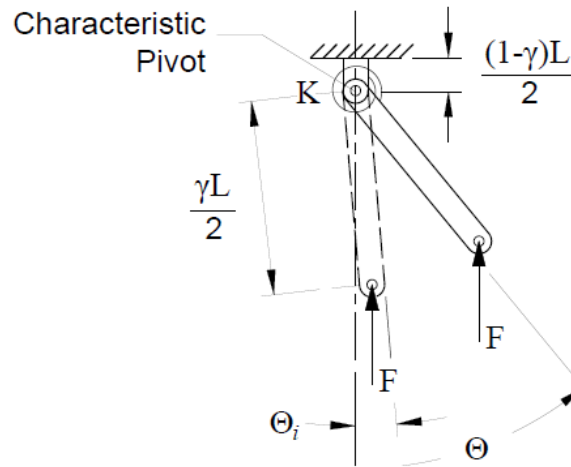
Figure 4.7 Half-Model of PRBM of Pinned-Pinned Compliant Beam.

where,

$$K = 2\gamma K_\Theta \frac{EI}{L} \tag{63}$$

$$I = \frac{wt^3}{12} \tag{64}$$

The constant-force equation is simplified with the Taylor/ Maclaurin series [85, 86],

$$F = \frac{2K(\Theta - \Theta_i)}{\gamma L \left(\Theta - \frac{\Theta^3}{3!} + \frac{\Theta^5}{5!} - \frac{\Theta^7}{7!}\right)} \tag{65}$$

It is simplified furthermore with the Taylor/Maclaurin series [85, 86] as the initial beam-end angle tends to zero,

$$F = \frac{2K}{\gamma L}(1 + 0.1667\Theta^2 + 0.0194\Theta^4) \tag{66}$$

The *characteristic load*, defined as the first value of the force exerted by the beam at zero-degree deflection, of the fixed-free compliant beam is as follows:

$$F_c = \frac{2K}{\gamma L} = 7.18 \; lb \tag{67}$$

It is well known that a member under compressive axial loading buckles when the force reaches a critical level, i.e., Euler's critical load [87-89]. Upon investigation, it is observed that the beam's characteristic load is almost identical to its critical buckling load. The Euler's critical load of a segment is dependent on its boundary conditions, so the formula for the fixed-free compliant beam is as follows.

$$P_{cr} = \frac{\pi^2 EI}{(L)^2} = 6.91 \; lb \tag{68}$$

The characteristic load factor, η_c, of the pinned-pinned compliant segment turns out to be the same as the fixed-free beam. This reinforces that the beam generates constant force in its post-buckling stage, as illustrated in Figure 4.8.

$$\eta_c = \frac{F_c}{P_{cr}} = \frac{4K_\Theta}{\pi^2} = 1.039 \tag{69}$$
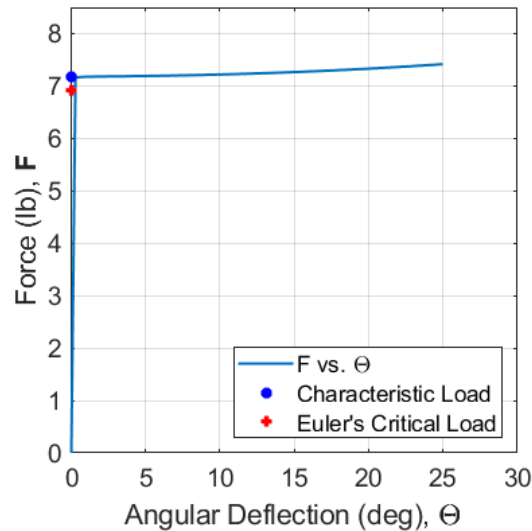
Figure 4.8 Force Vs. Deflection of Pinned-Pinned Compliant Beam, with its Characteristic and Critical Load.

4.4. FIXED GUIDED COMPLIANT BEAM

A fixed-guided, compliant beam grounded/fixed at one end and guided at the other to maintain the beam-end angle the same, i.e., the slope of the beam at the guided end remains constant while being able to translate in both directions as presented in Figure 4.9. Likewise, its PRBM, illustrated in Figure 4.10, consists of two characteristic pivots with two torsional springs [26, 68-71]. Similarly, it generates near-constant force without the need for optimization when subjected to axial loading. The force equation is derived from the half model of its PRBM, shown in Figure 4.11, due to symmetry.
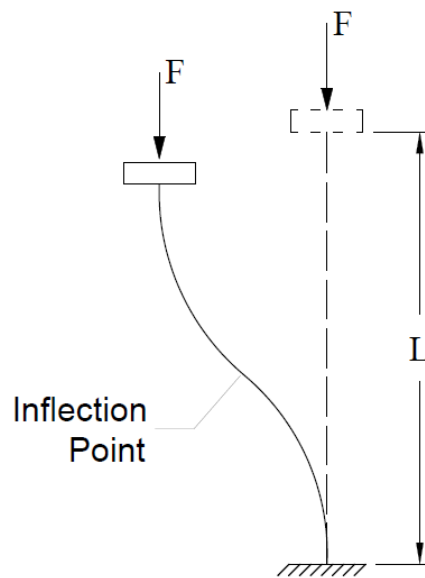
Figure 4.9 Fixed-Guided Compliant Beam.

$$\sum M_O = 0 :$$

$$F. \frac{\gamma L}{2} \sin \Theta = K(\Theta - \Theta_i) \qquad (70)$$

$$F = \frac{2K(\Theta - \Theta_i)}{\gamma L \sin \Theta} \tag{71}$$
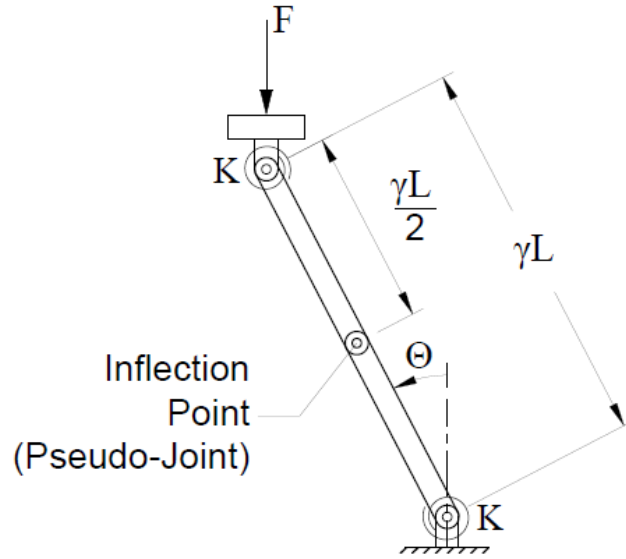
Figure 4.10 PRBM of Fixed-Guided Compliant Beam.
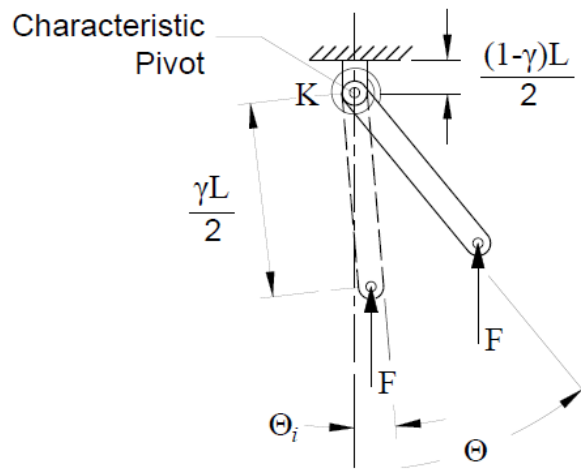
Figure 4.11 Half-Model of PRBM of Fixed-Guided Compliant Beam.

where,

$$K = 2\gamma K_\Theta \frac{EI}{L} \tag{72}$$

$$I = \frac{wt^3}{12} \tag{73}$$

Using the Taylor/Maclaurin series [85, 86],

$$F = \frac{2K(\Theta - \Theta_i)}{\gamma L\left(\Theta - \frac{\Theta^3}{3!} + \frac{\Theta^5}{5!} - \frac{\Theta^7}{7!}\right)} \tag{74}$$

As the initial beam-end angle tends to zero, it is further simplified with Taylor/Maclaurin series [85, 86],

$$F = \frac{2K}{\gamma L}(1 + 0.1667\Theta^2 + 0.0194\Theta^4) \tag{75}$$

Characteristic load factor, η_c, of the fixed-guided compliant beams turns out to be the same as the other two beams. It again reinforces that the beam generates constant force in its post-buckling stage, as depicted in Figure 4.12.

$$F_c = \frac{2K}{\gamma L} = 4.99 \; lb \tag{76}$$

$$P_{cr} = \frac{\pi^2 EI}{L^2} = 4.8 \; lb \tag{77}$$

$$\eta_c = \frac{F_c}{P_{cr}} = \frac{4K_\Theta}{\pi^2} = 1.039 \tag{78}$$

Each of the torsional springs of the pinned-pinned and fixed-guided beams is about twice the stiffness of that of a fixed-free beam, so these two compliant segment types are four times stiffer as there are two springs for the same beam length as the fixed-free

beam. Again, the initial beam-end angle needs to be close to zero degrees to be able to generate near-constant force, and the beams are slightly perturbed to facilitate buckling in the desired direction.
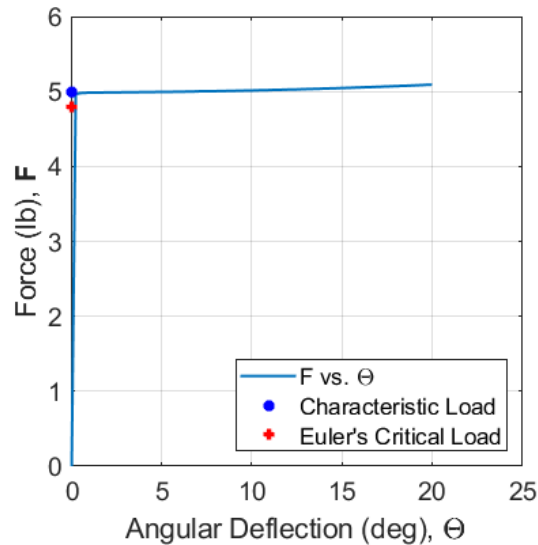
Figure 4.12 Force Vs. Deflection of Fixed-Guided Compliant Beam, With Its Characteristic and Critical Load.

4.5. COMPOUND- COMPLIANT SEGMENTS WITH SMALL-LENGTH FLEXURAL PIVOTS (SLFP)

A compound compliant beam consists of compliant and rigid segments. The compliant segment is considered as a small-length flexural pivot (SLFP) when its length is significantly smaller than the adjacent rigid segment [67, 91-92], as shown in Figure 4.13. Similar to the other compliant segments, the beams with SLFPs generate near-constant force when subjected to axial loading, without the need for design

optimization. The PRBM of an SLFP demonstrated in Figure 4.14 has a characteristic

pivot at its mid-point [68-71, 91-92] and is utilized to derive the force equations.
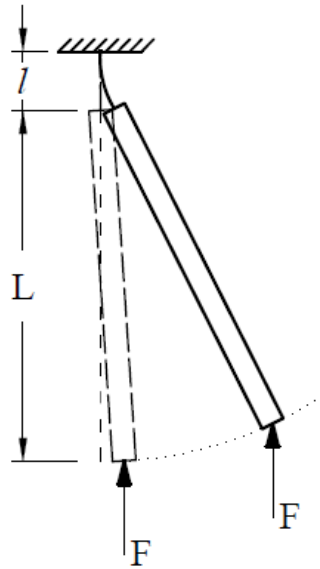
Figure 4.13 Compound Compliant Beam with Small-Length Flexural Pivot (SLFP).

From its static equilibrium position,

$\sum M_O = 0$:

$$F. \left(L + \frac{l}{2}\right) \sin \Theta \ = \ K(\Theta - \Theta_i) \tag{79}$$

$$F = \frac{K(\Theta - \Theta_i)}{\left(L + \frac{l}{2}\right) \sin \Theta} \tag{80}$$

where,

$$K = \frac{EI}{l} \tag{81}$$

$$I = \frac{wt^3}{12} \tag{82}$$
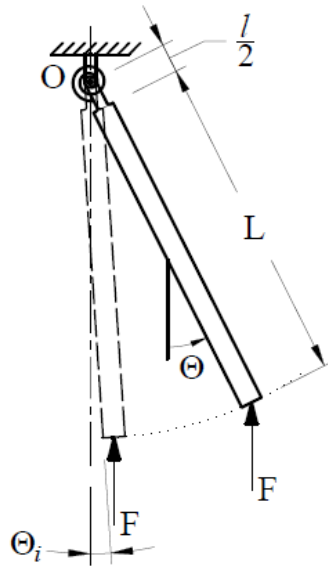
Figure 4.14 Pseudo-Rigid-Body Model of an SLFP.

The constant-force equation is simplified with the Taylor/ Maclaurin series [85, 86],

$$F = \frac{K(\Theta - \Theta_i)}{\left(L + \frac{l}{2}\right)\left(\Theta - \frac{\Theta^3}{3!} + \frac{\Theta^5}{5!} - \frac{\Theta^7}{7!}\right)} \qquad (83)$$

It is simplified furthermore with the Taylor/Maclaurin series and as the initial beam-end angle tends to zero,

$$F = \frac{K}{\left(L + \frac{l}{2}\right)}(1 + 0.1667\Theta^2 + 0.0194\Theta^4) \qquad (84)$$

Characteristic load of the compound compliant beam with an SLFP, at zero deflection,

$$F_c = \frac{K}{\left(L + \frac{l}{2}\right)} \qquad (85)$$

The force acting on the beam is calculated at its end, not at the end of the SLFP. Hence, its characteristic load cannot be compared with the critical load of buckling

for the compliant segment. Thus, the effective critical load at the end of the compound-compliant beam is estimated using its PRBM, as shown in Figure 4.15.
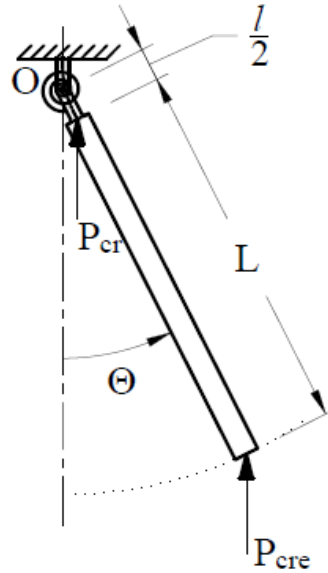
Figure 4.15 Pseudo-Rigid-Body Model of an SLFP
for Equivalent Euler's Critical Load.

From its static equilibrium position,

$$\sum M_O = 0:$$

$$P_{cre}\left(\frac{l}{2}\sin\Theta\right) = P_{cr}\left(L + \frac{l}{2}\right)\sin\Theta \tag{86}$$

$$P_{cre} = P_{cr}\left(L + \frac{l}{2}\right) \tag{87}$$

Additionally, the small-length compliant segment of the compound beam has a low slenderness ratio (for most cases of the SLFPs). For low slenderness-ratio SLFP, Johnson's parabolic formula, an alternative to Euler's critical load, is used to compute the critical

buckling load of the beam [93, 94]. The slenderness ratio of the compliant beam is calculated as follows.

$$slenderness\ ratio = \left(\frac{L_e}{r}\right) \tag{88}$$

where, r is the radius of gyration,

$$r = \sqrt{\frac{I}{A}} \tag{89}$$

Johnson's parabolic formula is as follows,

$$\sigma_{cr} = S_y - \frac{1}{E}\left(\frac{S_y}{2\pi} \cdot \frac{L_e}{r}\right)^2 \tag{90}$$

The critical load is then calculated as a product of the critical stress and the beam's cross-sectional area,

$$P_{cr} = \sigma_{cr} \cdot A \tag{91}$$

Upon examination, it is observed that the characteristic load of the beam is nearly the same as its estimated effective critical load, attesting that it exerts near-constant force in its post-buckling stage, as shown in Figure 4.16. As Johnson's parabolic formula is dependent on the material and geometric properties of the compliant segment, the ratio of the characteristic and critical load varies for the SLFPs.

Table 4.2 Forces of Fixed-Free Compound-Compliant Beam with SLFP

$F_c = 22.046\ lb$	$P_{cre} = 22.886\ lb$
$\eta_c = \dfrac{F_c}{P_{cre}} = 0.963$	
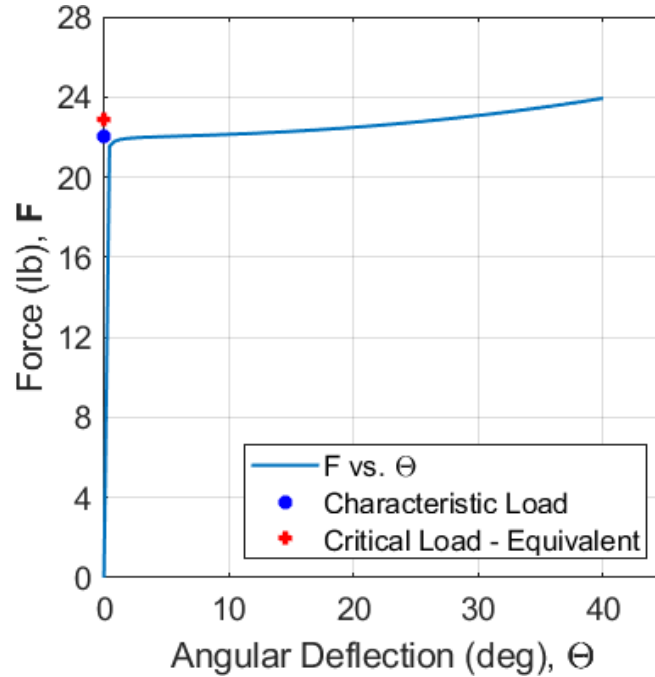
Figure 4.16 Force Vs. Deflection of Compound Compliant Segment With SLFP.

4.6. RIGID LINK WITH A TORSIONAL SPRING

A simple model of a rigid link pivoted to the ground at one end with a torsional spring, shown in Figure 4.17, generates a near-constant force upon loading it axially, as well. The link is slightly perturbed from its axis to allow it to deflect in the desired direction. The constancy of the force increases as the initial beam-end angle tends to zero degrees, signifying that no design optimization is necessary to generate near-constant force over its range of motion. It is scalable in both the size and the magnitude of the force. A numerical model is derived from its static equilibrium position, similar to the fixed-free compliant beam. Based on its model, the force-deflection is plotted in Figure 4.18.
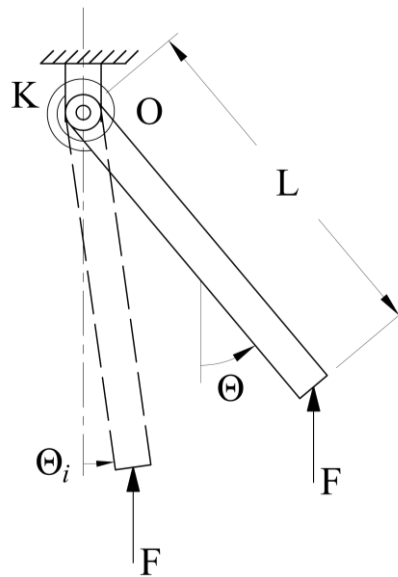
Figure 4.17 Rigid Link with a Torsional Spring.

$$\sum M_O = 0:$$

$$F.L \sin \Theta = \quad K(\Theta - \Theta_i) \tag{92}$$

$$F = \frac{K(\Theta - \Theta_i)}{L \sin \Theta} \tag{93}$$

The equation is simplified with the Taylor/Maclaurin series [85, 86] as the initial beam-end angle tends to zero,

$$F = \frac{K}{L}(1 + 0.1667\Theta^2 + 0.0194\Theta^4) \tag{94}$$

Table 4.3 Rigid Link Parameters

$L = 3in$	$K = 6 \; in/lb$
$\Theta_i = 0.01 \; degrees$	
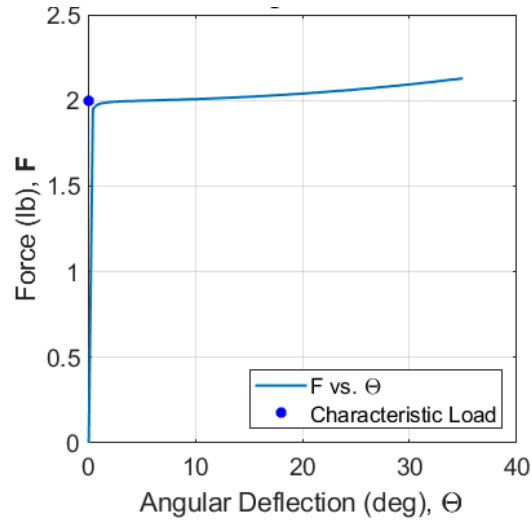
Figure 4.18 Force Vs. Deflection of Rigid Link with Torsional Spring.

The value of the force exerted at zero deflection, i.e., the characteristic load of the rigid-link arrangement is as follows.

$$F_c = \frac{K}{L} = 2 \ lb \tag{95}$$

It may also be observed that these equations are very similar to that of the fixed-free beam arrangement. The commonalities between these two models give the designer the freedom to develop a constant-force mechanism using either a rigid link with a torsional spring or a compliant beam.

4.7. SUMMARY

The theory that the simple, compliant segments exert near-constant force in their post-buckling stage without a need for design optimization has been investigated. Mathematical models are developed to study the performance of the three most common compliant segment types: fixed-free/pinned, pinned-pinned, and fixed-guided beams. The

pseudo-rigid-body model (PRBM) concept is utilized to model and analyze the force characteristics of the compliant beams under axial loading. It is noted that a fixed-free compliant beam under axial loading generates near-constant force over a significant range of its deflection. The same is true for pinned-pinned and fixed-guided compliant beams. They exert near-constant force, as well, when they undergo buckling due to axial loading. The force equations are derived from their respective PRBMs. These equations are comparable to each other, as the half-models of the pinned-pinned and fixed-guided PRBMs are similar to the PRBM of the fixed-free compliant beam. It is observed that the constancy of the force is only dependent on the initial beam-end angle and not on any other geometric or material properties of the beam. It increases as the initial angle tends to zero degrees, and as the initial angle increases, the beams act as a soft spring. The characteristic load of the compliant segment, defined as the first value of the force exerted at zero deflection, is observed to be nearly the same as its Euler's critical load, demonstrating the constancy of the force exerted by the compliant beams is predominantly due to this phenomenon.

Additionally, the compound-compliant segment with an SLFP and rigid-link arrangements are investigated, and similar analytical models are developed for constant force generation. Likewise, the characteristic load of the SLFP is nearly the same as its critical load, which is estimated by Johnson's parabolic formula because of its low slenderness ratio.

5. EXPERIMENTAL VALIDATION OF CONSTANT-FORCE COMPLIANT SEGMENTS AND KERNEL OF CONSTANT-FORCE MECHANISMS

5.1. INTRODUCTION

The proposed theory that simple compliant segments generate constant force in their post-buckling state when subjected to axial compressive loading, and the results obtained from the PRBM-based analytical model are experimentally validated for the three rudimentary segment types, i.e., fixed-free, pinned-pinned, and fixed-guided beams. This investigation further exemplifies that the proposed theory is the very kernel for generating constant force by the existing constant-force mechanisms.

5.2. EXPERIMENTAL VALIDATION

A test setup is developed for each compliant segment type with a deflector to initiate deflection in the desired direction. They are machined out of Aluminum and are equipped with roller/ball bearings as needed, and also have guides to ensure smooth motion. The experiments are conducted on the Instron® Universal Testing Machine (UTM) 8000, and the recorded values are compared against the theoretical results.

5.2.1. Fixed-Free Compliant Beam. The fixed-free test setup, shown in Figure 5.1, consists of two spring-steel, compliant beams that are fixed at one end to the top plate. The beams have rollers attached at the free ends to eliminate or minimize the effect of friction on the test results. The top-plate assembly is guided by a steel rod and a Delrin sleeve to travel vertically with little to no frictional resistance. A deflector (in red) is placed around the Delrin sleeve at the free end of the beams to slightly perturb those outwards to ensure that they deflect in the desired direction.
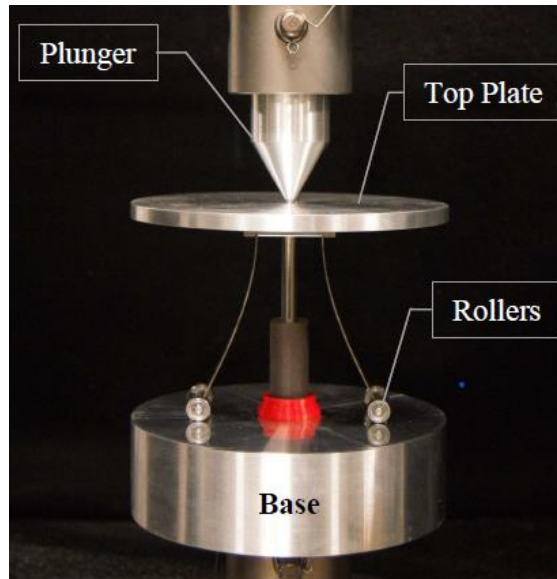
Figure 5.1 Test Setup of Fixed-Free Compliant Beam.
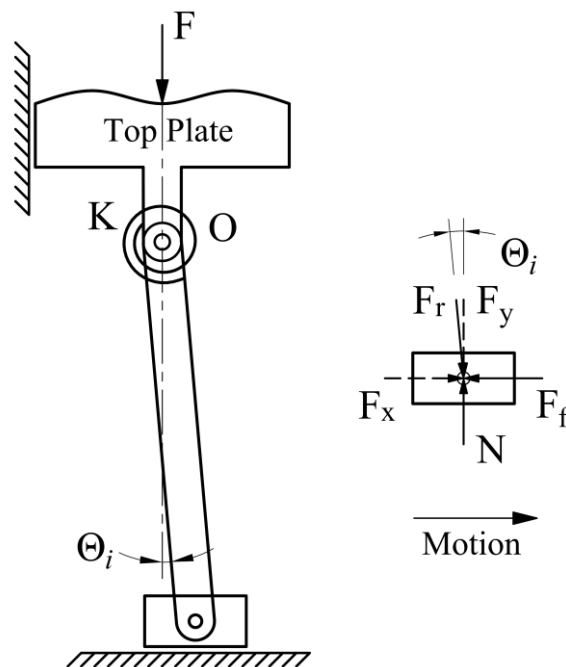
Figure 5.2 PRBM of Beam Assembly in its Static Equilibrium and FBD of its Slider.

The friction between the beam and the base affects the initial beam-end angle, which determines the constancy of the force, as shown in its static equilibrium position and the free-body diagram of the slider in Figure 5.2.

$$\sum F_Y = 0 : \quad N = F_y = F_r \cos \Theta_i \tag{96}$$

For the slider to be in motion,

$$\sum F_X \geq 0 : F_x \geq F_f \tag{97}$$

$$F_f = \mu N \quad \& \quad F_x = F_r \sin \Theta_i \tag{98}$$

$$F_r \sin \Theta_i \geq \mu F_r \cos \Theta_i \tag{99}$$

$$\tan \Theta_i \geq \mu \quad \textbf{or} \quad \mu \leq \tan \Theta_i \tag{100}$$

For a small initial angle, the coefficient of friction must be very low, which is only possible with rollers at the free end.

$$for \ \Theta_i = 0.1° \Rightarrow \ \mu \leq 0.00174 \tag{101}$$
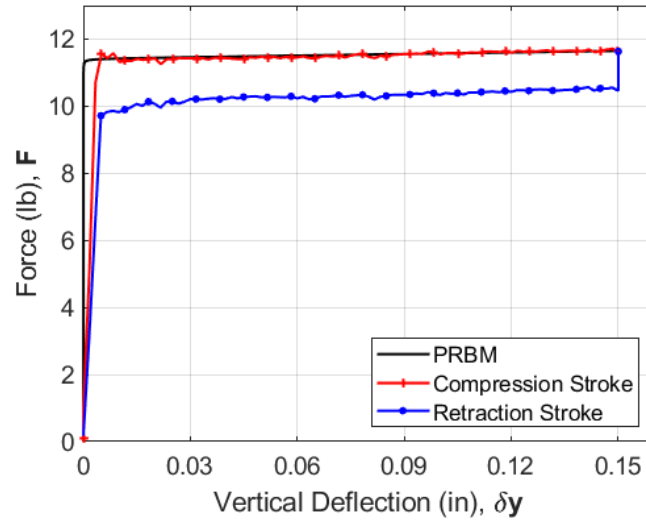
Figure 5.3 Experimental Results for Fixed-Free Compliant Beam.

The experimental results for the fixed-free compliant beam are presented below in Figure 5.3. It may be noted that there is a difference in force between compression and retraction strokes (*Hysteresis effect*), which can be alluded to due to the *Coulomb friction*. It may also be observed that the force predicted by the analytical model is not at the median of compression & retraction strokes, as is generally the case for the Hysteresis effect.
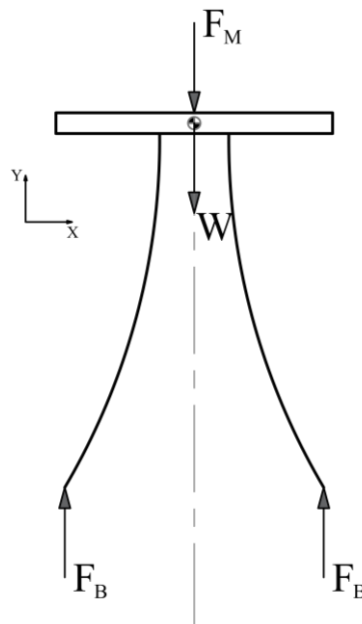
Figure 5.4 Static Equilibrium Position of The Top Plate Assembly.

It is determined experimentally that the UTM machine reads a net value of forces from the beams and the weight of the top plate, which is explained with a free-body diagram of the top-plate assembly in its static equilibrium position, shown in Figure 5.4.

$$\sum Y = 0 :$$

$$2F_B - W_{plate} - F_M = 0 \tag{102}$$

$$F_M = 2F_B - W_{plate} \qquad (103)$$

The force predicted by the PRBM-based analytical model is appropriately adjusted by deducting the weight of the top-plate assembly for all the test setups.
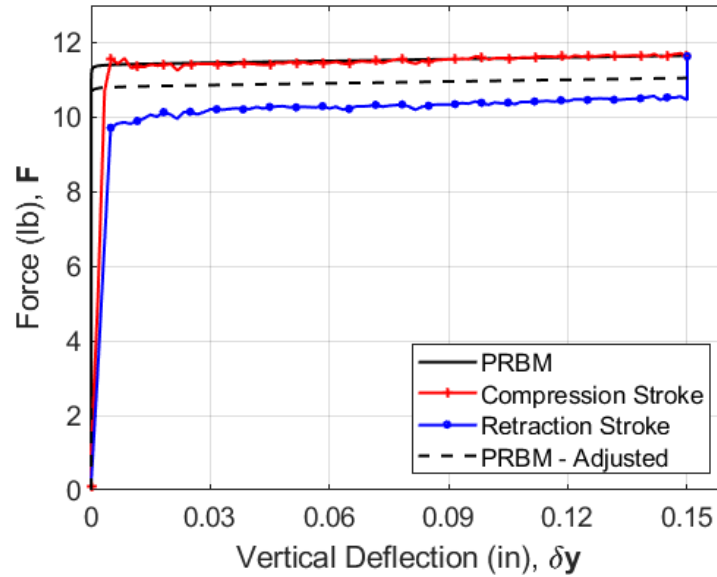
Figure 5.5 Experimental Results for Fixed-Free Compliant Beam - Adjusted.

Table 5.1 The Beam and PRBM Parameters for Fixed-Free Test Setup

Spring Steel's Modulus of Elasticity, $E = 30e^6\ psi$	
thickness, $t = 0.025 \pm 0.001"$	*width, $w = 0.5 \pm 0.002"$*
Length of the beam, $L = 3 \pm 0.002"$	
Characteristic Radius Factor, $\gamma = 0.8156$	
Stiffness Coefficient, $K_\Theta = 2.56597$	
Weight of the Top Plate, $W_{plate} = 0.6\ lb$	

The adjusted theoretical force profile aligns at the center of the experimental values/profiles. The experiment validates the theory that compliant beams under axial loading generate constant force in their post-buckling stage.

5.2.2. Pinned-Pinned Compliant Beam. In the case of the pinned-pinned test setup, illustrated in Figure 5.6, consists of four spring-steel, compliant beams that rest in the grooves machined into the top plate and the base forming a half joint, which allows the beams to rotate freely at both ends. This setup also has a guide-rod with a Delrin sleeve to ensure a smooth vertical motion. Similar to the fixed-free test setup, a deflector (in orange) is placed around the Delrin sleeve at the center of the beams' length to perturb the beams slightly off-axis to let them deflect in the desired outward direction.
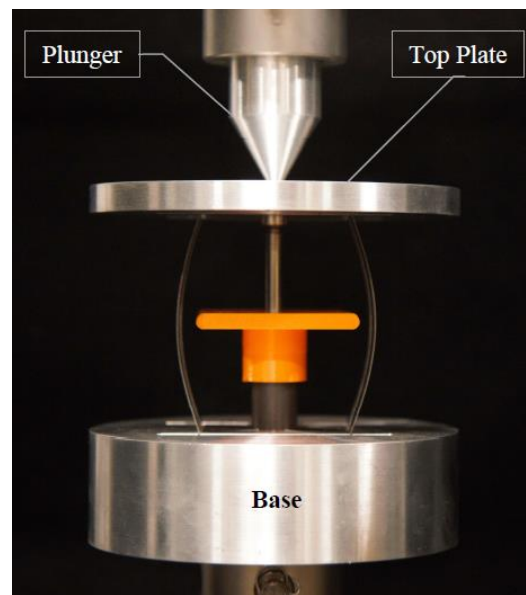
Figure 5.6 Pinned-Pinned Compliant Beam Test Setup on Instron UTM.

Similarly, the weight of the top plate is taken into account while comparing the theoretical forces with the experimental results, presented in Figure 5.7. This experimental

result further validates the theory for pinned-pinned compliant beams, which generate constant force in the post-buckling stage, as it matches nearly with the theoretical plot.
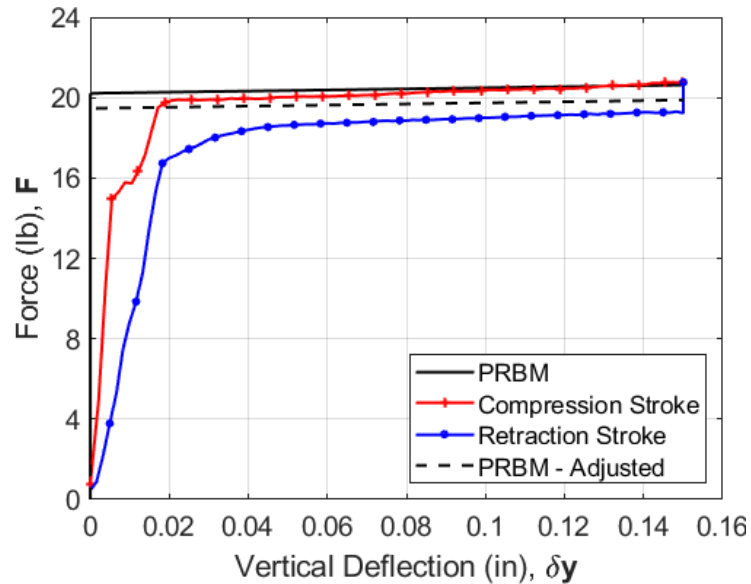
Figure 5.7 Experimental Result for Pinned-Pinned Compliant Beams.

Table 5.2 The Beam and PRBM Parameters for Pinned-Pinned Test Setup

Spring Steel, $E = 30e^6$ psi	
$t = 0.015 \pm 0.001"$	$w = 0.5 \pm 0.002"$
$L = 3 \pm 0.002"$	$W_{plate} = 0.75\ lb$
$\gamma = 0.8156$	$K_\Theta = 2.56597$

A minor discrepancy in the experimental results may be observed for the pinned-pinned test setup, especially at the initial phases of the stroke. It can be largely attributed

to the sharp ends of the beams not being able to rest uniformly in the concave grooves machined into the base and the top plate. During the initial phase of the stroke, the beams align into the grooves as the setup is being loaded, and the experimental force values tend to merge with the theoretical force. The tolerances in the beams' length and the deflector, along with surface errors at the beam-ends and the grooves are the potential causes for the mismatch in the force plots.
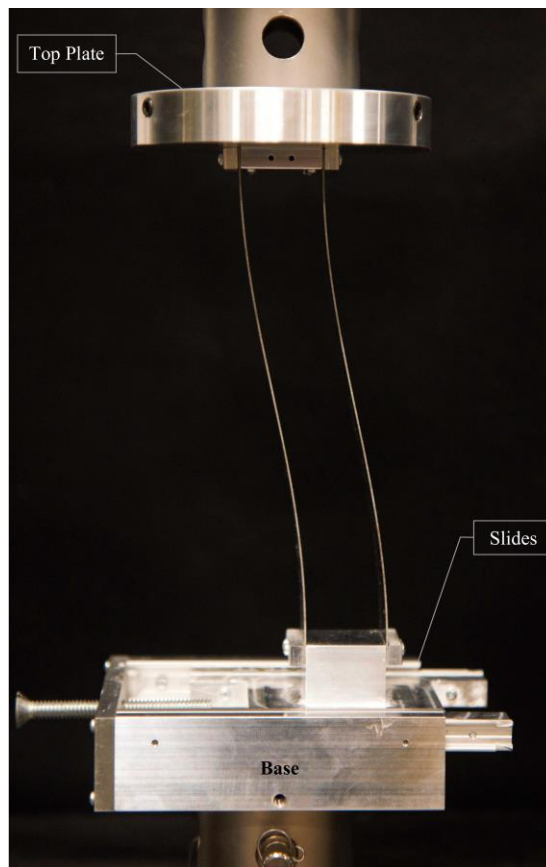
Figure 5.8 Fixed-Guided Compliant Beam Test Setup on Instron UTM.

5.2.3. Fixed-Guided Compliant Beam. The fixed-guided test setup, illustrated in Figure 5.8, consists of two spring-steel beams, which are fixed to the top plate at one end

and the other to a slider at the base. The slider allows the beams to translate but constrains their rotation, which makes it the guided end of the test setup. The leadscrew provided at the base perturbs the slider so that the beams are slightly off-axis, which lets them deflect in the desired direction.

Similarly, the weight of the top plate is considered while comparing the theoretical forces with the experimental values. The experimental result for fixed-guided compliant beams, shown in Figure 5.9, further validates the theory that they generate constant force in the post-buckling stage, as it matches closely with the analytical results.
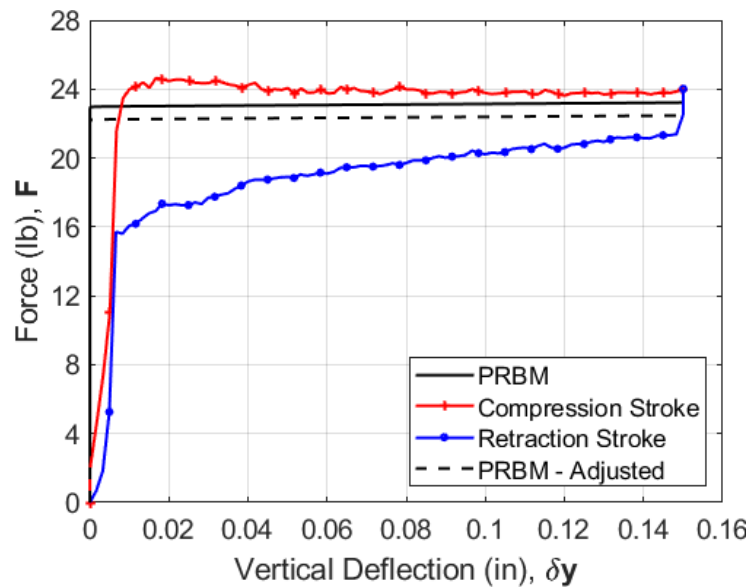
Figure 5.9 Experimental Result for Fixed-Guided Compliant Beams.

It may also be observed that the experimental results for the fixed-guided test setup have slightly deviated from the theoretical plot, especially in the retraction stroke towards the end of the cycle. It is mainly due to the lash in the draw slides used for the guided end of the beams at its base (too much clearance and slack). During the compression stroke,

the carriage members that are inside the rails of the slider coast along the bottom side of the railing. However, in the retraction stroke, it slides against the top side. The slack in them also causes the carriage skew while translating, esp. in the retraction stroke because of the angle of the resultant force acting on it. These are the potential reasons for the discrepancies in test results for the fixed-guided beams.

Table 5.3 The Beam and PRBM Parameters for Fixed-Guided Test Setup

Spring Steel, $E = 30e^6\ psi$	
$t = 0.025 \pm 0.001"$	$w = 1 \pm 0.002"$
$L = 6 \pm 0.002"$	$W_{plate} = 0.75\ lb$
$\gamma = 0.8156$	$K_\theta = 2.56597$

5.3. THE KERNEL OF THE EXISTING COMPLIANT CONSTANT-FORCE MECHANISM

A few of the existing compliant constant-force mechanisms are examined now with the premise that simple compliant segments generate near-constant force to establish that the proposed theory is the kernel of the CFM to produce a constant force. As a case study, one of the configurations of the compliant slider-crank CFMs, class 1A as shown in Figure 5.10 [24-28], is considered to investigate and establish the relationship between the proposed theory and the existing constant-force mechanisms.

The class 1A configuration has a compliant segment at its slider end, and it may be observed that its static equilibrium position, presented in Figure 5.11, is identical to the fixed-free compliant beam under the axial load. The reaction force exerted at the beam end is the same as the force exerted at the slider. Hence, the compliant segment of class 1A configuration is a fixed-free beam under axial loading that generates near-constant force.
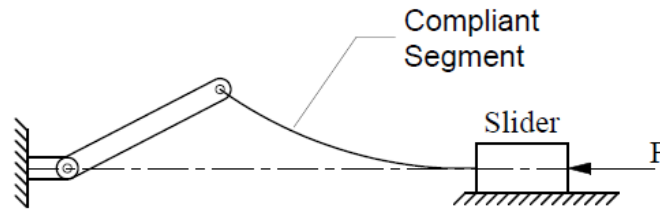
Figure 5.10 Class 1A Slider-Crank, Compliant Constant-Force Mechanism.

Figure 5.11   Compliant Segment of Class 1A Slider-Crank, CFM with Reaction Force.

A compliant cam-follower mechanism developed by Midha et al. [28], which is based on a class 1A CFM to exert constant force, is presented in Figure 5.12. The cam operates as a pseudo-crank of the mechanism, and the follower beam in its static equilibrium position is just a compliant beam under axial load. Hence, this arrangement behaves similarly in generating constant force.

From this investigation, it is evident that the constancy of the force for the large part is from the buckling of the compliant beam. The function of the cam or the mechanism is to assist the compliant beam (under axial loading) to produce an exact constant load over the desired range of deflection. It establishes the fact that the proposed theory is the kernel of the CFMs for the generation of constant force.
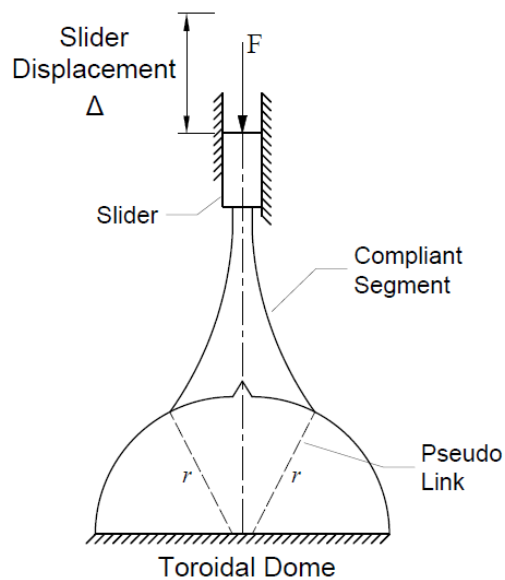
Figure 5.12   Compliant Constant-Force Mechanism with Toroidal Cam.

5.4. SUMMARY

The proposed theory and the force-displacement characteristics predicted by the PRBM-based analytical model for constant force are experimentally validated for three rudimentary compliant segment types. Roller bearings are utilized in the test setups to minimize or eliminate the effects of friction on the results. Also, beam-deflectors are employed to slightly perturb the beams before loading them to ensure they deform in the

desired direction. The analytical results are adjusted to include the effects of gravity load on the top plate of the test setups. The experimental results match the theoretical force profile for fixed-free, pinned-pinned, fixed-guided beams. Hence, it validates the proposed theory that simple, compliant segments produce near-constant force in their post-buckling stage. However, there are minor discrepancies in the results for the pinned-pinned and fixed-guided test setups, due to machining and assembly errors.

The proposed theory is further exemplified with a few examples of the existing CFMs. An optimized mechanism or cam surface at the beam end may generate an exact constant force over large deflections but is not needed to produce a near-constant force. A simple arrangement of compliant beams under axial loading can achieve that without the need for any optimization.

6. DESIGN AND ANALYSIS OF A UNIQUE CONSTANT-FORCE COMPLIANT MECHANISM – CANTED SPRING

6.1. INTRODUCTION

A growing interest in constant-force devices for applications in diverse fields has led to the development of several compliant constant-force mechanisms (CFMs) for specific needs and requirements. However, most of them are not easily scalable, especially in their construction. This research focuses on a novel compliant constant-force mechanism, Canted Spring, which is relatively simple to scale up or down to serve various engineering applications.

In this section, the canted spring is formally defined to distinguish it from the other compliant mechanisms that can exert constant force. It also has a few unique advantages over the rest of the CFMs. A type synthesis of the canted spring is executed based on its PRBM to develop all the possible configurations. It is recognized that a few of them have the best possibility to exert constant force based on the recent findings that compliant segments generate near-constant force when subjected to axial compressive loading (see section 5). A dimensional-synthesis optimization is developed to determine the best combinations of the PRBM of the canted spring to exert constant force over its deflection. A design methodology to construct the desired mechanism based on the optimized configurations is discussed with examples. The force-displacement characteristics of other sets of non-constant force configurations were also presented.

6.2. DEFINITION AND ADVANTAGES

A compliant mechanism in a canted form, which comprises a negative pitch segment (slanted inwards) along with a positive pitch segment, is henceforth termed a Canted Spring, as shown in Figure 6.1. The positive pitch segment of the canted springs is either cantilevered or pivoted to the ground, and the other end at the negative pitch segment is free to slide. The inspiration for this canted profile [95] is from canted coil springs, which exert near-constant force across a partial range of their deflection [96]. However, these canted springs have the potential to exert constant force over a large part of their deflection.
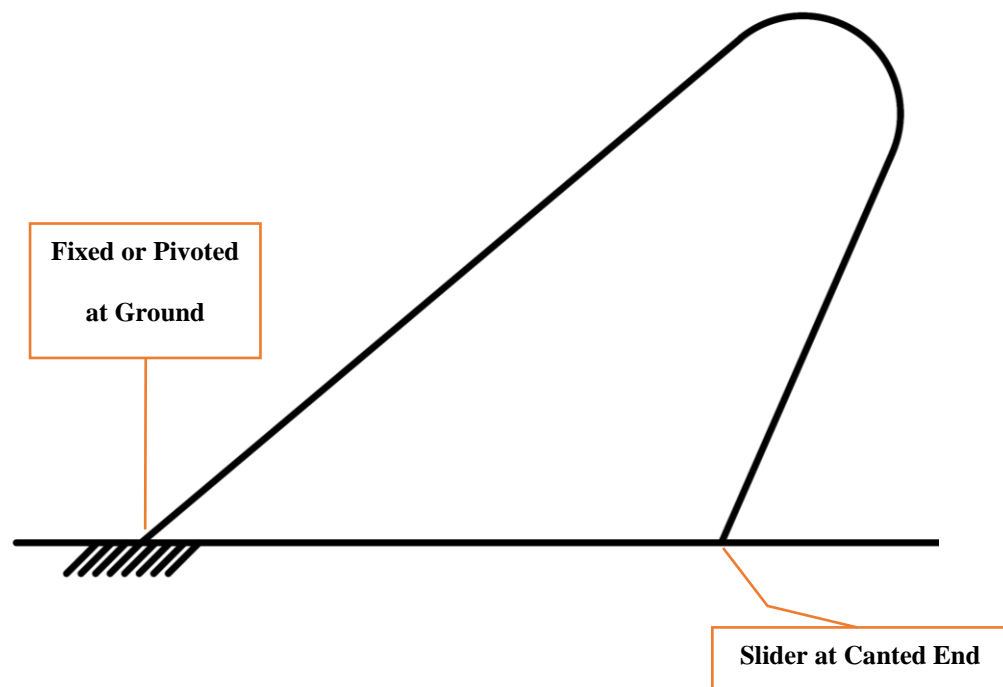
Figure 6.1   Canted Spring Profile

Canted springs have a few unique advantages over the other existing compliant CFMs, stated as follows:

- They are compact in their construction as half of the mechanism is slanted inwards, unlike the other slider-crank-based CFMs.

- It can be deployed as a single unit or in modules, whereas the other CFMs are often used in pairs or modules to neutralize the transverse forces.

- They do not need external guide rods or top plates/surfaces to contain the springs, as they can be assembled on a single flat surface.

- It could either be a constant-force or soft spring based on its boundary conditions.

Kinematic synthesis of the canted spring, like any mechanical system, is the means to design for specified motion and function [97], which has two phases: i) Type Synthesis and ii) Dimensional Synthesis. A rigid-body kinematic chain was developed to identify all the possible configurations of canted spring during the type-synthesis phase. Dimensional synthesis determines the geometry of the compliant mechanism using its PRBM with the objective of generation of constant force.

6.3. TYPE SYNTHESIS OF CANTED SPRING

Type Synthesis is described as the definition of the proper type of mechanism best suited to the problem [97-98]. For the canted spring pseudo-rigid-body kinematic chain, Numerical Synthesis, a subset of type synthesis, determines the number of links and the mechanism degrees of freedom to perform a specified task.

6.3.1. Pseudo-Rigid-Body Kinematic Chain. The pseudo-rigid-body (PRB) kinematic chain of the canted spring is determined by investigating its behavior under

loading. It is always determined to be loaded at its apex. The undeformed profiles of the canted springs and their deformations for various topologies were obtained through Finite Element Analysis (FEA) & Chain Algorithm simulations, as shown in Figure 6.2.
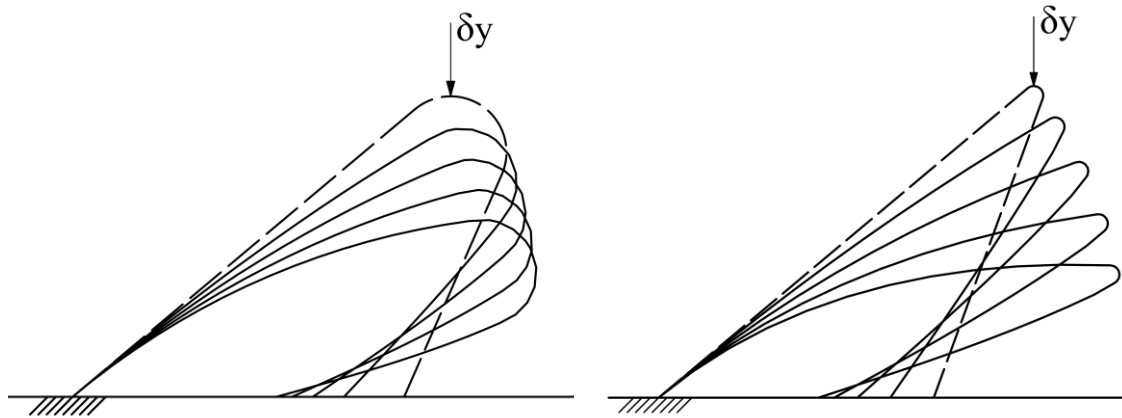
Figure 6.2   Deformations of Different Canted Spring Profiles
(FEA – Ansys® Mechanical APDL & Chain Algorithm)

It is observed that most of the deflection in the canted springs is at two locations on the continuum, thus, two pin joints are specified at the respective locations. It is the same behavior for all the topologies of the springs under observation. The point of application of force is treated as a rigid location, if not, it would behave as a pseudo-joint. It results in a four-bar slider mechanism as the kinematic chain of the canted spring. It may be noted that the beam end of the negative-pitch segment is a half joint that rotates and slides, hence, represented by a link with a revolute joint and a prismatic pair. This does not affect the degrees of freedom and the kinematic behavior of the mechanism. This investigation draws parallels with the research conducted by Midha and Bagivalu [99] on static mode shapes in compliant mechanisms and their appropriate pseudo-rigid-body models.
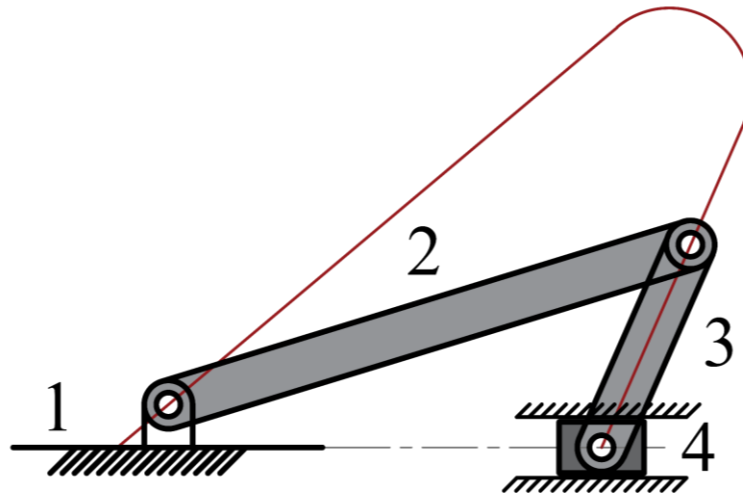
Figure 6.3   Rigid-Body Kinematic Chain of Canted Spring

The beams' resistance to bending is represented by torsional springs, not shown in the figure, which forms the pseudo-rigid-body model (PRBM) of the canted spring, discussed in the later sections.

6.3.2. Canted Spring Configurations. Type synthesis of canted spring employs its PRB kinematic chain to determine all possible combinations of compliance in the mechanism that exhibits the same kinematic behavior. Initially, a heuristic approach of type synthesis of the canted spring derived six configurations by deducing the mechanism combinations by replacing the two revolute joints in the kinematic chain with compliance [100]. The revolute & prismatic joints at the slider of the kinematic chain are not replaced by compliance for this type-synthesis analysis because it is a sliding half-joint (higher pair) without any deformations. The determined six configurations are grouped into three categories based on the location of compliance in the mechanisms. The first category has two mechanisms with compliance at both the identified pin joints. The second and third

category mechanisms, two of each, have compliance at only one location, either at the ground pin joint (joint 1) or at the negative-pitch segment (joint 2).

Subsequently, a systematic and formalized approach developed by Bagivalu Prasanna [101] yielded two additional configurations, which have been classified into the first category mechanisms.

Formalized Enumeration Process – Many different methodologies have been developed for the type synthesis of compliant mechanisms [102]. One such approach proposed by Murphy [24] is a rigid-body-replacement method that uses the PRBM technique to identify the equivalent rigid-body kinematic chain of the compliant mechanism for the analysis. A recent investigation by Bagivalu Prasanna and Midha [101] further simplified and discovered the benefits of considering the PRBM directly in the type synthesis process for detecting the isomorphism. This simplified formal approach, which uses existing graph theory and the compliance number (C) concept [103], is employed to enumerate all the possible configurations of the canted spring. The compliance number (C) represents the compliance information in the matrix that depicts the link connections in the PRBM [101]. The matrix form referred to as the PRBM Adjacency Matrix (A) is then utilized for deriving all the PRBM combinations without isomorphism [101].

The formal type synthesis of the canted spring is enabled by the steps developed by Bagivalu Prasanna and Midha [101], as stated below. Steps 1 to 5 identify the basic structure of the PRBM, and the required compliance content (C_{min} and C_{max}) based on the design requirements. Steps 6 through 8 are for the enumeration process of the PRBMs and their respective compliant configurations. The process is briefly summarized as follows.

Step 1: Required degrees-of-freedom (F_c) for the canted spring, $F_c = 1$. Fc signifies the maximum number of inputs provided to a compliant mechanism.

Step 2: A rigid-body chain for the spring is determined based on its F_c, which is a four-bar slider mechanism, the same as the one presented in section 6.3.1.

Step 3: The minimum value of the compliance number (C_{min}) is computed as follows:

$$C_{min} = F_c - F_r \qquad (104)$$

where Fr is the freedom number and signifies the kinematic indeterminacy of the structure. It is equal to zero for the canted spring to ensure there is no rigid-body motion.

Step 4: Necessary design requirements for the canted spring are:

  i.   The slider pair between links 1 & 4 and the revolute joint connecting links 3 & 4 are not treated as characteristic pivots, as explained in the previous section

  ii.   Links 1 & 4 are treated as rigid links, hence the spring is regarded as a partially compliant mechanism for the enumeration process

  iii. Subsequently, the PRBM of the mechanism has only two torsional springs

  iv.   The force acting on the canted spring is applied at the apex of the rigid segment. Therefore, link 2 may be replaced only by a compound-compliant segment

Step 5: The maximum value of the compliance number (C_{max}) is determined based on the requirements:

$$C_{max} = 2 \qquad (105)$$

Step 6: The possible PRBM combinations of the canted spring are enumerated by using adjacency matrices and the values of C_{min} & C_{max}. The adjacency matrix of the mechanism is constructed from its kinematic graph [101]. The elements of the matrices are defined as follows.

(i, j)

$$= \begin{cases} 0, & \textit{if link } \textbf{\textit{i}} \textit{ is not connected to link } \textbf{\textit{j}} \\ 1, & \textit{if link } \textbf{\textit{i}} \textit{ is connected to link } \textbf{\textit{j}} \textit{ with a kinematic pair} \\ C, & \textit{if link i is connected to link j with a characteristic pivot} \\ & \qquad \qquad \textit{and torsional spring} \\ -1, & \textit{if the link is a ground link} \end{cases} \qquad (106)$$

i. The adjacency matrix (A) of the equivalent rigid-body mechanism of the canted spring is as follows. The elements highlighted in red represent the rigid joints and are not replaced with C (compliance) for the enumeration process

$$A = \begin{bmatrix} 0 & 1 & 0 & 1 \\ 1 & 0 & 1 & 0 \\ 0 & 1 & 0 & 1 \\ 1 & 0 & 1 & 0 \end{bmatrix} \qquad (107)$$

ii. Matrix A being symmetric, the elements above the main diagonal are considered and expressed in an uncompressed sequence, S. By eliminating the zeroes of the sequence S, a compressed sequence, s, is created

$$S = 101101 \qquad (108)$$

$$s = 1111 \qquad (109)$$

iii. In the enumeration process, links 2 & 3 and the associated kinematic pairs between 1 & 2 and 2 & 3 (shown in Figure 6.3) are considered for replacement with compliance, i.e., $C_{max} = 2$. Hence, the possible number of PRBM combinations are:

$$C_2^2 + C_1^2 = 3 \; configurations \qquad (110)$$

iv. C_2^2 represents the number of PRBM combinations with two characteristic pivots and C_1^2 for the PRBMs with one characteristic pivot. Their corresponding uncompressed (S_i) and compressed sequences (s_i) are tabulated in Table 6.1, and

the respective adjacency matrices that represent the pseudo-rigid-body model (PRBM) combinations are in Table 6.2.

Table 6.1 Compressed (*s*) and Uncompressed (*S*) Sequences for the PRBM Combinations

PRBM Configurations for $C = 2$		PRBM Configurations for $C = 1$	
Compressed Sequence (s_i)	*Compressed Sequence (S_i)*	*Compressed Sequence (s_i)*	*Compressed Sequence (S_i)*
$s_\mathrm{I} = C1C1$	$S_\mathrm{I} = C01C01$	$s_\mathrm{II} = C111$	$S_\mathrm{II} = C01101$
		$s_\mathrm{III} = 11C1$	$S_\mathrm{III} = 101C01$

Table 6.2 Adjacency Matrices for the PRBM Combinations

Adjacency Matrices for PRBM Configurations with $C = 2$
$$A_\mathrm{I} = \begin{bmatrix} 0 & C & 0 & 1 \\ C & 0 & C & 0 \\ 0 & C & 0 & 1 \\ 1 & 0 & 1 & 0 \end{bmatrix}$$
Adjacency Matrices for PRBM Configurations with $C = 1$
$$A_\mathrm{II} = \begin{bmatrix} 0 & C & 0 & 1 \\ C & 0 & 1 & 0 \\ 0 & 1 & 0 & 1 \\ 1 & 0 & 1 & 0 \end{bmatrix}$$
$$A_\mathrm{III} = \begin{bmatrix} 0 & 1 & 0 & 1 \\ 1 & 0 & C & 0 \\ 0 & C & 0 & 1 \\ 1 & 0 & 1 & 0 \end{bmatrix}$$

Step 7: A_I matrix has a compliance number of 2, which is different from A_{II} & A_{III} ($C =$ 1). The location of the characteristic pivot in the PRBMs of A_{II} & A_{III} are different from one another, although they have the same compliance number ($C = 1$). Since all the PRBMs are not identical, the compliant mechanisms derived from them are non-isomorphic.

Step 8: All possible compliant mechanisms are enumerated for each of the PRBM combinations.

Case a: For the PRBM combination associated with the A_I matrix ($C = 2$), the possible end conditions of the rigid links are listed in Table 6.3. The compliant mechanism configurations enumerated from this PRBM are classified as Category I canted springs, as shown in Figure 6.4

Table 6.3 Possible End Conditions for the Links and the Corresponding Compliant
Segment Type Combinations in Case a.

Link 2 End Conditions	Link 3 End Conditions	Link 4 End Conditions
CC	*C*1	11
SLFP – SLFP	SLFP – Revolute Joint	Revolute Joint – Slider
Fixed – Fixed	SLFP – Revolute Joint	Revolute Joint – Slider
SLFP – Fixed	Fixed – Revolute Joint	Revolute Joint – Slider
Fixed – SLFP	Fixed – Revolute Joint	Revolute Joint – Slider

Case b: The possible end conditions of the rigid links for the PRBM of the A_{II} (C = 1) matrix are listed in Table 6.4. The enumerated compliant mechanisms are classified as Category II canted springs, as shown in Figure 6.5
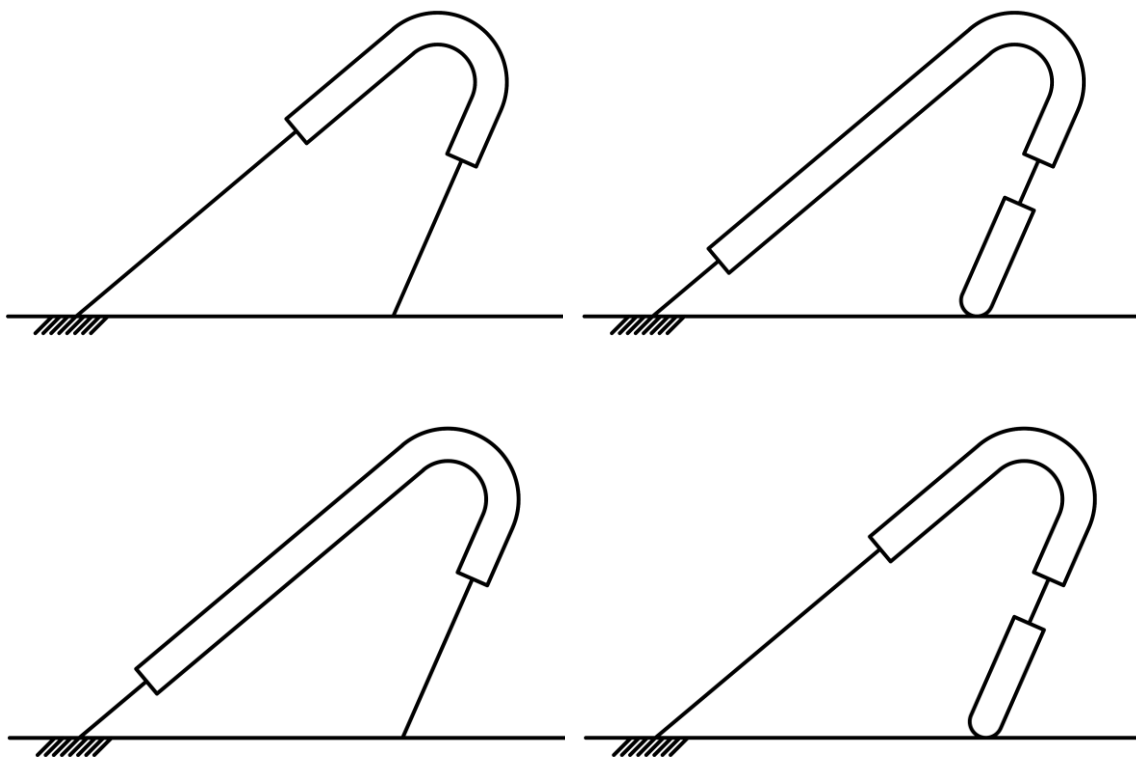
Figure 6.4   Category I – Class 2A
Two Pin-Joints Replaced with Discreet Compliance

Table 6.4 Possible End Conditions for the Links and the Corresponding Compliant
Segment Type Combinations in Case b.

Link 2 End Conditions	Link 3 End Conditions	Link 4 End Conditions
$C1$	11	11
SLFP – Revolute Joint	Revolute Joint – Revolute Joint	Revolute Joint – Slider
Fixed – Revolute Joint		
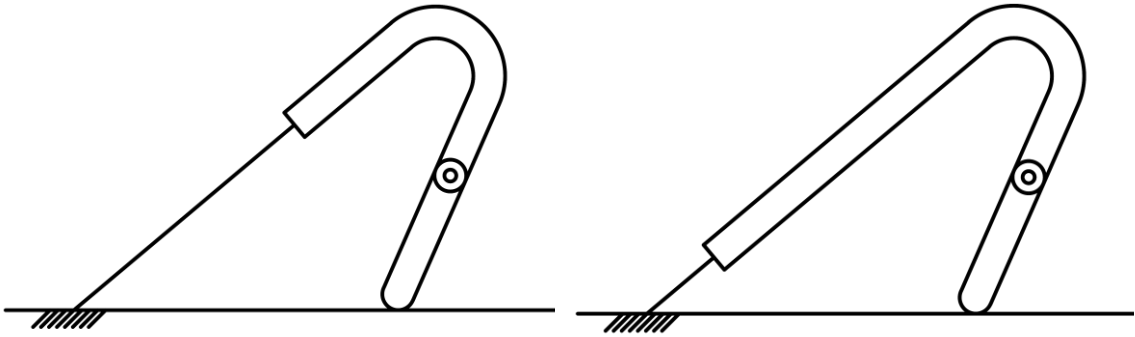
Figure 6.5   Category II – Class 1A
Pin-Joint at Ground Replaced with Discreet Compliance

Case C: For the PRBM combination A_{III} matrix ($C = 1$), the rigid links' possible end conditions are listed in Table 6.5. The respective compliant mechanisms enumerated are classified into Category III canted springs, as shown in Figure 6.6

Table 6.5 Possible End Conditions for the Links and the Corresponding Compliant Segment Type Combinations in Case c.

Link 2 End Conditions	Link 3 End Conditions	Link 4 End Conditions
1C	C1	11
Revolute Joint – SLFP	SLFP – Revolute Joint	Revolute Joint – Slider
Revolute Joint – Fixed	Fixed – Revolute Joint	

These categories are analogous to the classification of slider-crank-based compliant CFMs developed by Midha et al. [24-25, 27-28]. The force-displacement behavior of category III springs (two configurations) is the primary focus of this research effort, as they have the best potential for exerting constant force. From the recent research findings, it is

evident that axially loading the beams is essential for generating near-constant force, which is a certainty for category III configurations, i.e., negative pitch compliant segment (fixed-free beam) under axial loading conditions.
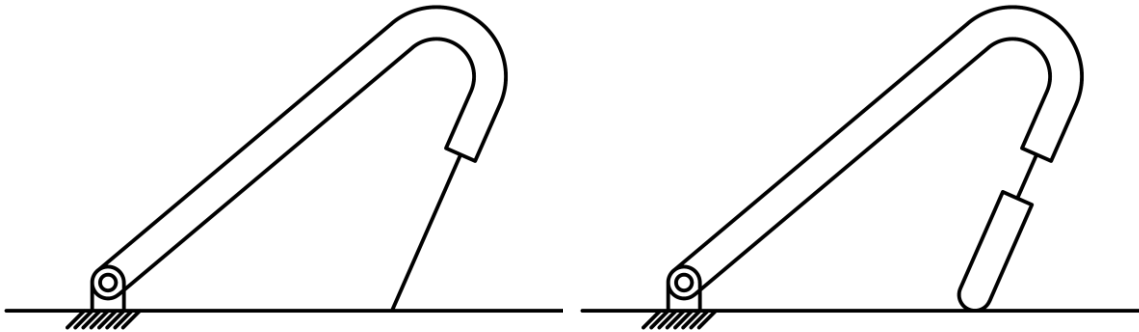
Figure 6.6   Category III – Class 1B
Pin-Joint at Canted Segment Replaced with Discreet Compliance

6.4. DIMENSIONAL SYNTHESIS OF CANTED SPRING

The dimensional synthesis of the canted spring is executed for its pseudo-rigid-body model to determine the geometry that generates a prescribed nonlinear force over its deflection. The principle of Virtual-Work is utilized to determine the force-displacement characteristic behavior of the canted springs. An optimization routine is developed to synthesize the nondimensionalized parameters of the PRBM for producing a more exact constant force over a significant range of their deflection in the case of category III mechanisms.

6.4.1. Pseudo-Rigid-Body Model of Canted Spring. Compliant mechanisms may be best analyzed with a simple yet efficient pseudo-rigid-body model (PRBM) concept. The PRBM of the canted spring, shown in Figure 6.7, is utilized to design and

analyze it for force-displacement characteristics using the equations of the rigid-body slider mechanism. The significance of this PRBM is that one model may be used for all three categories of the canted spring. It has two characteristic pivots with torsional springs to model the compliant beams' resistance to bending. However, the spring constants K_1 or K_2 will be absent (equal to zero) for that category of mechanisms where there is no compliance at that location. The canted spring is loaded vertically at its apex, which is represented by a coupler point (on link 2) in its PRBM.
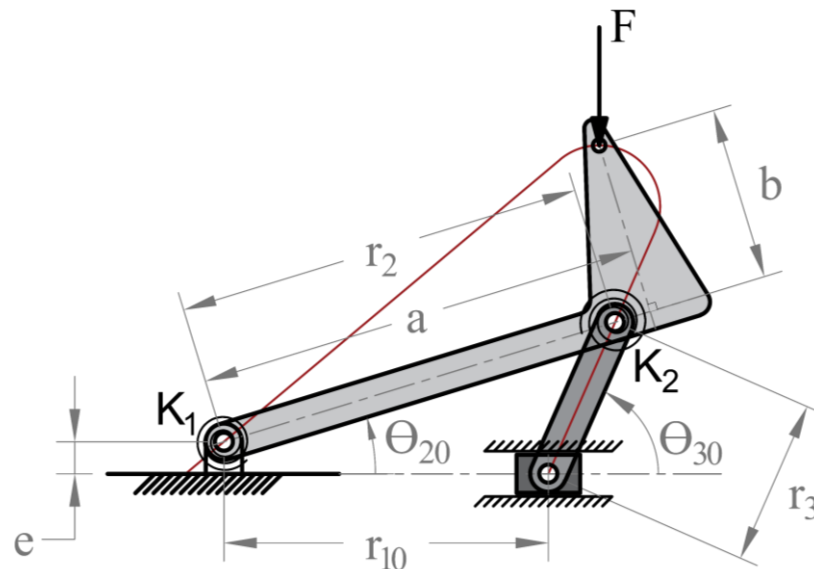
Figure 6.7   Pseudo-Rigid-Body Model of Canted Spring with Force at Coupler Point

6.4.2. Force-Displacement Characteristics of Canted Spring. The force-displacement characteristics of the canted spring are obtained by applying the principle of virtual work [27, 104] on its PRBM, with Δy deflection at the apex as input. It may be defined as for a mechanical system in equilibrium, the net virtual work of all the active forces is zero for all the virtual displacements consistent with the constraints [104]. The

work done by a force on a body along a virtual displacement is known as virtual work. The

method is presented in a series of steps, where the equations are derived in the context of

the PRBM (Figure 6.7) and its vector loops at two different positions, initial and deformed,

as shown in Figure 6.8, for loop-closure equations [105]. The mechanism has a force at its

apex and two torsional springs to represent the beams' compliance at those two locations,

as shown in its PRBM, as illustrated in Figure 6.7.
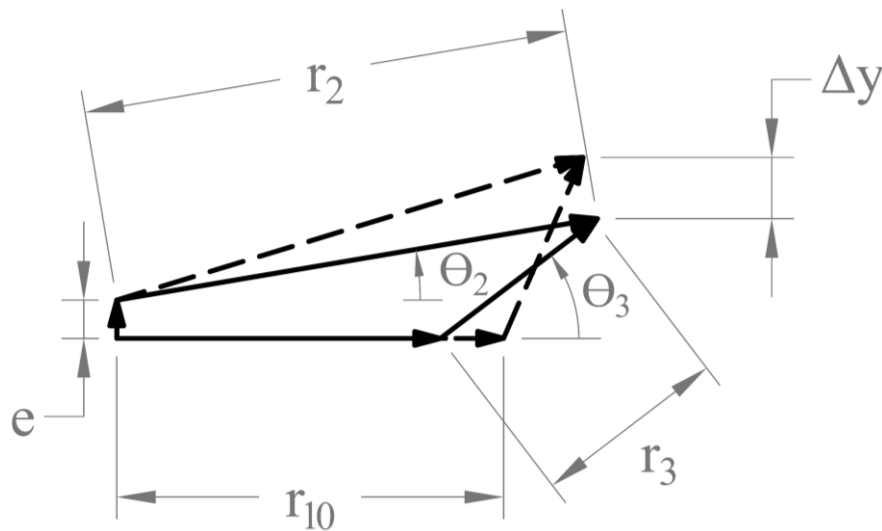
Figure 6.8   Vector Loops of PRBM at Deflected and Undeflected Positions

6.4.2.1. Application of the principle of virtual work. In order to apply the

virtual-work principle, virtual displacements of the mechanism for applied forces and

torques at the springs are determined to evaluate the virtual work done by each of them

from undeflected to the arbitrary deflected position and equated to zero for equilibrium in

the system.

The following sequence of steps describes the procedure in detail to derive the equations for the force.

Step 1: Defining origin and generalized coordinate, q

The ground pivot on the positive-pitch segment is chosen as the origin. For this analysis, angle Θ_2 is a sensible choice as a generalized coordinate, as the force is applied on the input link r_2 (see Figure 6.7).

$$q : \Theta_2 \tag{111}$$

Step 2: Expressing the applied force in the vector form

The input force, F, acting vertically downwards on the spring (Figure 6.7) may be represented in the vector form as,

$$\vec{F} = -\mathrm{F} \cdot \hat{j} \tag{112}$$

Step 3: Determining the position vector of the input force

$$\vec{Z}_F = (\mathrm{a}\cos\Theta_2 - \mathrm{b}\sin\Theta_2) \cdot \hat{\imath} + (\mathrm{a}\sin\Theta_2 + \mathrm{b}\cos\Theta_2) \cdot \hat{\jmath} \tag{113}$$

where, a and b are the dimensions from the origin along the input link to locate the force at the apex, as shown in Figure 6.7.

Step 4: Evaluating virtual displacement for the force

The virtual displacement is derived by differentiating the position vector of the load with the generalized coordinate, q.

Virtual displacement,

$$\delta\vec{Z}_F = \left(\frac{d\vec{Z}_F}{dq}\right)\delta q = \left(\frac{d\vec{Z}_F}{d\Theta_2}\right)\delta\Theta_2 \tag{114}$$

here, Θ_2 is the generalized coordinate

$$\delta\vec{Z}_F = (-\mathrm{a}\sin\Theta_2 - \mathrm{b}\cos\Theta_2)\delta\Theta_2 \cdot \hat{\imath} + (\mathrm{a}\cos\Theta_2 - \mathrm{b}\sin\Theta_2)\delta\Theta_2 \cdot \hat{\jmath} \tag{115}$$

Step 5: Computing virtual work done by the force

It is obtained by carrying out the dot product of the force vector with virtual displacement.

Virtual Work due to the input force,

$$\delta W_F = \vec{F} \cdot \delta \vec{Z}_F = -F(a \cos \Theta_2 - b \sin \Theta_2)\delta\Theta_2 \tag{116}$$

Step 6: Determining angles for torques of the torsional springs at the characteristic pivots

The vector forms of the angles through which the torsional springs react to generate moments are (see Figures 6.7 & 6.8):

For pivot at the positive-pitch segment (K_1),

$$\vec{\Theta}_1 = (\Theta_2 - \Theta_{20}) \cdot \hat{k} \tag{117}$$

For pivot at the negative-pitch segment (K_2),

$$\vec{\Theta}_2 = \{(\Theta_3 - \Theta_2) - (\Theta_{30} - \Theta_{20})\} \cdot \hat{k} \tag{118}$$

Step 7: Calculating torques at the torsional springs and expressing them in vector forms

Torque at torsional spring 1,

$$\vec{T}_1 = -K_1\vec{\Theta}_1 = -K_1(\Theta_2 - \Theta_{20}) \cdot \hat{k} \tag{119}$$

Torque at torsional spring 2,

$$\vec{T}_2 = -K_2\vec{\Theta}_2 = -K_2[(\Theta_3 - \Theta_2) - (\Theta_{30} - \Theta_{20})] \cdot \hat{k} \tag{120}$$

Step 8: Finding virtual angular displacements for the torques

The virtual angular displacements are derived by differentiating the angular vectors with the generalized coordinate, *q*.

$$\delta\vec{\Theta}_1 = \left(\frac{d\vec{\Theta}_1}{dq}\right)\delta q = \frac{d}{d\Theta_2}(\Theta_2 - \Theta_{20})\delta\Theta_2 \cdot \hat{k} = \delta\Theta_2 \cdot \hat{k} \tag{121}$$

$$\delta\vec{\Theta}_2 = \left(\frac{d\vec{\Theta}_2}{dq}\right)\delta q = \frac{d}{d\Theta_2}[(\Theta_3 - \Theta_2) - (\Theta_{30} - \Theta_{20})]\delta\Theta_2 \cdot \hat{k} \tag{122}$$

$$= \left(\frac{d\Theta_3}{d\Theta_2} - 1\right)\delta\Theta_2 \cdot \hat{k}$$

Step 9: Computing the virtual work done at the torsional springs

It is evaluated by the summation of the dot products of the torques with their respective virtual angular displacements.

Virtual work due to the torques,

$$\delta W_T = \vec{T}_1 \cdot \delta\vec{\Theta}_1 + \vec{T}_2 \cdot \delta\vec{\Theta}_2 \tag{123}$$

$$\delta W_T = -K_1(\Theta_2 - \Theta_{20})\delta\Theta_2$$
$$- K_2[(\Theta_3 - \Theta_2) - (\Theta_{30} - \Theta_{20})]\left(\frac{d\Theta_3}{d\Theta_2} - 1\right)\delta\Theta_2 \tag{124}$$

Step 10: Determining the ratio $d\Theta_3 / d\Theta_2$ from the deflected loop

The ratio $d\Theta_3$ / $d\Theta_2$ often referred to as the *kinematic coefficient* of four-bar mechanisms, is derived from the loop closure equation of the deflected position.

$$\vec{e} + \vec{Z}_2 = \vec{Z}_1 + \vec{Z}_3 \tag{125}$$

where, Z_1, Z_2, and Z_3 represent the position vectors of the links r_1, r_2, and r_3, respectively.

that results in *two scalar equations*, as follows:

$$r_2 \cos\Theta_2 = r_1 + r_3 \cos\Theta_3 \tag{126}$$

$$e + r_2 \sin\Theta_2 = r_3 \sin\Theta_3 \tag{127}$$

Differentiating Equation 127 with the generalized coordinate yields,

$$r_2 \cos\Theta_2 \cdot \delta\Theta_2 = r_3 \cos\Theta_3 \cdot \frac{d\Theta_3}{d\Theta_2} \cdot \delta\Theta_2 \tag{128}$$

$$\frac{d\theta_3}{d\theta_2} = \frac{r_2 \cos \theta_2}{r_3 \cos \theta_3} \tag{129}$$

Step 11: Net total virtual work done by the mechanism in equilibrium

According to the principle of virtual work, the net work done by the system in equilibrium is zero, which is as follows:

Net Virtual Work,

$$\delta W = 0 : \ \delta W_F + \delta W_T = 0 \tag{130}$$

results in,

$$F = \frac{-K_1(\theta_2 - \theta_{20}) - K_2[(\theta_3 - \theta_2) - (\theta_{30} - \theta_{20})]\left(\frac{d\theta_3}{d\theta_2} - 1\right)}{(a \cos \theta_2 - b \sin \theta_2)} \tag{131}$$

The *force* equation may be further simplified by substituting the kinematic coefficient,

$$F = \frac{-K_1(\theta_2 - \theta_{20}) - K_2[(\theta_3 - \theta_2) - (\theta_{30} - \theta_{20})]\left(\frac{r_2 \cos \theta_2}{r_3 \cos \theta_3} - 1\right)}{(a \cos \theta_2 - b \sin \theta_2)} \tag{132}$$

6.4.2.2. Nondimensionalized parameters for the mechanism synthesis. The vertical displacement, Δy, from undeflected to deflected position is the input for canted spring analysis. The loop-closure equations yield the following to analyze the PRBM. For the analysis of the mechanism, the input Δy may be expressed as:

$$\Delta y = \ r_2 \sin \theta_{20} - r_2 \sin \theta_2 \tag{133}$$

from the loop closure Equation 127,

$$\theta_3 = \sin^{-1}\left(\frac{e + r_2 \sin \theta_2}{r_3}\right) \tag{134}$$

The mechanism parameters, hereafter, are nondimensionalized to aid the designers in synthesizing a canted spring per the requirements/needs. The dimensional parameters are normalized with the input link length r_2 as follows.

Table 6.6 Nondimensionalized Parameters of the Canted Spring PRBM

$Y = \dfrac{\Delta y}{r_2}$	$E_y = \dfrac{e}{r_2}$
$R = \dfrac{r_3}{r_2}$	$R_1 = \dfrac{r_{10}}{r_2}$
$A = \dfrac{a}{r_2}$	$B = \dfrac{b}{r_2}$

Hence, the loop-closure equations transform to:

$$\theta_2 = \sin^{-1}(\sin\theta_{20} - Y) \tag{135}$$

$$\theta_{30} = \cos^{-1}\left(\frac{\cos\theta_{20} - R_1}{R}\right) \tag{136}$$

$$E_y = R\sin\theta_{30} - \sin\theta_{20} \tag{137}$$

$$\theta_3 = \sin^{-1}\left(\frac{\sin\theta_{20} + E_y}{R}\right) \tag{138}$$

The general equation of force, F, for all three categories of the canted spring is determined using the virtual work principle, which is as follows.

$$F = \frac{K_1(\theta_{20} - \theta_2) + K_2\{(\theta_{30} - \theta_{20}) - (\theta_3 - \theta_2)\}\left(\frac{r_2\cos\theta_2}{r_3\cos\theta_3} - 1\right)}{a\cos\theta_2 - b\sin\theta_2} \tag{139}$$

For category I springs, both the spring constant terms K_1 & K_2 have non-zero values, and for categories II & III, K_2 & K_1 are equal to zero, respectively. Hence, the force equation for the category III mechanisms may be rearranged as follows.

$$F = \frac{K_2}{r_2} \Phi_F \tag{140}$$

where Φ_F is the *nondimensionalized force factor*,

$$\Phi_F = \frac{\{(\Theta_{30} - \Theta_{20}) - (\Theta_3 - \Theta_2)\}\left(\frac{\cos \Theta_2}{R \cos \Theta_3} - 1\right)}{A \cos \Theta_2 - B \sin \Theta_2} \tag{141}$$

As established in sections 4 and 5, category III mechanisms with compliant beams undergoing axial compression loads have the best potential to exert constant force. The configurations of categories I & II behave as soft springs and hard/linear springs, respectively, which can be optimized to exert prescribed nonlinear force profiles.

6.4.3. Optimization For Category III Springs. An optimization routine is developed to synthesize the best possible configurations that produce a more-exact constant force over the desired deflection. The normalized (nondimensionalized) parameters of the PRBM that result in CFM are determined by minimizing the variation in the output force over a significant range of its deflection. The dimensions and initial angles of the PRBM are computed from these optimized parameters to construct a constant-force canted spring, as explained in the later springs. The optimization problem may be stated as follows:

$$find\ X \ = \ \begin{Bmatrix} R \\ A,\ B \\ E_y \\ \Theta_{20} \\ \Theta_{30} \end{Bmatrix} \tag{142}$$

which minimizes the function, i.e., also termed as *Constancy Ratio, α*

$$f(X) = \frac{|F|_{max}}{|F|_{min}} = \frac{|\Phi_F|_{max}}{|\Phi_F|_{min}} = \alpha \tag{143}$$

subject to the following constraints

$$R, A > 0 \qquad B > 0.15R \qquad R_1 > 0.1$$

$$\pi/3 \ \le \ \theta_{30} \ \le \ \pi/2$$

Constancy ratio may be defined as a ratio of the maximum value of the force or nondimensionalized force factor to its minimum value. The closer the ratio to unity, the constant the output force remains with respect to its deflection
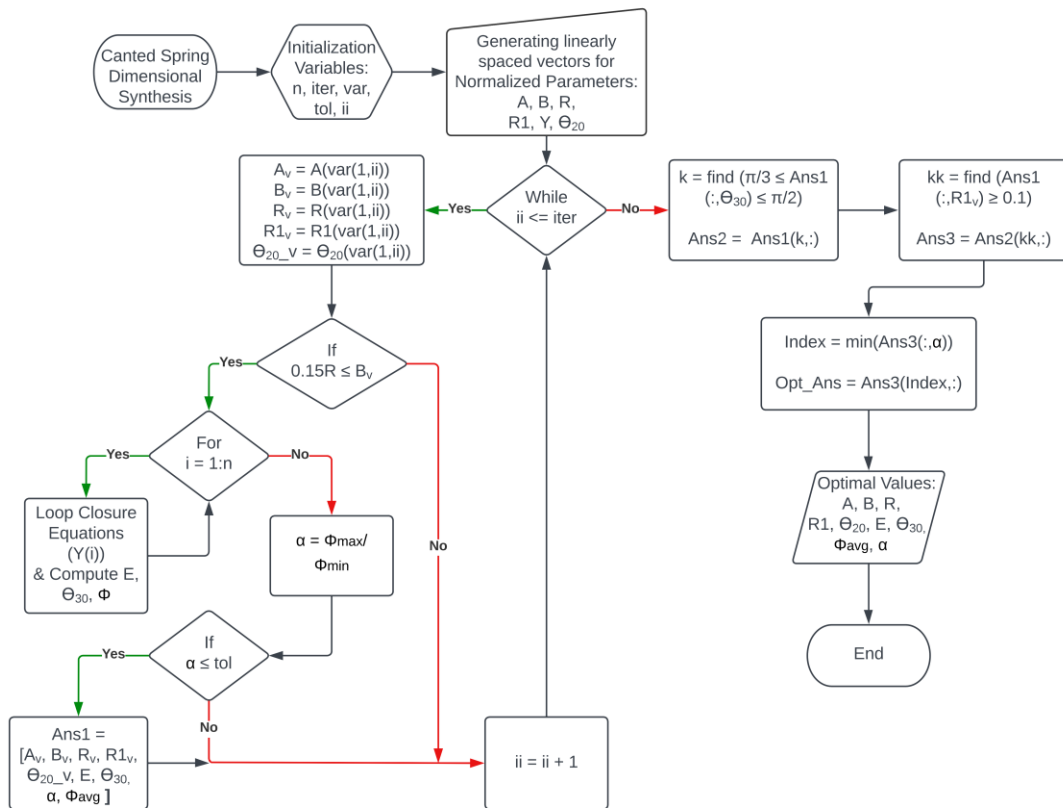
Figure 6.9   Flowchart of the Optimization Synthesis for Category III Springs

A flowchart, presented in Figure 6.9, explains the sequence of operations of the optimization routine that determines the best possible combination of parameters of the PRBM for a CFM for given constraints. An additional set of constraints are applied to determine other configurations of CFM with slightly different objectives, as stated below. *Additional constraints* for the optimization routine in the flowchart:

a) Find a solution for maximum Φ_{avg} from 'Ans3' - this determines a configuration with a higher amplitude of nondimensionalized force factor. This configuration helps in developing CFMs with higher force amplitude in a compact form without compromising on the constancy of the force (α)

b) Find solutions for various Φ_{Favg} and E_y from 'Ans3' with low α values - this helps in determining configurations with different offset values (eccentricity, E_y) for the ground pin-joint, giving the designer(s) the flexibility in developing a CFM that suits their shape and size constraints.

This flowchart lays out the general sequence of computations but does not show all the programming details, which are exhibited in Appendix A.

The dimensional synthesis results of the pseudo-rigid-body model for category III springs are tabulated for positive, zero, and negative eccentricities of ground pin-joint, E_y, that generate constant force in Tables 6.7, 6.8, and 6.9, respectively. The nondimensionalized force factor, Φ_F, is practically constant across its substantial deflection. Each of the optimized configurations in the tables has the average value of Φ_F, which helps determine the expected nominal output constant force using Equation 144.

$$F_{avg} = \frac{K_2}{r_2} \Phi_{F_{avg}} \tag{144}$$

Table 6.7 lists the PRBM configurations of the canted springs with a *positive offset/eccentricity* for the ground pin joint at the positive-pitch segments (link 2), i.e., the pin joint is above the ground level (slider level). Each configuration offers a different average value of Φ_{Favg} and eccentricity, E_y. It may also be noted that some of them provide large, recommended deflection ranges with their corresponding constancy ratios.

Table 6.7 Dimensional Synthesis Results for E-Positive Configurations.

E+	Config. 1	Config. 2	Config. 3	Config. 4	Config. 5
E_y	0.185	0.085	0.144	0.02	0.145
R	0.544	0.544	0.59	0.60	0.60
θ_{20}	20°	25°	24.5°	32°	25°
θ_{30}	75.6°	68.9°	71.25°	66.4°	71.1°
A	1.00	0.90	0.97	0.90	1.25
B	0.15	0.50	0.16	0.45	0.17
Y	$0.075 - 0.3$	$0.1 - 0.375$	$0.1 - 0.35$	$0.1 - 0.4$	$0.1 - 0.35$
α	1.0542	1.0364	1.0311	1.0402	1.0320
$\lvert \Phi_F \rvert_{avg}$	0.6171	0.5894	0.4451	0.4126	0.3265

The force-displacement characteristic behavior of these configurations is demonstrated with their nondimensionalized parameters in plots of Figure. 6.10.
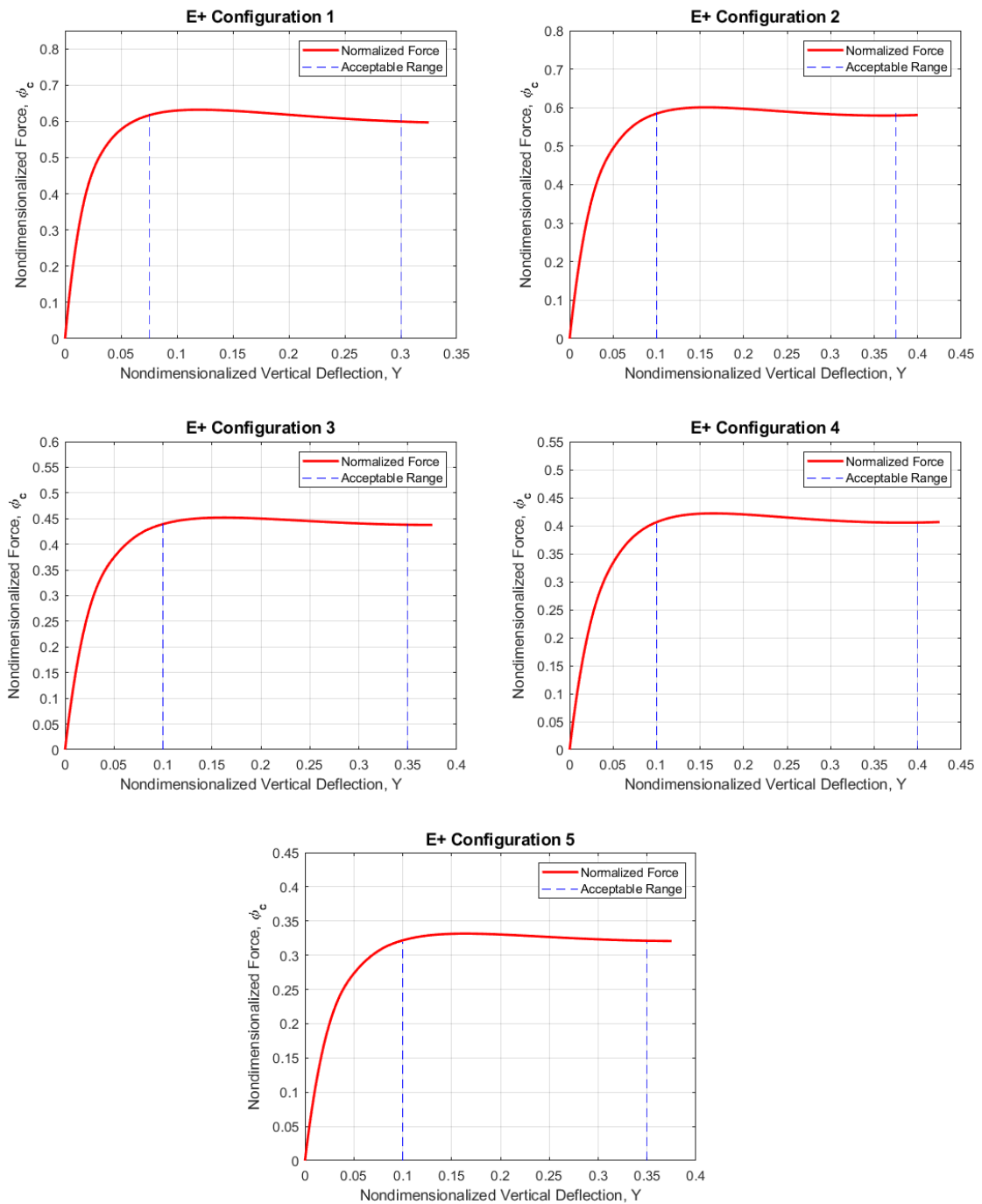
Figure 6.10   Force-Deflection Characteristics of Canted Spring E+ Configurations

Similarly, the optimized configurations for *zero offset/eccentricity* of the ground pin joint, i.e., it is at the level of the slider, are tabulated in Table 6.8. Their force-deflection characteristics are demonstrated in Figure 6.11.

Table 6.8 Dimensional Synthesis Results For E-Zero Configurations.

E0	Config. 1	Config. 2	Config. 3	Config. 4	Config. 5
E_y	0	0	0	0	0
R	0.531	0.552	0.568	0.60	0.60
θ_{20}	30.5°	31.5°	31.5°	35°	34°
θ_{30}	72.9°	71.2°	66.9°	72.9°	68.75°
A	0.90	0.90	0.90	1.00	1.10
B	0.38	0.37	0.50	0.15	0.40
Y	0.075 – 0.35	0.075 – 0.35	0.1 - 0.4	0.075 – 0.35	0.1 - 0.4
α	1.0576	1.0474	1.032	1.0544	1.0385
$\|\Phi_F\|_{avg}$	0.70	0.5969	0.5011	0.4136	0.349

Again, Table 6.9 has the optimized configurations of the PRBM with a *negative offset/eccentricity* of the ground pin joint, i.e., below the level of the slider. Their force-displacement characteristic behavior is presented in Figure 6.12.
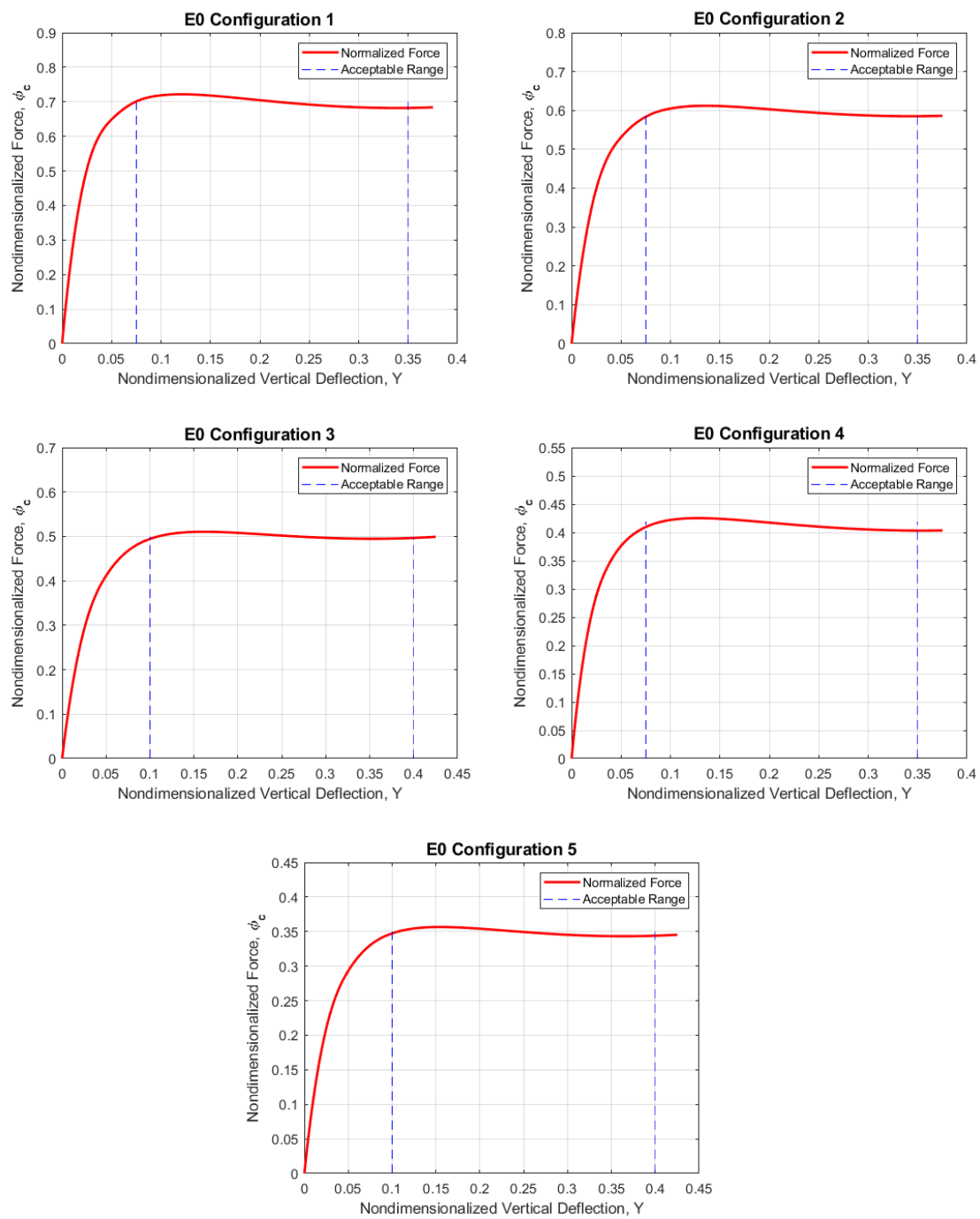
Figure 6.11 Force-Deflection Characteristics of Canted Spring E0 Configurations

Table 6.9 Dimensional Synthesis Results For E-Negative Configurations.

E-	Config 1	Config. 2	Config. 3	Config. 4	Config. 5
E_y	-0.059	-0.075	-0.09	-0.017	-0.195
R	0.40	0.414	0.441	0.477	0.507
θ_{20}	26.67°	29°	31.5°	29°	43.5°
θ_{30}	77.1°	81.8°	78.7°	78.7°	76.67°
A	0.90	0.98	1.25	1.15	1.05
B	0.50	0.20	0.34	0.16	0.15
Y	0.05 – 0.3	0.05 – 0.325	0.05 – 0.325	0.05 – 0.35	0.05 – 0.25
α	1.0393	1.0491	1.033	1.0349	1.0387
$|\Phi_F|_{avg}$	1.502	1.3247	0.8587	0.7641	0.6287

These optimized configurations of the PRBM of the category III spring provide the designer with options to meet their requirements and needs depending on their constraints like materials, shape, size, and level of constancy of the force, etc.

The following section illustrates the design and construction of a constant-force canted spring for the requirements of a designer/user from the tabulated configurations with a step-by-step process.
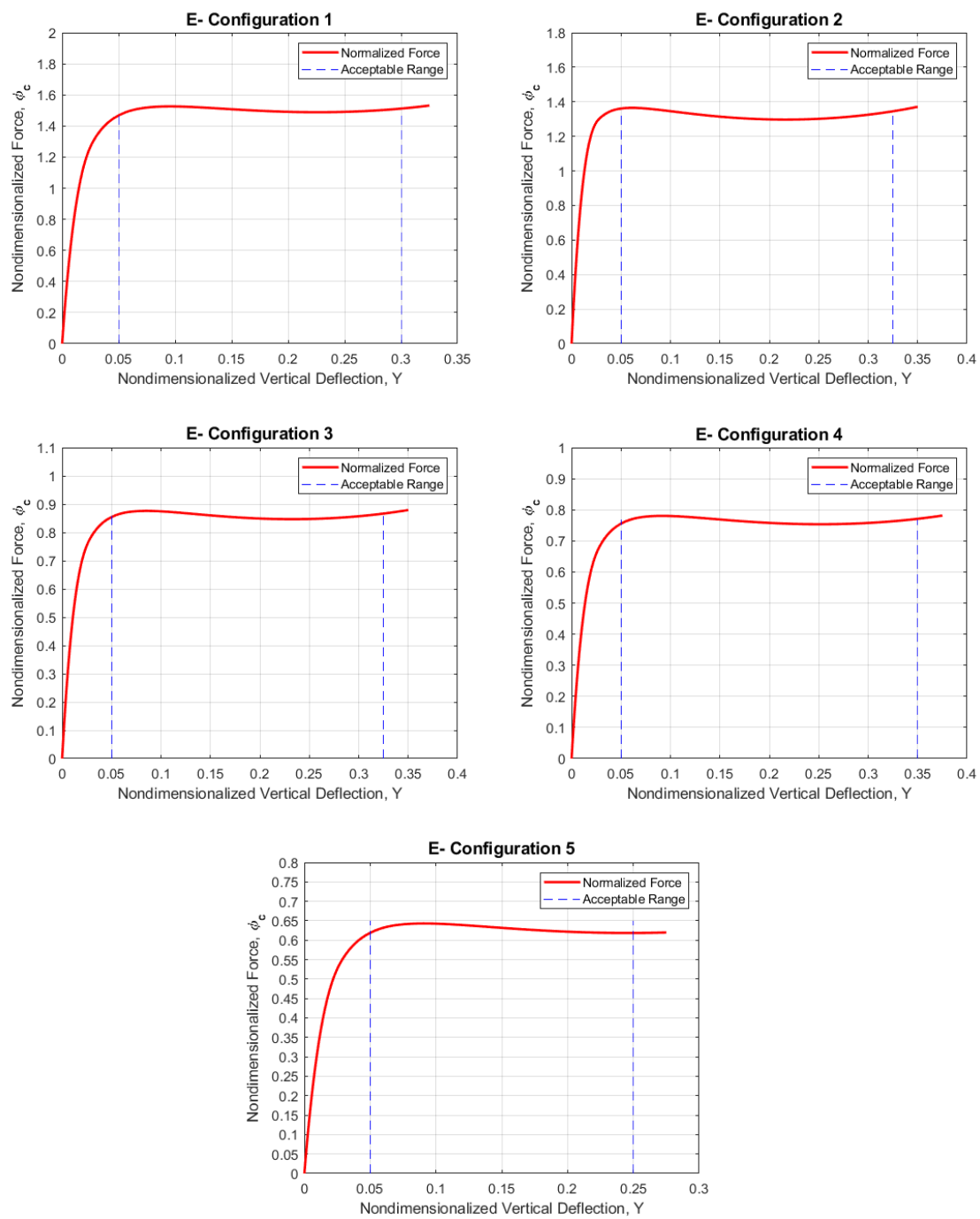
Figure 6.12   Force-Deflection Characteristics of Canted Spring E- Configurations

6.5. CONSTRUCTION OF DESIRED CONSTANT-FORCE CANTED SPRING WITH EXAMPLE

A methodology is formulated to aid the user in generating a constant-force canted spring using the optimized tables per their needs. The designer has a choice for the eccentricity of the ground pin joint either above, at, or below the ground level (slider) while developing a canted spring for one's prerequisites. A mechanism is developed as an example using an E-positive configuration to demonstrate the process of designing a canted spring for given design requirements. The method uses a similar design philosophy and draws inspiration from the approach developed by Bapat et al. [106].
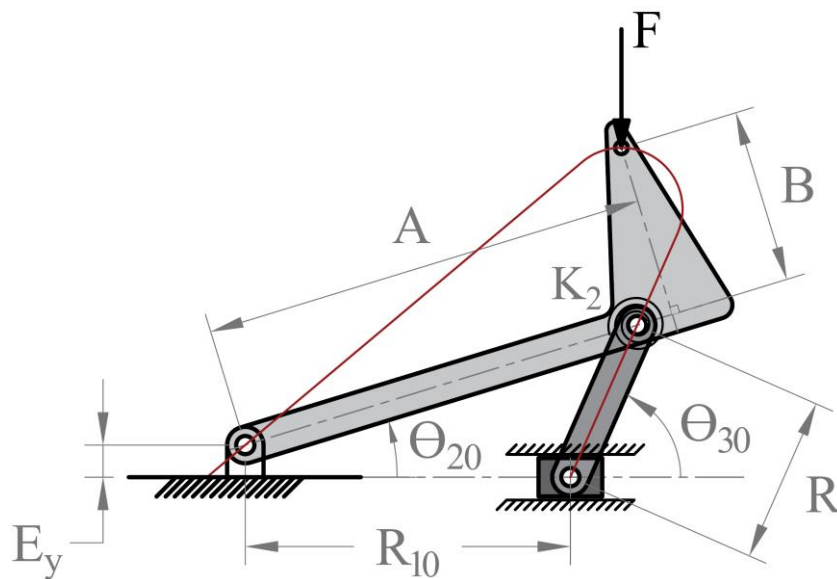
Figure 6.13   Pseudo-Rigid-Body Model of Canted Spring with Normalized Parameters

6.5.1. Design Methodology - Steps. The methodology of generating a desired constant-force canted spring is described in a series of steps. The steps are provided in the context of the pseudo-rigid-body model of the category III canted spring ($K_1 = 0$), as shown

in Figure 6.13. For this demonstration, E-positive configuration 3 from Table 6.7 is considered for the desired CFM construction.

- User Requirements

   The user has to provide the following three desired conditions for generating a CFM

   i. $Desired\ Height\ of\ Spring,\ T_y = 3.8\ in$

   ii. $Nominal\ Force,\ F = 5\ lb$

   iii. $Material\ of\ the\ Spring:\ 1075\ Spring\ Steel$

   $Young's\ Modulus,\ E = 30e^6\ psi$

- Step 1: Determine the link length r_2

   From the PRBM,

   $Nondimensionalized\ Height\ of\ the\ Spring,$

   $$H = E_y + A\sin\Theta_{20} + B\cos\Theta_{20}$$

   hence,

   $$\frac{T_y}{r_2} = E_y + A\sin\Theta_{20} + B\cos\Theta_{20}$$

   $$\Rightarrow r_2 \approx 5.5\ in$$

- Step 2: Determine the dimensions and angles of the PRBM from the nondimensionalized parameters and r_2

   $$r_3 = R \cdot r_2 \approx 3.25\ in$$

   $$e = E_y \cdot r_2 \approx 0.8\ in$$

   $$a = A \cdot r_2 \approx 5.34\ in$$

   $$b = B \cdot r_2 \approx 0.88\ in$$

$$\Theta_{30} = \sin^{-1}\left(\frac{e + r_2 \sin \Theta_{20}}{r_3}\right)$$

$$r_{10} = r_2 \cos \Theta_{20} - r_3 \cos \Theta_{30}$$

$$compliant\ segment\ length,\ L = {r_3}/{\gamma} \approx 3.8\ in$$

where, $characteristic\ radius\ factor,\ \gamma = 0.85$

Ensure that the computed Θ_{30} value is nearly the same as the optimized value provided in the table.

- Step 3: Calculate the required torsional spring constant K_2 and determine the cross-section of the beam

$$Given\ Force, F = \frac{K_2}{r_2}\phi_{c\,avg} = 5\ lb$$

$$\Rightarrow K_2 = 61.78\ in \cdot lb$$

Choose an appropriate or available thickness for the beam, and compute its width from K_2

    Free choice, $t = 0.04\ in$

    here, $K_2 = \gamma K_\Theta \frac{EI}{L}$

    where, $stiffness\ coefficient,\ K_\Theta = 2.65$

$$\Rightarrow width,\ w = \frac{12 \cdot I}{t^3} \approx 0.65\ in$$

- Step 4: Compute the force-deflection characteristics

Since the width of the beam may be rounded to the nearest second decimal, the spring constant K_2 will be slightly different from the initially calculated value, as the area moment of inertia (I) is calibrated.

$$Beam's\ torsional\ resistance, K_{2\_f} = \ \gamma K_\Theta \frac{EI_{calibrated}}{L}$$

Compute the force-displacement profile using Equations 140 & 141, as follows.

$$F = \frac{K_{2\_f}}{r_2} \Phi_F$$

6.5.2. PRBM of the Desired Canted Spring. The PRBM mechanism of the desired canted spring is modeled with the computed parameters:

i. Locate the ground pivot with the 'e' value above/below the slider level, as shown in Figure 6.14

ii. Link r_2 can be identified with its length and initial angle, Θ_{20}, as depicted in Figure 6.14

iii. Figure 6.14 also exhibits an imaginary circle that the link r_3 would trace when it is not fully constrained to identify the slider location. Please note that only one of the two locations will make it a canted spring (i.e., negative-pitch segment)

iv. Locate the apex point with its relative coordinates, a & b, which marks the completion of PRBM construction. The apex point is one of the crucial parameters for the generation of constant force throughout its recommended deflection range

v. Calculate the length of the compliant segment and trace it along r_3, as illustrated in Figure 6.14

6.5.3. Topology Construction. The topology construction of the canted spring is based on the PRBM and its apex point. Recommendations are provided below for the topological shape connecting the negative-pitch segment with the apex and ground pivot with steps and a sketch in Figure 6.14, but it is the designer's prerogative to shape the canted spring to desire.
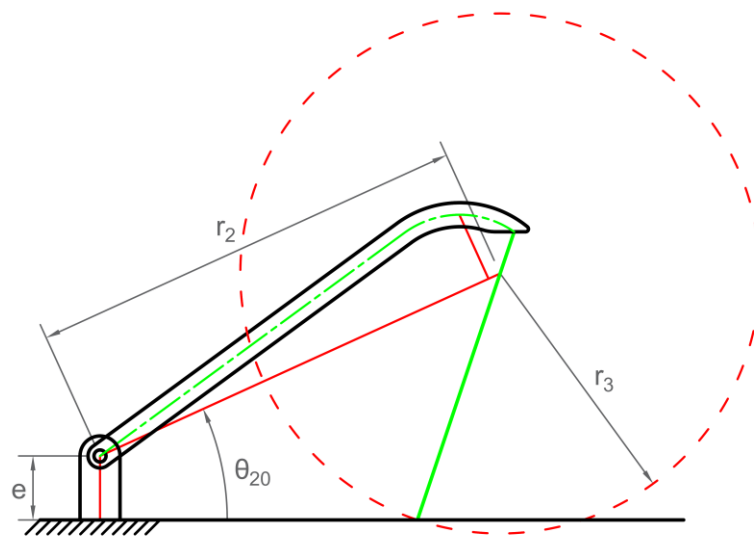
Figure 6.14   Topology Construction of The Canted Spring – Example

- Step i: Draw a construction line either perpendicular to the negative-pitch segment or a horizontal line to the width of the rigid segment

- Step ii: Now, create a circle with the apex point as one end of the diameter and as big as it gets closer to the end of the compliant segment

- Step iii: Now, draw a tangential line to the circle, completing the path of the rigid segment from the ground pin joint to the apex and the compliant beam end

- Step iv: Delete the unwanted curves and generate the thickness of the rigid segment, which is enclosed with the line drawn in *step i*

6.5.4. Validation of Force-Displacement Behavior of Canted Spring. The behavior of the example mechanism of the canted spring discussed in section 6.5.3 is examined with finite element analysis (FEA) simulations, and its undeflected position is presented in Figure 6.15.
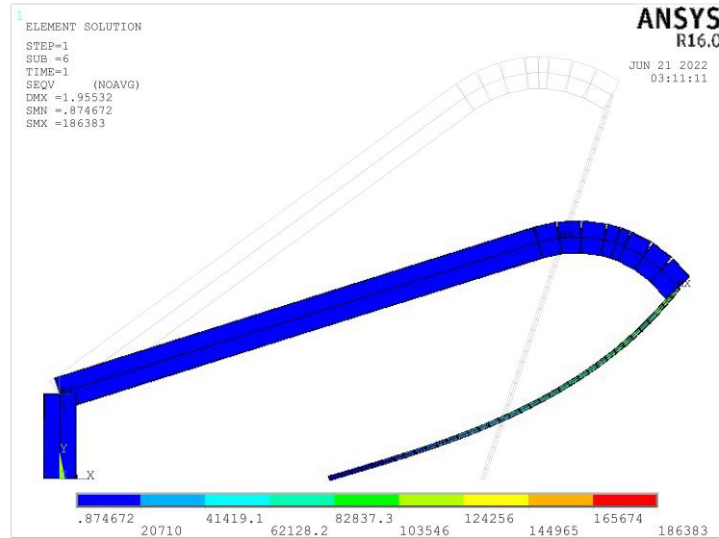
Figure 6.15 Deflected and Undeflected Positions of
Canted Spring – FEA (Ansys®) Simulation

The force profile predicted by the PRBM-based model is validated with FEA simulations using ANSYS® Mechanical APDL v16, as shown in Figure 6.16. The nominal force of the spring is computed as:

$$F_{avg} = \frac{K_2}{r_2} \Phi_{F_{avg}} \tag{145}$$

It may be noted that the force profiles nearly match each other, thus validating the model for the generation of constant force by canted springs, with a factor of safety of 1.12 for such large deflections. The minute variance between the FEA values and the PRBM results is likely due to i) computational assumptions of the software, esp. for beams under near buckling, ii) assuming the generalized average values for PRBM parametric functions, such as γ and K_{Θ}. More accurate values may be computed for each specific case by the equations provided by Midha, Howell, and Norton [67-71].
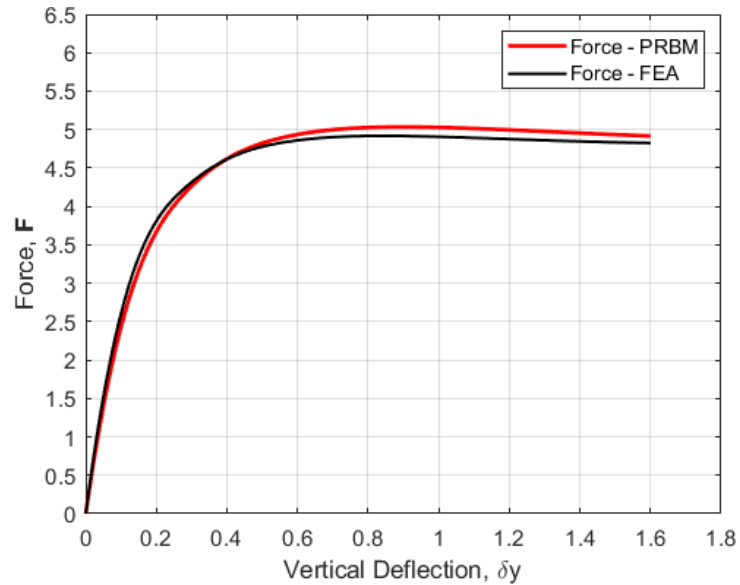
Figure 6.16   Force-Characteristic Behavior of the Canted Spring Example
– PRBM & FEA

6.6. CATEGORY I AND CATEGORY II SPRINGS

The compliant mechanisms of categories I and II behave as soft springs and hard/linear springs, respectively, which may be optimized to exert prescribed nonlinear force profiles. The category I canted springs have the potential to exert near-constant force over a selected range of its motion. The force-displacement characteristics of that spring might not be as constant or for such a large deflection as category III springs.

The force-displacement behavior of the category I & II springs is validated with FEA, as shown in Figures 6.17 and 6.18.

6.7. SUMMARY

A unique compliant mechanism, Canted Spring, has been examined to determine all possible configurations. A formal type synthesis that is based on the rigid-body-replacement method is employed to enumerate all the possible configurations. Pseudo-

rigid-body kinematic chain of the canted spring is determined by studying its behavior under loads using chain algorithm and FEA simulations. The kinematic chain and its PRBM are utilized in the type synthesis methodology to ensure there is no isomorphism. Eight configurations are derived, and they are classified into three categories based on the location of the compliance.
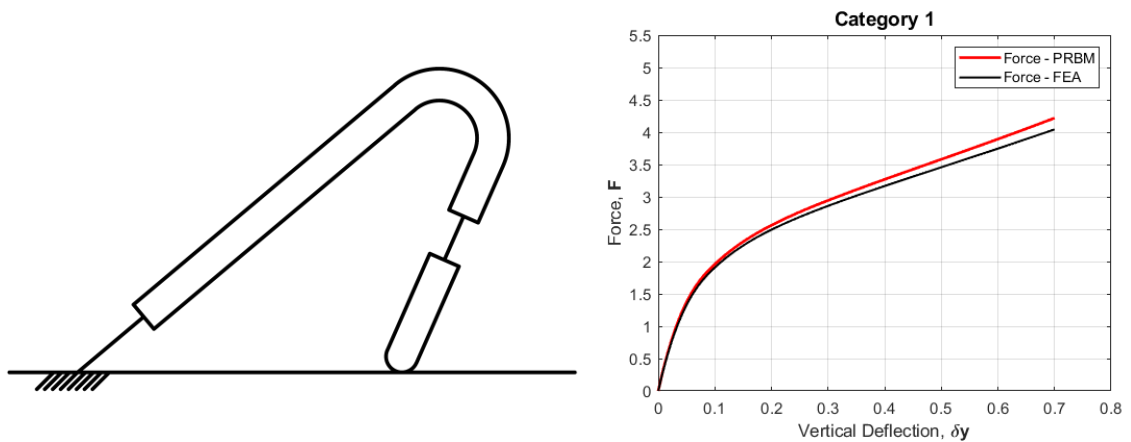
Figure 6.17   Force-Characteristic Behavior of Category I Canted Spring
with Two SLFPS – PRBM & FEA

The Principle of Virtual Work is used to determine the force-displacement equation for all three categories of the canted spring. Dimensional synthesis is conducted for Category III springs as they have the best potential for generating constant force since the compliant segments of these springs can be loaded axially. A synthesis routine is developed to optimize its PRBM parameters such that the output force remains nearly constant through a significant range of its deflection. The parameters are normalized so that the mechanism can be built to scale and magnitude of force per user requirements. A design methodology is presented for constructing a constant-force canted spring for given

requirements, from PRBM to its topology as well. The results are validated with finite element analysis simulations. The general force-displacement behavior of the other two category springs is also studied.
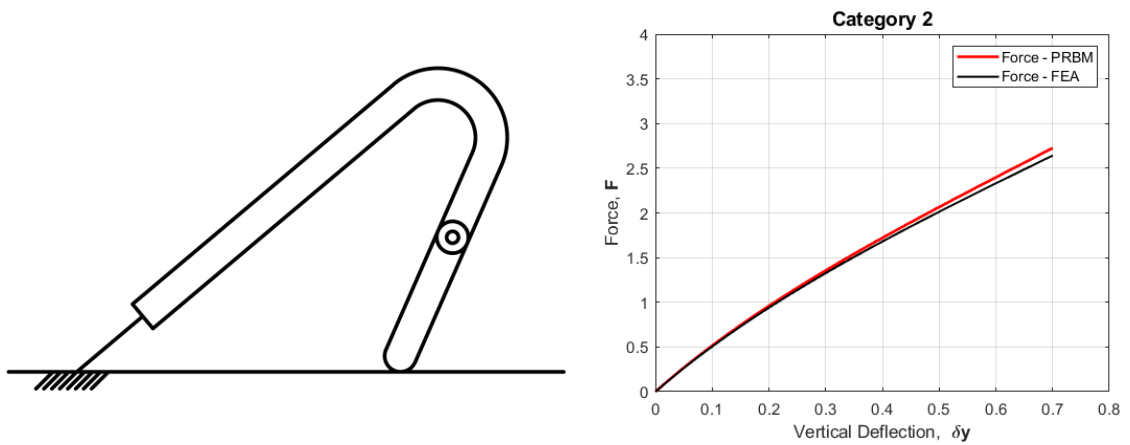
Figure 6.18   Force-Characteristic Behavior of Category II Canted Spring
with SLFP – PRBM & FEA

7. CFM SYSTEMS FOR HIGH LOAD-BEARING AND UNIFORM PRESSURE DISTRIBUTION APPLICATIONS: MODULAR UNITS AND ARRAY STRUCTURES

7.1. INTRODUCTION

Constant-force mechanisms have a wide range of applications, as they can exert and maintain the force/load nearly constant irrespective of their deformation. There have been many efforts in developing such mechanisms to meet specific demands and needs, e.g., Robotic end-effectors, CFM exercise equipment, electric connectors, etc. Hence, the mechanisms' parameters, i.e., kinematic, material, and topology, were optimized for such applications to operate under the stress limit for desired life cycles. Often, there is a need for implementing multiple CFMs to meet the force requirements and abide by the stress limits.

This section proposes a few generic arrangements of CFMs to serve such various load-bearing applications. Hereafter, they are characterized as CFM Systems: i) Modular Units and ii) Array Structures. A modular unit consists of two or more constant-force elements (segments/mechanisms) to provide higher load capacity while maintaining stresses under yield limit for given space constraints. An array structure is an arrangement of CFMs or modular units in systematic rectangular or circular configurations for uniform load distribution applications. The potential applications for each CFM system are discussed in the following sections, along with its design development.

7.2. MODULAR UNITS

A module (or modular unit) of multiple compliant constant-force elements (segments or mechanisms) provides higher-load bearing capacity for the desired deflection

while maintaining each segment/mechanism under the stress limit. The constant-force elements are arranged symmetrically such that the transverse reaction forces are balanced out, which enables the modules to exert load and translate in only one desired direction. The CFM elements can either be oriented radially or evenly spaced about the midplane(s) of the modular units. They could also have guide rods to ensure a smooth and directed translation of the top plate where and when needed, and in other cases, there is no need for them, as depicted in Figure 7.1. The units may be pre-assembled for given load requirements and design constraints of the application and deployed accordingly, e.g., aircraft landing gear, car suspensions, etc. The nominal constant force of the module may be adjusted as needed by adding or removing the CFM elements.

a.   b.

Figure 7.1   A Constant-Force Modular Units:
a.) Four Compliant Pinned-Pinned Segments, b.) Eight Canted Springs

One of the prime applications identified for the best use of constant-force modules is in the bridge/structure design [107]. Solving and accounting for the indeterminacy of a structure is a major part of the traditional design of a bridge/structure with many support

columns. Incorporating specifically-designed CFM modular units at a few selective columns of a bridge/structure would provide a known reaction force at each of those columns, irrespective of their location and irregularities in the column height. This arrangement of a bridge/structure with CFM modules would eliminate or at least drastically minimize the indeterminacy in its design, as demonstrated in Figure 7.2. It might also facilitate the efficient and economical construction of such structures. This research work is further investigated by Miyamoto and Midha [108].

Constant-Force
Support
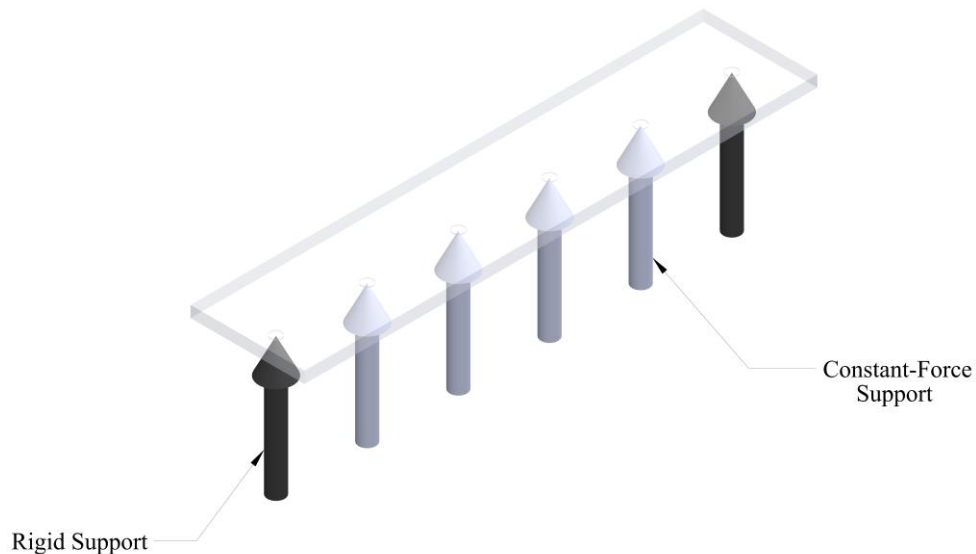
Rigid Support

Figure 7.2   A Bridge/Structure Supported by Rigid and Constant-Force Supports

The Static equilibrium of the bridge/structure with constant-force modular units under uniformly-distributed load, as shown in Figure 7.3, may be expressed as follows,

$$\sum F_y = 0: \ W = \sum_{i=0}^{2} R_i + 4C \qquad (146)$$
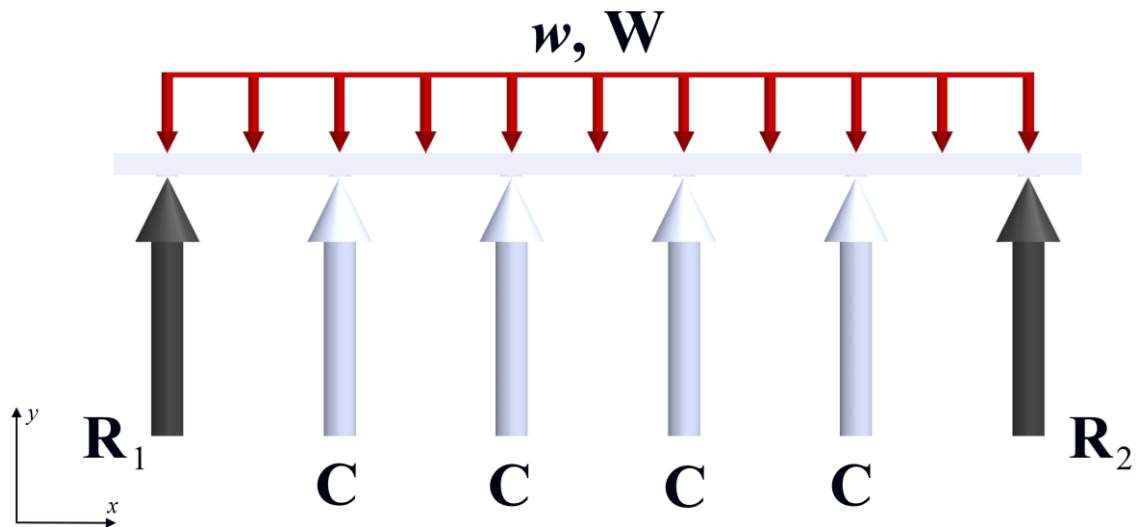
Figure 7.3   A Bridge/Structure with Modular Units under UDL

7.3. ARRAY STRUCTURES

A constant-force array structure has CFM elements or modular units arranged systematically in a rectangular or circular orientation for uniform pressure distribution. They also provide very high load-bearing capacity as they can be assembled with as many CFM units as needed, as shown in Figure 7.4. They have the ability to distribute the load uniformly regardless of the shape and size of the object resting on the array, as all of its units exert the same constant reaction force irrespective of their deflection.

The array structures may find applications in various products like automotive seating, chair cushions, shoe soles, bedding, and other similar products in medical & consumer markets for better pressure distribution. A simple algorithm is created to help synthesize suitable array structures based on the desired requirements, such as maximum allowable deflection, the curvature of the object resting on it, total load capacity, size, etc.
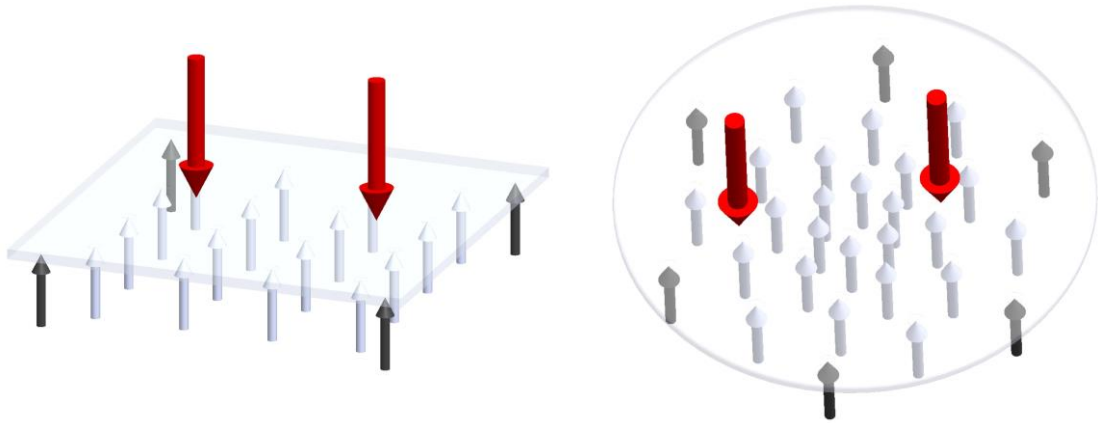
Figure 7.4   Constant-Force Array Structures: Rectangular and Circular Orientations

7.3.1. Automotive Seating – Application Example.   Automotive seat cushions shown in Figure 7.5 are considered for this example to demonstrate the behavior of an array structure, especially when a person is seated in a skewed position.   The pressure distribution of a person sitting upright on the cushion with a backrest in automotive seating is determined experimentally and through FEA simulations by Grujicic et al. [109] and Siefert et al. [110], as shown in Figures 7.5 a and b, respectively.   The weight distribution and the contact surface area vary if a person is sitting in a skewed position, i.e., cross-legged or leaning to one side.   It may be noted that the person experiences a non-uniform pressure distribution on one's glutes, both in nominal and lopsided seating, with a few high-pressure points causing moderate to extreme discomfort depending on the duration of seating and cushion materials.

a.   b.
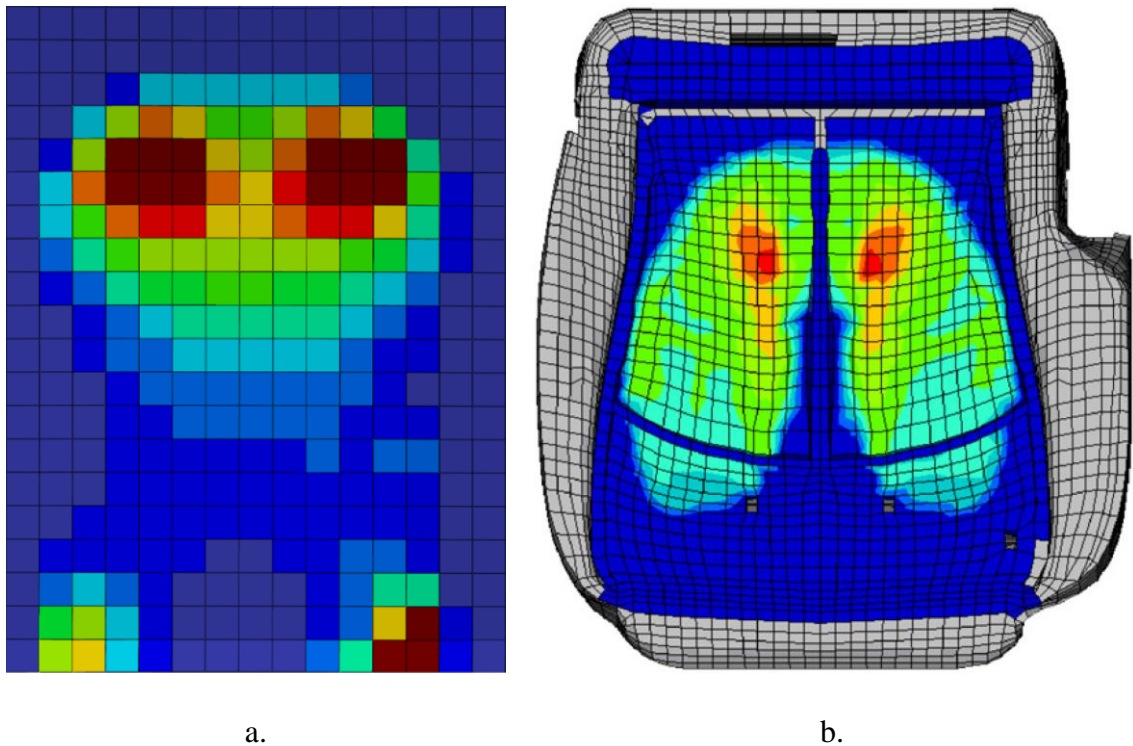
Figure 7.5   Pressure Distribution on Automotive Seating in Upright Position with
Backrest [109, 110]: a.) Experimental Data, b.) FEA Simulations

An automotive seat design with an array structure would alleviate such issues to provide better comfort to drivers and passengers. The reaction force of the elements in the array that are in contact with the body remains nearly the same regardless of their location & deflection, leading to uniform pressure distribution for different-sized humans, even in skewed positions.

7.3.2. Design Methodology. The process of developing on CFM array structure (rectangular orientation) is demonstrated below for the automotive seating example.

- Design Requirements for Array Construction

    1. Weight of the Person/Object (input), $W = 200\ lb$

    2. Curvatures (k) or radii of the object (r), $r = 3\ \&\ 2\ in$

3. Approx. size of the array (seat) (length x width): $12 \times 6 \, in$

4. Max. allowable deflection, $\delta = 1 \, in$
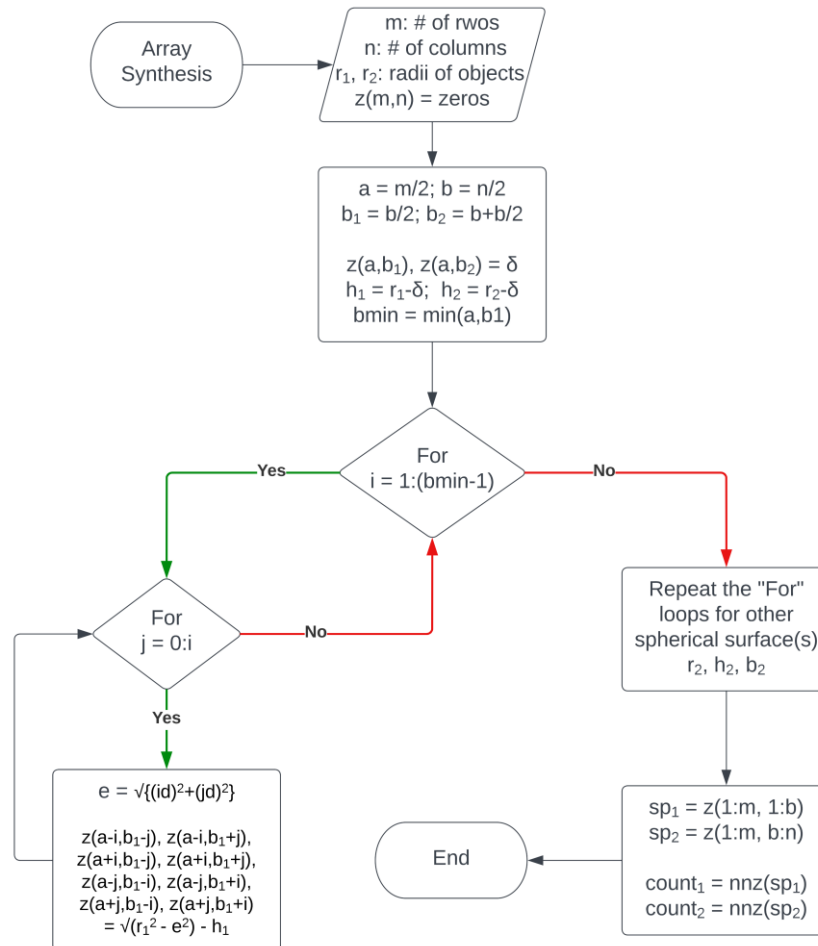
Figure 7.6 Algorithm to Generate Rectangular Array Structure

- Computation

  1. Distance between elements: $d = 0.1 \cdot (width - 1)$

  2. Calculate the number of elements in contact and their deflections using the devised program as demonstrated with a Flowchart in Figure 7.6. The

results obtained for this example from the MATLAB program are:

$$Number\ of\ units\ for\ sphere\ 1:\ \ 61$$

$$Number\ of\ units\ for\ sphere\ 2:\ \ 37$$

3. Compute the constant reaction force needed at each element of the array

$$Total\ number\ of\ elements\ in\ contact,\ \ n = 98$$

$$Force\ at\ each\ element,\ \ F = W/n\ \cong 2\ lb$$

4. The residual forces are accommodated by the ground reactions through the substrate, $W - F \cdot n = 4\ lb$

a.

b.
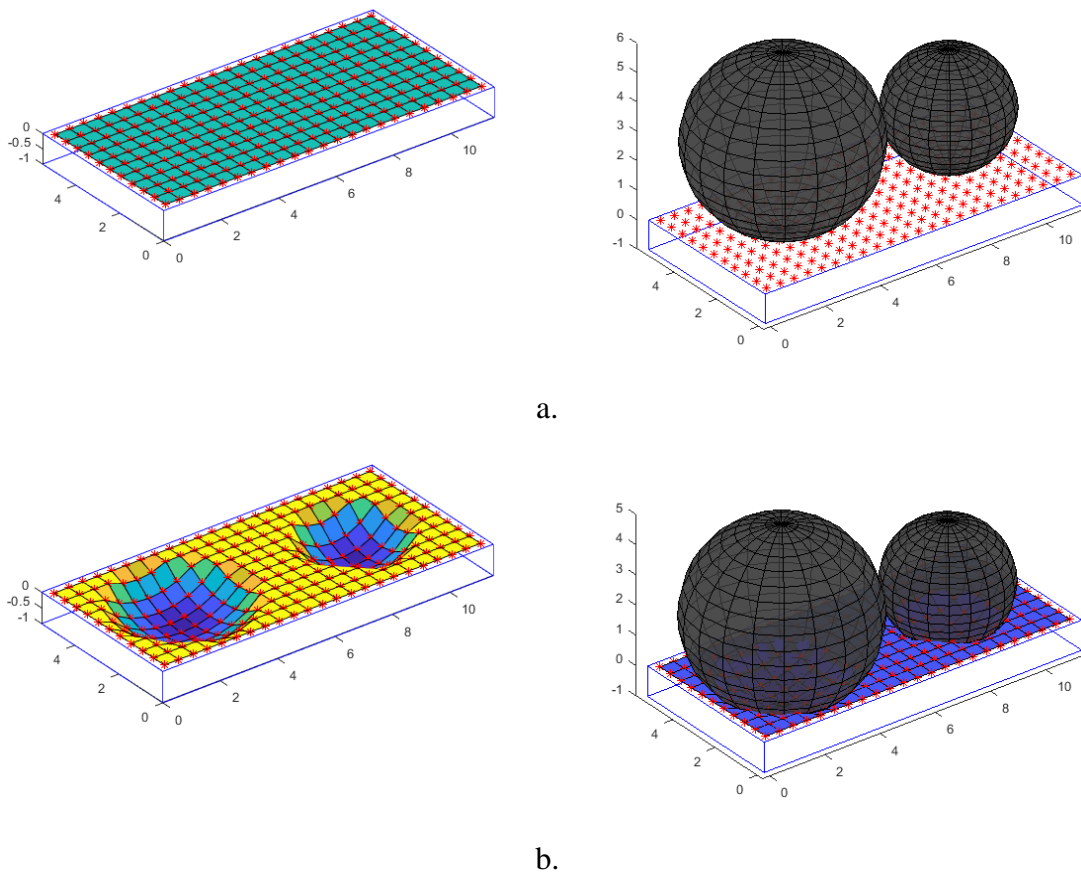
Figure 7.7   Array Structure Behavior in a Skewed Seating for the Cushion Example
a.) Initial Position, b.) Descended Position
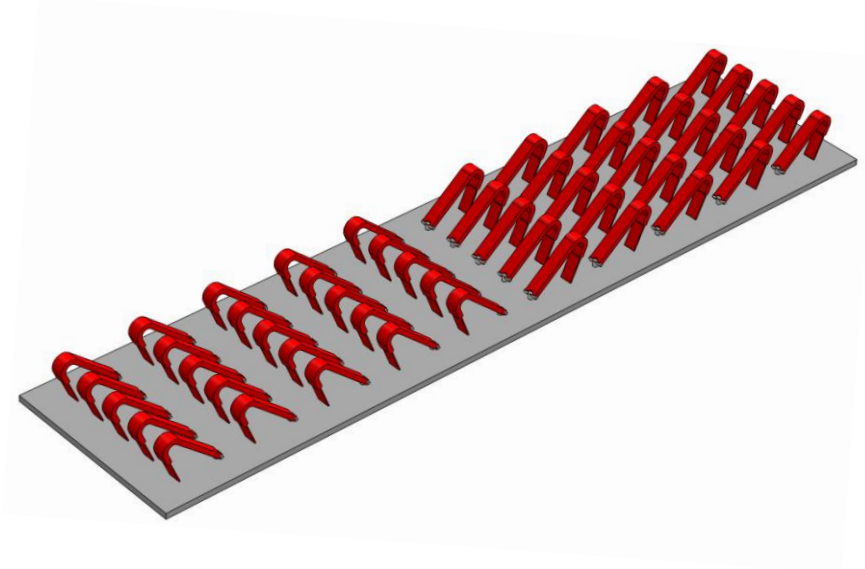
Figure 7.8   Algorithm to Generate Rectangular Array Structure

An automotive seat with a rectangular array structure (23 X 11) is designed to bear 200 lb human resting on it, with 196 lb. provided by the CFM elements of the array, and four pounds is from the ground reaction force.   The resulting seat cushion for the automotive seating is presented in Figure 7.7, demonstrating its behavior under loads. Figure 7.8 illustrates a possible arrangement of the seat cushion array.

7.4. SUMMARY

Constant-force modular units and array structures are developed to serve the needs of high-load-bearing applications. Arrays structures also have the ability for uniform pressure distribution, as the load across its elements remains nearly constant irrespective of their deflections. A few examples were presented to demonstrate the functionality of these CFM systems.

8. CONCLUSION AND FUTURE WORK RECOMMENDATIONS

8.1. SUMMARY OF THE RESEARCH INVESTIGATION

The theory that simple, compliant segments with different boundary conditions, subjected to axial loading, exert near-constant force the need for design optimization was demonstrated for various segment types. The pseudo-rigid-body model (PRBM) concept was utilized to predict the force-displacement characteristics of the beams under axial loading. The characteristic load for each beam was evaluated at zero deflection. It was observed that the constancy of the force is dependent only on the initial beam-end angle and is independent of its material and other geometric properties. It increases as the initial angle tends to zero degrees. A fixed-free compliant beam generated near-constant force over a significant range of deflection in its post-buckling stage, i.e., its characteristic load is nearly the same as the Euler's critical load. Similarly, pinned-pinned, fixed-guided, and compound-compliant (SLFP) beams exerted near-constant force in their post-buckling stages. It was demonstrated with examples that the constancy of the force exerted by the existing compliant CFMs is predominantly due to this phenomenon. An optimized mechanism or cam surface at the beam end may generate an exact constant force over large deflections, but not necessary for producing near-constant force with simple, compliant segments. The theoretical results predicted by the PRBM-based model were validated experimentally for the three most common compliant segment types.

A novel compliant constant-force mechanism, the canted spring, was designed based on the new understanding of the mechanics of generating constant force. Heuristically, six configurations were derived for the canted spring and revised to eight

with a formalized approach for type synthesis. They were categorized into three groups based on the location of compliance in the mechanisms. The category III canted springs had the best potential to generate constant force over large deformations. The other two category springs exhibited non-linear force characteristics, which may be optimized as needed. The PRBM concept was utilized to model the canted spring for dimensional synthesis, and its force-displacement behavior was investigated using the virtual work principle. An optimization routine was developed for category III canted springs, which minimized the variation in the output force, producing more exact constancy. The parameters of the PRBM were normalized with the link length r_2 for optimization. Configurations were generated for different eccentricities of the ground pivot. A methodology was formulated to help design a constant-force canted spring from these optimized mechanisms for desired requirements.

The CFMs were arranged into modular units and array structures (CFM systems) to serve a wide range of high load-bearing and uniform pressure distribution applications. The modular units can be placed at a few columns of the bridge/structure to minimize the indeterminacy in the design. A simple methodology was developed to exemplify the construction of an array structure for uniform pressure distribution. The modular units can be part of arrays instead of a CFM to support and distribute the heavy loads throughout the structure.

8.2. FUTURE WORK RECOMMENDATIONS

Synthesis of a cam profile for the compliant segments, esp. for fixed-free beams, could be explored to generate an exact constant force. An optimization routine for category

I canted springs, similar to the current methodology, could be developed for the generation of near-constant force, at least for a partial range of its deflection. A study on minimizing indeterminacy by using CFM modular units in the bridge/structure design. Development of CFM array structures either rectangular, circular, or combination of both orientations for uniform pressure-distribution applications, such as seat cushions, bedding & furniture, and floors (for assembly-line workers and care centers).

APPENDIX A.

MATLAB CODES FOR DIMENSIONAL SYNTHESIS OF CANTED SPRING OPTIMIZATION FOR CATEGORY III MECHANISMS

1. CATEGORY III CANTED SPRING – E-POSITIVE CONFIGURATIONS

```matlab
close all
clear
clc

format long e

rng(0);

n = 10;

iter = 100000;

var = randi(n,5,iter);

tol = 1.065;              %9*10^-2; % accuracy tol

A = linspace(0.9,1.25,n);
B = linspace(0,0.5,n);
R = linspace(0,0.6,n);
R1 = linspace(0.05,0.9,n);
theta20 = linspace(pi/12,pi/3,n);
% E = linspace(0.000001,1,n);
% theta30 = linspace(pi/4,pi/2,n);
Optimal_Ans = [];

y = linspace(0.1,0.5,n);%control varable

ii = 1;

while ii <= iter

    A_var = A(var(1,ii));
    B_var = B(var(2,ii));
    R_var = R(var(3,ii));
    R1_var = R1(var(4,ii));
    theta20_var = theta20(var(5,ii));
    %     E_var = E(var(6,ii));
```

```matlab
%         theta30_var = theta30(var(7,ii));

    if (0 <  A_var) && (0.15*R_var <= B_var) && (0 < R_var)

        for i = 1:n

            theta2 = asin(sin(theta20_var)-y(i));

            theta30 = acos((cos(theta20_var)-
R1_var)/R_var);

            E = R_var*sin(theta30) - sin(theta20_var);

            theta3 = asin((E + sin(theta2))/R_var);

            abs_phi1(i) = abs((((theta30-theta20_var)-
(theta3-theta2))*((cos(theta2)/(R_var*cos(theta3)))-
1))/(A_var*cos(theta2)-B_var*sin(theta2)));
        end

        Difference = max(abs_phi1)-min(abs_phi1);
        Phi_avg = mean(abs_phi1);
        Alpha_Phi = max(abs_phi1)/min(abs_phi1);

        if Alpha_Phi <= tol

            Optimal_Ans = [Optimal_Ans;
                [Difference, A_var, B_var, R_var, R1_var ,
theta20_var, E, theta30, Phi_avg, Alpha_Phi]];

        end

    end

     ii = ii + 1;

end

kk = find( pi/3.75<=Optimal_Ans(:,8) &
Optimal_Ans(:,8)<=pi/2 );
```

```matlab
Optimal_Ans_2 = Optimal_Ans(kk,:);

% [~,Index_min] = min(Optimal_Ans_2(:,1));
%
% Answer = Optimal_Ans_2(Index_min,:);

kkk = find(Optimal_Ans_2(:,5) > 0.1);

Answer3 = Optimal_Ans_2(kkk,:);

kkkk = find(Answer3(:,7)>= 0.1);
Answer4 = Answer3(kkkk,:);

[~,Index_min] = min(Answer4(:,10));

Answer = Answer4(Index_min,:);

[~,MaxIndex] = max(Answer4(:,9));

Ans_MaxAlpha = Answer4(MaxIndex,:);

kmore = find(Answer3(:,10)<= 1.035);
More_Answer = Answer3(kmore,:);

kmore2 = find(More_Answer(:,9)>= 0.4);
More_Answer2 = More_Answer(kmore2,:);

Difference_Optimal = Answer(1)
A_Optimal = Answer(2)
B_Optimal = Answer(3)
R_Optimal = Answer(4)
R1_Optimal = Answer(5)
theta20_Optimal = Answer(6)*180/pi
Answer(6)
E_Optimal = Answer(7)
theta30_Optimal = Answer(8)*180/pi
Answer(8)
Phi_avg = Answer(9)
Alpha = Answer(10)
```

2. CATEGORY III CANTED SPRING – E-ZERO CONFIGURATIONS

```matlab
close all
clear
clc

format long e

rng(0);

n = 10;

iter = 100000;

var = randi(n,5,iter);

tol = 1.065;    %9*10^-2; % accuracy tol

A = linspace(0.9,1.25,n);
B = linspace(0,0.5,n);
R = linspace(0,0.6,n);
%R1 = linspace(0.05,0.6,n);
theta20 = linspace(pi/12,pi/3,n);
% E = linspace(0.000001,1,n);
% theta30 = linspace(pi/4,pi/2,n);
Optimal_Ans = [];

y = linspace(0.1,0.5,n);%control varable

ii = 1;

while ii <= iter

    A_var = A(var(1,ii));
    B_var = B(var(2,ii));
    R_var = R(var(3,ii));
    %R1_var = R1(var(4,ii));
    theta20_var = theta20(var(4,ii));
    %     E_var = E(var(6,ii));
```

```
%       theta30_var = theta30(var(7,ii));

    if (0 <  A_var) && (0.15*R_var <= B_var) && (0 < R_var)

        for i = 1:n

            theta2 = asin(sin(theta20_var)-y(i));

            theta30 = asin((0 + sin(theta20_var))/R_var);
% acos((cos(theta20_var)-R1_var)/R_var);

            E = R_var*sin(theta30) - sin(theta20_var);

            R1_var = cos(theta20_var) - R_var*cos(theta30);

            theta3 = asin((0 + sin(theta2))/R_var);

            abs_phi1(i) = abs((((theta30-theta20_var)-
(theta3-theta2))*((cos(theta2)/(R_var*cos(theta3)))-
1))/(A_var*cos(theta2)-B_var*sin(theta2)));
        end

        Difference = max(abs_phi1)-min(abs_phi1);
        Phi_avg = mean(abs_phi1);
        Alpha_Phi = max(abs_phi1)/min(abs_phi1);

        if (Alpha_Phi <= tol)

            Optimal_Ans = [Optimal_Ans;
                [Difference, A_var, B_var, R_var, R1_var ,
theta20_var, E, theta30, Phi_avg, Alpha_Phi]];

        end

    end

    ii = ii + 1;

end
```

```matlab
kk = find( pi/3.75<=Optimal_Ans(:,8) &
Optimal_Ans(:,8)<=pi/2 );

Optimal_Ans_2 = Optimal_Ans(kk,:);

% [~,Index_min] = min(Optimal_Ans_2(:,1));
%
% Answer = Optimal_Ans_2(Index_min,:);

kkk = find(Optimal_Ans_2(:,5) > 0.1);

Answer3 = Optimal_Ans_2(kkk,:);

[~,Index_min] = min(Answer3(:,10));

Answer = Answer3(Index_min,:);

[~,MaxIndex] = max(Answer3(:,9));

Ans_MaxAlpha = Answer3(MaxIndex,:);

kmore = find(Answer3(:,10)<= 1.05);
More_Answer = Answer3(kmore,:);

kmore2 = find(More_Answer(:,9)>= 0.4);
More_Answer2 = More_Answer(kmore2,:);

Difference_Optimal = Answer(1)
A_Optimal = Answer(2)
B_Optimal = Answer(3)
R_Optimal = Answer(4)
R1_Optimal = Answer(5)
theta20_Optimal = Answer(6)*180/pi
Answer(6)
E_Optimal = Answer(7)
theta30_Optimal = Answer(8)*180/pi
Answer(8)
Phi_avg = Answer(9)
Alpha = Answer(10)
```

3. CATEGORY III CANTED SPRING – E-NEGATIVE CONFIGURATIONS

```matlab
close all
clear
clc

format long e

rng(0);

n = 10;

iter = 100000;

var = randi(n,5,iter);

tol = 1.065;                %9*10^-2; % accuracy tol

A = linspace(0.9,1.25,n);
B = linspace(0,0.5,n);
R = linspace(0,0.6,n);
R1 = linspace(0.05,0.9,n);
theta20 = linspace(0,pi/3,n);
% E = linspace(0.000001,1,n);
% theta30 = linspace(pi/4,pi/2,n);
Optimal_Ans = [];

y = linspace(0.05,0.35,n);%control varable

ii = 1;

while ii <= iter

    A_var = A(var(1,ii));
    B_var = B(var(2,ii));
    R_var = R(var(3,ii));
    R1_var = R1(var(4,ii));
    theta20_var = theta20(var(5,ii));
    %      E_var = E(var(6,ii));
```

```matlab
%       theta30_var = theta30(var(7,ii));

    if (0 <  A_var) && (0.15*R_var <= B_var) && (0 < R_var)

        for i = 1:n

            theta2 = asin(sin(theta20_var)-y(i));

            theta30 = acos((cos(theta20_var)-
R1_var)/R_var);

            E = R_var*sin(theta30) - sin(theta20_var);

            theta3 = asin((E + sin(theta2))/R_var);

            abs_phi1(i) = abs((((theta30-theta20_var)-
(theta3-theta2))*((cos(theta2)/(R_var*cos(theta3)))-
1))/(A_var*cos(theta2)-B_var*sin(theta2)));
        end

        Difference = max(abs_phi1)-min(abs_phi1);
        Phi_avg = mean(abs_phi1);
        Alpha_Phi = max(abs_phi1)/min(abs_phi1);

        if Alpha_Phi <= tol

            Optimal_Ans = [Optimal_Ans;
                [Difference, A_var, B_var, R_var, R1_var ,
theta20_var, E, theta30, Phi_avg, Alpha_Phi]];

        end

    end

     ii = ii + 1;

end

kk = find( pi/3.75<=Optimal_Ans(:,8) &
Optimal_Ans(:,8)<=pi/2 );
```

```matlab
Optimal_Ans_2 = Optimal_Ans(kk,:);

% [~,Index_min] = min(Optimal_Ans_2(:,1));
% Answer = Optimal_Ans_2(Index_min,:);

kkk = find(Optimal_Ans_2(:,5) > 0.1);

Answer3 = Optimal_Ans_2(kkk,:);

kkkk = find(Answer3(:,7) < 0);
Answer4 = Answer3(kkkk,:);

[~,Index_min] = min(Answer4(:,10));

Answer = Answer4(Index_min,:);

[~,MaxIndex] = max(Answer4(:,9));

Ans_MaxAlpha = Answer4(MaxIndex,:);

kmore = find(Answer4(:,10)<= 1.05);
More_Answer = Answer4(kmore,:);

kmore2 = find(More_Answer(:,9)>= 0.4);
More_Answer2 = More_Answer(kmore2,:);

Difference_Optimal = Answer(1)
A_Optimal = Answer(2)
B_Optimal = Answer(3)
R_Optimal = Answer(4)
R1_Optimal = Answer(5)
theta20_Optimal = Answer(6)*180/pi
Answer(6)
E_Optimal = Answer(7)
theta30_Optimal = Answer(8)*180/pi
Answer(8)
Phi_avg = Answer(9)
Alpha = Answer(10)
```

APPENDIX B.

**ANSYS APDL CODE FOR VALIDATING THE RESULTS PREDICTED BY
PRBM-BASED MODEL FOR CANTED SPRING EXAMPLE**

The following ANSYS Mechanical APDL program computes the force exerted by the Canted Spring example in section 6.5 (Figure 6.15). The code computes the force for one input displacement at a time, hence it has to be executed for a few displacement inputs to get understand its force-displacement behavior.

```
!######################## START OF COMMAND FILE ####################
! This command file is for analysis of a Canted Spring with one flexible segment, slider, and ground pin-joint


finish
/clear                              ! Clear previous data


!ENTERING PRE PROCESSOR MODULE
/prep7                              ! Enter preprocessor mode


!DEFINE ELEMENT TYPES
et,1,beam188                        ! Regular beam elements

et,2,mpc184,6                       ! Pin-joint elements


!DEFINE MATERIALS
mp,ex,1,30e6                        ! Modulus of elasticty for material 1

mp,prxy,1,0.3                       ! Poissons ratio for material 1
```

!DEFINE SECTIONS FOR FLEXIBLE AND RIGID LINKS

sectype,1,beam,rect,flexible,0   ! Section type for flexible segment

secdata,0.04,0.65   ! Section properties for section 1

sectype,2,beam,rect,rigid,0   ! Section type for rigid segment

secdata,0.3,1   ! Section properties for section 2

!Nodes for Rigid segment and pin-joint

N , 1 , 0 , 0 , 0 $

N , 2 , 0 , 0.8 , 0 $

!Node for pin-joint

N , 3 , 0 , 0.8 , 0 $

!Nodes for Rigid segment - positive pitch segment

N , 3 , 0 , 0.8 , 0 $

N , 4 , 3.8036 , 3.5866 , 0 $

N , 5 , 3.9747 , 3.6904 , 0 $

N , 6 , 4.1661 , 3.7664 , 0 $

N , 7 , 4.3804 , 3.8089 , 0 $

N , 8 , 4.4942 , 3.8154 , 0 $

N , 9 , 4.5804 , 3.8127 , 0 $

N , 10 , 4.7804 , 3.7822 , 0 $

N , 11 , 4.9804 , 3.7145 , 0 $

!NODES for FLEXIBLE segment - negative pitch segment

N , 12 , 5.1799 , 3.6022 , 0 $

N , 13 , 5.1456 , 3.5 , 0 $

N , 14 , 5.112 , 3.4 , 0 $

N , 15 , 5.0784 , 3.3 , 0 $

N , 16 , 5.0448 , 3.2 , 0 $

N , 17 , 5.0112 , 3.1 , 0 $

N , 18 , 4.9776 , 3 , 0 $

N , 19 , 4.944 , 2.9 , 0 $

N , 20 , 4.9105 , 2.8 , 0 $

N , 21 , 4.8769 , 2.7 , 0 $

N , 22 , 4.8433 , 2.6 , 0 $

N , 23 , 4.8097 , 2.5 , 0 $

N , 24 , 4.7761 , 2.4 , 0 $

N , 25 , 4.7425 , 2.3 , 0 $

N , 26 , 4.7089 , 2.2 , 0 $

N , 27 , 4.6753 , 2.1 , 0 $

N , 28 , 4.6417 , 2 , 0 $

N , 29 , 4.6081 , 1.9 , 0 $

N , 30 , 4.5745 , 1.8 , 0 $

N , 31 , 4.5409 , 1.7 , 0 $

N , 32 , 4.5073 , 1.6 , 0 $

N , 33 , 4.4737 , 1.5 , 0 $

N   ,   34   ,   4.4402 ,   1.4   ,   0 $

N   ,   35   ,   4.4066 ,   1.3   ,   0 $

N   ,   36   ,   4.373 ,   1.2   ,   0 $

N   ,   37   ,   4.3394 ,   1.1   ,   0 $

N   ,   38   ,   4.3058 ,   1   ,   0 $

N   ,   39   ,   4.2722 ,   0.9   ,   0 $

N   ,   40   ,   4.2386 ,   0.8   ,   0 $

N   ,   41   ,   4.205 ,   0.7   ,   0 $

N   ,   42   ,   4.1714 ,   0.6   ,   0 $

N   ,   43   ,   4.1378 ,   0.5   ,   0 $

N   ,   44   ,   4.1042 ,   0.4   ,   0 $

N   ,   45   ,   4.0706 ,   0.3   ,   0 $

N   ,   46   ,   4.037 ,   0.2   ,   0 $

N   ,   47   ,   4.0034 ,   0.1   ,   0 $

N   ,   48   ,   3.9699 ,   0   ,   0 $

!SELECT ELEMENT, MATERIAL and SECTION PROPERTIES FOR ground (E

positive)

TYPE,1 $ MAT,1 $ SECNUM,2

!defining rigid element

EN,1,1,2

!REVOLUTE JOINT

sectype,3,joint,revo,pinjoint

!SELECT ELEMENT, MATERIAL and SECTION PROPERTIES FOR Pin-Joint

TYPE,2 $ MAT,1 $ SECNUM,3

local,11,0,0,0.8,0, , ,90 $ secjoint,,11,11

csys,11

!ELEMENT FOR ground PIN JOINT

EN,2,2,3

!SELECT ELEMENT, MATERIAL and SECTION PROPERTIES FOR Positive-Pitch

RIGID SEGMENT

TYPE,1 $ MAT,1 $ SECNUM,2   ! Selecting element 1, material 1 and

section 2 for further use

!DEFINE ELEMENTS FOR Positive-Pitch Rigid Segment

EN,3,3,4 $ EN,4,4,5 $ EN,5,5,6 $ EN,6,6,7 $ EN,7,7,8 $ EN,8,8,9 $ EN,9,9,10 $

EN,10,10,11 $ EN,11,11,12

!SELECT ELEMENT, MATERIAL and SECTION PROPERTIES FOR Negative-Pitch

Flexible Segment

TYPE,1 $ MAT,1 $ SECNUM,1   ! Selecting element 1, material 1 and

section 1 for further use

!DEFINE ELEMENTS FOR Positive-Pitch Rigid Segment

EN,12,12,13 $ EN,13,13,14 $ EN,14,14,15 $ EN,15,15,16 $ EN,16,16,17

EN,17,17,18 $ EN,18,18,19 $ EN,19,19,20 $ EN,20,20,21 $ EN,21,21,22 $ EN,22,22,23

$ EN,23,23,24

EN,24,24,25 $ EN,25,25,26 $ EN,26,26,27 $ EN,27,27,28 $ EN,28,28,29 $ EN,29,29,30

$ EN,30,30,31

EN,31,31,32 $ EN,32,32,33 $ EN,33,33,34 $ EN,34,34,35 $ EN,35,35,36 $ EN,36,36,37

$ EN,37,37,38

EN,38,38,39 $ EN,39,39,40 $ EN,40,40,41 $ EN,41,41,42 $ EN,42,42,43 $ EN,43,43,44

$ EN,44,44,45

EN,45,45,46 $ EN,46,46,47 $ EN,47,47,48

finish

!ENTERING SOLUTION MODULE

/solu

!ANALYSIS TYPE AND PROPERTIES

antype,0 $ autots,1 $ nlgeom,1 $ nsubst,10,1000,1 $ outres,all,all

```
        ! Static analysis, auto time stepping on, nonlinear geometry on substep

requirements

time,1                                  ! maximum time of analysis


!DEFINE CONSTRAINTS

d,1,all,0                               ! Fixity constraint at ground

d,48,uy,0                               ! y Displacement constraint to slider point

!d,31,uz,0                              ! z Displacement constraint to slider point

!d,50,rotz,-0.5                         ! theta Displacement constraint to coupler

point

!f,50,fx,-200                           ! load constraint at coupler point, fx

d,8,uy,-1.6                             ! Displacement input at apex point, dy


solve


!ENTERING POST PROCESSOR MODULE

/post1

/eshape,1                               ! Display as a solid geometry

plns,u,sum $ /replot                    ! Plot displacement

plns,s,eqv $ /replot                    ! Plot stress

!antime,20,0.5,,1,2,0,1                       ! Animation controls

!anim,10,1,0.5                          ! Animation controls

prenergy,sene             ! Display total strain energy stored in the mechanism
```

/post26

nsol,2,48,u,x,sliderdisp   ! Store nodal displacements at all time steps

(load steps), ux

!nsol,3,50,u,y,ydisp50   ! Store nodal displacements at all time steps

(load steps), uy

!prvar,2,3   ! Display command to list nodal

displacements at all time steps (load steps), ux and uy

!######################### END OF COMMAND FILE #######################

APPENDIX C.

**MATLAB CODE FOR GENERATING CFM RECTANGULAR ARRAY
STRUCTURE**

This MATLAB code is part of the design methodology to develop rectangular CFM array structure for given load and size requirements.

```matlab
clc;
clear all;
close all;
m = input('enter the # of rows - array (odd number
only):');
n = input('enter the # of columns - array (odd number
only):');
d = input('enter the distance between two adjacent
elements:'); %for time being assume the module as a point
%f = 12; %the constant reaction force of the module with 4
canted springs with each offering 3lb reaction force
def = 1; % max deflection of the center module
z = zeros(m,n);
r1 = input('radius of the first circle:');
r2 = input('radius of the second circle:');
a = ceil(m/2); % ceil = round of to next integer % the
center row
b = ceil(n/2);  % the center column
b1 = floor(b/2);    % the center column for sphere 1
b2 = b + ceil(b/2); % the center column for sphere 2

[z(a,b1), z(a,b2)] = deal(def); % max defelction is
assigned the center elements for both spheres
h1 = r1 - def;  % the distance from center of the sphere to
part not dipressed into teh bed --> see figure in notes
h2 = r2 - def;
bmin = min(a, b1); % to get the least distance from the
center element to box sides


% if (r1+r2) <= (b2-b1)*d
for i = 1:(bmin-1)
    j = 0;
     e = sqrt((i*d)^2 + (j*d)^2);
    [z(a-i,b1),z(a+i,b1),z(a,b1-i),z(a,b1+i)]=
deal(sqrt(r1^2 - e^2)- h1); %deal= to assign the same value
to different variables

    for j1 = 1:i
        e = sqrt((i*d)^2 + (j1*d)^2);
```

```matlab
        [z(a-i,b1-j1),z(a-i,b1+j1),z(a+i,b1-
j1),z(a+i,b1+j1),z(a-j1,b1-i),z(a-j1,b1+i),z(a+j1,b1-
i),z(a+j1,b1+i)]= deal(sqrt(r1^2 - e^2)- h1);
    end
end

for i = 1:(bmin-1)
    j = 0;
    e = sqrt((i*d)^2 + (j*d)^2);
    [z(a-i,b2),z(a+i,b2),z(a,b2-i),z(a,b2+i)]=
deal(sqrt(r2^2 - e^2)- h2); %deal= to assign the same value
to different variables

    for j1 = 1:i
        e = sqrt((i*d)^2 + (j1*d)^2);
        [z(a-i,b2-j1),z(a-i,b2+j1),z(a+i,b2-
j1),z(a+i,b2+j1),z(a-j1,b2-i),z(a-j1,b2+i),z(a+j1,b2-
i),z(a+j1,b2+i)]= deal(sqrt(r2^2 - e^2)- h2);
    end
end
% else
%     fprintf('the two circles are not arranged properly');
% end


for k = 1:m
    for l = 1:n
        if (z(k,l)<= 0) % non-contact elements
            z(k,l) = 0;
        else
            z(k,l) = -1*z(k,l); %contact lements with
negative sign for depression plot
        end
    end
end

x1 = [0 n*d n*d 0 0];
y1 = [0 0 m*d m*d 0];
z1 = [0 0 0 0 0];
z11 = [-1 -1 -1 -1 -1];
x2 = [0 n*d n*d 0; 0 n*d n*d 0];
y2 = [0 0 m*d m*d; 0 0 m*d m*d];
z2 = [0 0 0 0; -1 -1 -1 -1];
xp = zeros(m,n);
yp = zeros(m,n);
for k = 1:m
```

```matlab
    for l = 1:n
        xp(k,l) = l*d - d/2;    % x cooordinates for array-
elment points    % d/2 is distance from boxside to element
1
        yp(k,l) = k*d - d/2;    % y cooordinates for array-
elment points
    end
end
zp = zeros(m,n);

subplot(1,2,1);
plot3(x1, y1, z1, '-b' );    %3D plot of upper box
hold on;
plot3(x1, y1, z11, '-b');    %3D plot of lower box
hold on;
plot3(x2,y2,z2,'-b');        % sides of teh cuboid box
hold on;
plot3(xp, yp, zp, '*r');     % points fro array elements
surface(xp, yp, zp);         % substrate on the points
axis equal;

subplot(1,2,2);
plot3(x1, y1, z1, '-b' );
hold on;
plot3(x1, y1, z11, '-b');
hold on;
plot3(x2,y2,z2,'-b');
hold on;
plot3(xp, yp, zp, '*r');
% surface(xp, yp, zp);
[xs1, ys1, zs1] = sphere();      %sphere function with
xs1,ys1,zs1 as center
surf(r1*xs1+xp(a,b1), r1*ys1+yp(a,b1),
r1*zs1+(zp(a,b1)+r1),'FaceColor',[0.25 0.25
0.25],'FaceAlpha',0.75);      %definign the center & color
[xs2, ys2, zs2] = sphere();
surf(r2*xs2+xp(a,b2), r2*ys2+yp(a,b2),
r2*zs2+(zp(a,b2)+r2),'FaceColor',[0.25 0.25
0.25],'FaceAlpha',0.75);
axis equal;

figure(2)
subplot(1,2,1);
plot3(x1, y1, z1, '-b' );
hold on;
plot3(x1, y1, z11, '-b');
```

```matlab
hold on;
plot3(x2,y2,z2,'-b');
hold on;
plot3(xp, yp, z, '*r');        %depressed points
surface(xp, yp, z);            %substrate
axis equal;

subplot(1,2,2);
plot3(x1, y1, z1, '-b' );
hold on;
plot3(x1, y1, z11, '-b');
hold on;
plot3(x2,y2,z2,'-b');
hold on;
plot3(xp, yp, z, '*r');
surface(xp, yp, z);
[xs1, ys1, zs1] = sphere();
surf(r1*xs1+xp(a,b1), r1*ys1+yp(a,b1),
r1*zs1+(z(a,b1)+r1),'FaceColor',[0.25 0.25
0.25],'FaceAlpha',0.75);
[xs2, ys2, zs2] = sphere();
s = surf(r2*xs2+xp(a,b2), r2*ys2+yp(a,b2),
r2*zs2+(z(a,b2)+r2),'FaceColor',[0.25 0.25
0.25],'FaceAlpha',0.75);
axis equal;
% get(s)
sp1 = z(1:m,1:b);
sp2 = z(1:m,b:n);
count_1 = nnz(sp1);
count_2 = nnz(sp2);
```

BIBLIOGRAPHY

[1]   Midha, A., and Her, I., "Research Notes," Purdue University, West Lafayette, IN, 1985.

[2]   Midha, A., Norton, Tony W., and Howell, L. L. "On the Nomenclature, Classification and Abstractions of Compliant Mechanisms," *ASME Journal of Mechanical Design*, Vol. 116, No. 1, pp. 270-279, 1994.

[3]   Visser C. S., and Midha, A. "Compliant Pliers," US Patent 5522290A, 1994.

[4]   SMINT® Mint Dispenser, https://www.smint.co.uk/, July 2022.

[5]   Kuber, R. S., "Development of a Methodology for Pseudo-Rigid-Body Models of Compliant Segments with Inserts, and Experimental Validations," MS Thesis, Missouri University of Science and Technology, Rolla, MO, 2013.

[6]   Crews, J. A., "Methodology for Analysis of Stress, Creep, and Fatigue Behavior of Compliant Mechanisms," MS Thesis, Missouri University of Science and Technology, Rolla, MO, 2016.

[7]   The Mars Curiosity Rover Wheels and Legs, https://mars.nasa.gov/msl/spacecraft/rover/wheels/, July 2022.

[8]   Michelin X Tweel Airless Radial Tire, www.michelintweel.com, July 2022.

[9]   Adidas Springblade: Shoes with Actual Springs Might Be a Good Idea, https://www.gizmodo.com.au/2013/06/adidas-springblade-shoes-with-actual-springs-might-be-a-good-idea/, July 2022.

[10]   Flight Flexor Footrest, https://www.ergocentric.com/product/foot-flexor/, June 2022.

[11]   Mettlach, G. A., Khanuja, S. S., and Midha, A. "Design of an Ergonomic Compliant Modular Chair," *Proceedings of 4th National Applied Mechanisms and Robotics Conference*, pp. AMR95-009-1-10, December 1995.

[12]   Davidson, M., "Innovative Lives: Artificial Parts – Van Phillips," https://invention.si.edu/innovative-lives-artificial-parts-van-phillips, July 2022.

[13]   Ossur hf.., "Flex-Foot Cheetah," Master Prosthetic Catalog, https://assets.ossur.com/library/39389/Flex-Foot%20Cheetah%20Catalog%20page%20-%202018.pdf, June 2022.

[14] Halverson, P. A., Bowden, A. E., and Howell, L. L., "A Compliant-Mechanism Approach to Achieving Specific Quality of Motion in a Lumbar Total Disc Replacement," *International Journal of Spine Surgery*, Vol. 6: pp. 78-86, 2012.

[15] TED Speaker Nikolai Begg, https://www.ted.com/speakers/nikolai_begg, June 2022.

[16] Cronin, J., Frecker, M., and Mathew, A., "Design of a Compliant Endoscopic Suturing Instrument," *Proceedings ASME Design Engineering Technical Conference*, September 2007.

[17] AMP Inc. Crimping Tool and Chip Extractor, Courtesy of Midha, A., January 2020.

[18] Wahl, A. M., *Mechanical Springs,* Penton Publishing Company, Cleveland, OH, 1944.

[19] Nathan, R. H. "A Constant Force Generation Mechanism," *ASME Journal of Mechanisms, Transmissions, and Automation in Design*, Vol. 107 No. 4: pp. 508-512, 1989.

[20] Williman, J., "Small Torque," *Engineering* (London), Gillard Welch Associates, London, pp. 27-28, 1995.

[21] Jenuwine, J. G., and Midha, A., "Design of an Exact Constant Force Generating Mechanism," *Proceedings of the 1st National Applied Mechanics & Robotics Conference*, Vol. II: pp. 10B-4-1 -10B-4-5, Cincinnati, OH, 1989.

[22] Jenuwine, J. G., and Midha, A., "Synthesis of Single-Input and Multiple-Output Port Mechanisms with Springs for Specified Energy Absorption," *ASME Journal of Mechanical Design*, Vol. 116: 937-943, 1994.

[23] Midha, A., "Compliant Mechanisms: Memory Lane, the Journey, and the Exciting Road Ahead," *Proceedings of the ASME International Design Engineering Technical Conferences and Computers and Information in Engineering Conference*, Presentation, Las Vegas, Nevada, September 05, 2007.

[24] Murphy, M. D., "A Generalized Theory for the Type Synthesis and Design of Compliant Mechanisms," Ph.D. Dissertation, Purdue University, West Lafayette, IN, 1993.

[25] Murphy, M. D., Midha, A., and Howell, L. L., "Methodology for the Design of Compliant Mechanisms Employing Type Synthesis Techniques with Example," *Proceedings of the ASME Mechanisms Conference, Mechanism Synthesis and Analysis*, DE-Vol. 70: pp. 61-66, 1994.

[26] Howell, L. L., "A Generalized Loop-Closure Theory for the Analysis and Synthesis of Compliant Mechanisms," Ph.D. Dissertation, Purdue University, West Lafayette, IN. 1993.

[27] Howell, Larry L., Midha, Ashok, and Murphy, Morgan D. "Dimensional Synthesis of Compliant Constant-Force Slider Mechanisms." *Proceedings of the ASME Design Engineering Technical Conferences*, DE-Vol. 71: 23rd Biennial Machine Elements and Machine Dynamics. pp. 509-515. New York, NY, June 1994.

[28] Midha, A., Murphy, M. D., and Howell, L. L., "Compliant Constant-Force Mechanism and Devices Formed Therewith," *US Patent 5649454*, 1997.

[29] Millar, A. J., Howell, L. L., and Leonard, J. N., "Design and Evaluation of Compliant Constant-Force Mechanisms," *Proceedings of the ASME Design Engineering Technical Conferences and Computers in Engineering Conference*, DETC/MECH-1209: pp. 1-12, Irvine, CA, August 18-22, 96-, 1996.

[30] Parkinson, M. B., Howell, L. L., and Cox, J. J., "A Parametric Approach to the Optimization-Based Design of Compliant Mechanisms," *Proceedings of the ASME Design Engineering Technical Conferences, 23rd Design Automation Conference*, DETC97/DAC-3763: pp. 1-8.,Sacramento, CA, September 14-17, 1997.

[31] Weight, B. L., "Development and Design of Constant-Force Mechanisms," M.S. Thesis, Brigham Young University, Provo, UT, 2001.

[32] Weight, B. L., Magleby, S. P., and Howell, L. L., "Selection of Compliant Constant-Force Mechanisms Based on Stress and Force Criteria," *Proceedings of the ASME International Design Engineering Technical Conferences and Computers and Information in Engineering Conference, 27th Biennial Mechanisms and Robotics Conference*, Vol. 5: DETC2002/MECH-34206: pp. 51-63, Quebec, Canada, September 29-October 2, 2002.

[33] Boyle, C., Howell, L. L., Magleby, S. P., and Evans, M. S., "Dynamic Modeling of Compliant Constant-Force Compression Mechanisms," *Mechanism and Machine Theory*, Vol. 38(12): pp. 1469-1487, 2003.

[34] Weight, B. L., Mattson, C. A., Magleby, S. P., and Howell, L. L., "Configuration Selection, Modeling, and Preliminary Testing in Support of Constant Force Electrical Connectors," *ASME Journal of Electronic Packaging*, Vol. 129(3): pp. 236-246, 2007.

[35] Jutte, C. V., "Generalized Synthesis Methodology of Nonlinear Springs for Prescribed Load-Displacement Functions," Ph.D. Dissertation, University of Michigan, Ann Arbor, MI, 2008.

[36] Rahman, M. Ur., and Zhou, H., "Design of Constant Force Compliant Mechanisms," *International Journal of Engineering Research & Technology*, Vol. 3(7): pp. 14-19, 2014.

[37] Christian, A. J., "On the Dynamic Analysis of Compliant Mechanisms Based on the Pseudo-Rigid-Body Model," M.S. Thesis, Missouri University of Science and Technology, Rolla, MO, 2015.

[38] Liu, Y., and Xu, Q., "Design of a Compliant Constant Force Gripper Mechanism Based on Buckled Fixed-Guided Beam," *Proceedings of the International Conference on Manipulation, Automation and Robotics at Small Scales (MARSS)*, pp. 1-6, Paris, France, July 18-22, 2016.

[39] Wang, P., and Xu, Q., "Design of a Flexure-Based Constant-Force XY Precision Positioning Stage," *Mechanism and Machine Theory*, Vol. 108: pp. 1-13, 2017.

[40] Wang, P., and Xu, Q., "Design and Modeling of Constant-Force Mechanisms: A Survey," *Mechanism and Machine Theory*, Vol. 119: pp. 1-21, 2018.

[41] Ma, F., Chen, G., and Wang, H., "Large-Stroke Constant-Force Mechanisms Utilizing Second Bending Mode of Flexible Beams: Evaluation Metrics and Design Approach," *Proceedings of the ASME International Design Engineering Technical Conferences and Computers and Information in Engineering Conference, Mechanisms and Robotics Conference*, DETC2019-97813: pp. 1-9, Anaheim, CA, August 18-21, 2019.

[42] Evans, M. S., and Howell, L. L., "Constant-Force End-Effector Mechanism," *Proceedings of the IASTED International Conference, Robotics and Application*, pp. 250-256, Santa Barbara, CA, October 28-30, 1999.

[43] Herder, J. L., and Tuijthof, G. J. M., "Two Spatial Gravity Equilibrators," *Proceedings of the ASME Design Engineering Technical Conferences and Computer in Engineering Conference, 26th Biennial Mechanisms and Robotics Conference*, DETC2000/MECH-14120: pp. 643-652, Baltimore, MD, September 10-13, 2000.

[44] Herder, J. L., and Van Den Berg, F. P. A., , "Statically Balanced Compliant Mechanisms (SBCM's), An Example and Prospects," *Proceedings of the ASME Design Engineering Technical Conferences and Computer in Engineering Conference, 26th Biennial Mechanisms and Robotics Conference*, DETC2000/MECH-14144, Baltimore, MD, September 10-13, 2000.

[45]   Nahar, D. R., and Sugar, T., "Compliant Constant-Force Mechanism with a Variable Output for Micro/Macro Applications," *Proceedings of the IEEE International Conference on Robotics and Automation*, pp. 318-323, Taipei, Taiwan, September 14-19, 2003.

[46]   Frischknecht, B. D., Howell, L. L., and Magleby, S. P., "Crank-Slider with Spring Constant Force Mechanism," *Proceedings of the ASME International Design Engineering Technical Conferences and Computers and Information in Engineering Conference, 28th Biennial Mechanisms and Robotics Conference*, Vol. 2, DETC2004-57318: pp. 809-817, Salt Lake City, UT, September 28-October 2, 2004.

[47]   Howell, L. L., and Magleby, S. P., "Substantially Constant-Force Exercise Machine," *U.S. Patent Application No. 7060012*, 2006.

[48]   Lan, C-C., Wang, J-H., and Chen, Y-H., "A Compliant Constant-Force Mechanism for Adaptive Robot End-Effector Operations," *Proceedings of the IEEE International Conference on Robotics and Automation*, pp. 2131-2136, Anchorage, AK, May 3-8, , 2010.

[49]   Pham, H-T., and Wang, D-A., "A Constant-Force Bistable Mechanism for Force Regulation and Overload Protection," *Mechanism and Machine Theory*, Vol. 46(7): pp. 899-909, 2011.

[50]   Tolou, N., Pluimers, P. P., Jensen, B., D., Magleby, S., Howell, L. L., and Herder, J. L., "Constant Force Micro Mechanism out of Carbon Nanotube Forest," *Proceedings of the 12th EUSPEN International Conference*, pp. 1-4, Stockholm, Sweden, June 2011.

[51]   Tolou, N., Pluimers, P. P., Jensen, B. D., Magleby, S., Howell, L. L., and Herder, J. L., "Carbon-Nanotube-Based Constant Force Mechanisms," *Proceedings of the First DSPE Conference on Precision Mechatronics, an Initiative of DSPE and Brainport Industries*, Deurne, Netherlands, September 4-5, 2012.

[52]   Zirbel, S. A., Aten, Q. T., Easter, M., Jensen, B. D., and Howell, L. L., "Compliant Constant-Force Micro-Mechanism for Enabling Dual-Stage Motion," *Proceedings of the ASME International Design Engineering Technical Conferences and Computers and Information in Engineering Conference, 36th Mechanisms and Robotics Conference*, Vol. 4, DETC2012-70321: pp. 191-198, Chicago, IL, August 12-15, 2012.

[53]   Parlaktaş, V., "Spatial Compliant Constant-Force Mechanism," *Mechanism and Machine Theory*, Vol. 67: pp. 152-165, 2013.

[54]   Karthik, K., , "On the Design of a Nearly Constant-Force Modular Device Based on a Compliant Slider Mechanism," M.S. Thesis, Missouri University of Science and Technology, Rolla, MO, 2015.

[55]   Manousos, N., "Technical Perspective: The Where, How, and Why of Constant Force Mechanisms in Watchmaking," https://www.hodinkee.com/articles/a-close-look-at-constant-force-in-watchmaking. December 22, 2022.

[56]   Liu, Y., Yu, D-P., and Yao, J., "Design of an Adjustable Cam Based Constant Force Mechanism," *Mechanism and Machine Theory*, Vol. 103: pp. 85-97, 2016.

[57]   Tolman, K. A., Merriam, E. G., and Howell, L. L., "Compliant Constant-Force Linear-Motion Mechanism," *Mechanism and Machine Theory*, Vol. 106: pp. 68-79, 2016.

[58]   Lambert, P., and Herder, J. L., "An Adjustable Constant Force Mechanism Using Pin Joints and Springs," *New Trends in Mechanism and Machine Science. Mechanisms and Machine Science*, Vol. 43: pp. 453-461, Springer, Cham, 2017.

[59]   Liu, Y., Zhang, Y., and Xu, Q., "Design and Control of a Novel Compliant Constant-Force Gripper Based on Buckled Fixed-Guided Beams," *IEEE/ASME Transactions on Mechatronics*, Vol. 22(1): pp. 476-486, 2017.

[60]   Hasara, S., and Lusk, C., "A Load-Adjustable Constant-Force Mechanism," *Proceedings of the ASME International Design Engineering Technical Conferences and Computers and Information in Engineering Conference, 42nd Mechanisms and Robotics Conference*, Quebec City, Quebec, Canada, Vol. 5A, DETC2018-86246: pp. V05AT07A019: 1-5, August 26-29, 2018.

[61]   Zhang, X., Wang, G., and Xu, Q., "Design, Analysis and Testing of a New Compliant Compound Constant-Force Mechanism," *Actuators*, Vol. 7(4): pp. 65, 2018.

[62]   Zhang, X., and Xu, Q., "Design and Analysis of a Compound Constant-Force Mechanism for Compliant Gripper," *Proceedings of the International Conference on Manipulation, Automation and Robotics at Small Scales (MARSS)*, Nagoya, pp. 1-6, Japan, July 4-8, 2018.

[63]   Jutte, C. V., and Kota, S., "Design of Single, Multiple, and Scaled Nonlinear Springs for Prescribed Nonlinear Responses," *ASME Journal of Mechanical Design*, Vol. 132, No. 1: pp. 011003-1-011003-10, 2010.

[64]   Salamon, B., "Mechanical Advantage Aspects in Compliant Mechanisms Design," M.S. Thesis, Purdue University, West Lafayette, IN, 1989.

[65]   Howell, L. L., "The Design and Analysis of Large-Deflection Members in Compliant Mechanisms," M.S. Thesis, Purdue University, West Lafayette, IN, 1991.

[66]   Midha, A., "Chapter 9: Elastic Mechanisms," The First Forty Years of Modern Kinematics – A Tribute to Ferdinand Freudenstein, Erdman, A. G., ed., *Proceedings, Minneapolis/Brainerd*, pp. 9-1-9 – 9-1-60, MN, July 1993.

[67]   Howell, L. L., and Midha, A., "A Method for the Design of Compliant Mechanisms with Small-Length Flexural Pivots," *ASME Journal of Mechanical Design*, Vol. 116(1): pp. 280-290, 1994.

[68]   Howell, L. L., and Midha, A., "Parametric Deflection Approximations for End-Loaded, Large-Deflection Beams in Compliant Mechanisms," *ASME Journal of Mechanical Design*, Vol. 117(1): pp. 156-165, 1995.

[69]   Norton, T. W., "On the Nomenclature, Classification, and Mobility of Compliant Mechanisms," M.S. Thesis, Purdue University, West Lafayette, IN, 1991.

[70]   Howell, L. L., Midha, A., and Norton, T. W., "Evaluation of Equivalent Spring Stiffness for Use in a Pseudo-Rigid-Body Model of Large-Deflection Compliant Mechanisms," *ASME Journal of Mechanical Design*, Vol 118(1): pp. 126-131, 1996.

[71]   Howell, L. L., *Compliant Mechanisms*, John Wiley & Sons, Inc., New York, NY, 2001.

[72]   Bisshopp, K. E., and Drucker, D. C. "Large Deflection of Cantilever Beams," *Quarterly of Applied Mathematics*, Vol. 3, No. 3, pp. 272-275, 1945.

[73]   Pauly, J., and Midha, A., "Improved Pseudo-Rigid-Body Model Parameter Values for End-Force-Loaded Compliant Beams," *Proceedings of the IDETC/CIE*, DETC2004-57580: pp. 1513-1517. Salt Lake City, UT, September 28 - October 2, 2004.

[74]   Midha, A., Kuber, R, Chinta, V, and Bapat, S. G. "A Method for a More Accurate Calculation of the Stiffness Coefficient in a Pseudo-Rigid-Body Model (PRBM) of a Fixed-Free Beam Subjected to End Forces." *Proceedings of the ASME IDETC/CIE*, V05AT08A045, DETC2014-35366: pp. 1-10. Buffalo, NY, August 17 – 20, 2014.

[75]   Midha, A., Her, I., and Salamon, B. A., "A Methodology for Compliant Mechanism Design: Part I – Introduction and Large-Deflection Analysis." *Proceedings of the 18th ASME Design Automation Conference*, Advances in Design Automation, DE-Vol.44-2: pp. 29-38, 1992.

[76]   Her, I., Midha, A., and Salamon, B. A., "A Methodology for Compliant Mechanisms Design: Part II – Shooting Method and Application," *Advances in Design Automation, 18th ASME Design Automation Conference*: pp. 39-45. Scottsdale, Arizona, September 1992.

[77]   Ananthasuresh, G. K., "A New Design Paradigm for Micro-Electro-Mechanical Systems and Investigations on the Compliant Mechanism Synthesis," PhD Thesis, University of Michigan, Ann Arbor. 1994.

[78]   Frecker, M. I., Ananthasuresh, G. K., Nishiwaki, S., Kikuchi, N., and Kota, S., "Topological Synthesis of Compliant Mechanisms using Multi-Criteria Optimization," *ASME Journal of Mechanical Design*, Vol. 119: pp. 238-245, 1997.

[79]   Saggere, L., and Kota, S., "Synthesis of Planar, Compliant Four-Bar Mechanisms for Compliant-Segment Motion Generation," *ASME Journal of Mechanical Design*, Vol. 123, No. 1: pp. 535-541, 2001.

[80]   Erdman, A. G., Sandor, G. N., and Kota, S., *Mechanism Design: Analysis and Synthesis*, Vol. 1, Prentice Hall, New Jersey, 2001.

[81]   Midha, A., and Kuber, R., "Closed-Form Elliptic Integral Solution for Initially Straight and Initially-Curved Small-Length Flexural Pivots," *Proceedings of the ASME 2014 International Design Engineering Technical Conferences & Computers and Information in Engineering Conference*, pp. DETC35268: 1-7, 2014.

[82]   Su, H. –J., "A Pseudo-Rigid-Body 3R Model for Determining Large Deflection of Cantilever Beams Subject to Tip Loads", *ASME Journal of Mechanisms and Robotics*, Vol. 1, No. 2, pp. 021008, 2009.

[83]   Bapat, S., Bagivalu Prasanna, P., Midha, A., "A Pseudo-Rigid-Body 3R Model for Determining Large Deflection of Cantilever Beams Subject to Tip Loads", *Manuscript under preparation (2023)*.

[84]   Midha, A., Lodagala, V., Bagivalu Prasanna, P., & Komatireddy, J., "A Primal Treatise of Constant-Force, Compliant Segments, and Mechanisms." *Proceedings of the ASME 2020 International Design Engineering Technical Conferences and Computers and Information in Engineering Conference*, Vol. 10: 44th Mechanisms and Robotics Conference (MR), pp. V010T10A016: 1-12, August 17–19, 2020.

[85]   Fitzpatrick, P. M., *Advanced Calculus*, American Mathematical Society, Providence, RI, 2009.

[86]   Taylor/Maclaurin Series Calculator, https://www.symbolab.com/solver/taylor-maclaurin-series-calculator, July 2022

[87] Euler, L., "Chapter Additamentum 1," *Methodus Inveniendi Lineas Curvas Maximi Minimive Proprietate Gaudentes, Sive Solutio Problematis Isoperimetrici Lattissimo Sensu Accepti*, eulerarchive.org, E065, 1744.

[88] Beer, F. P., Johnston, R. E., Jr., Dewolf, J. T., and Mazurek, D. F., "Columns," *Mechanics of Materials*, The McGraw-Hill Companies, pp. 630-691, New York, NY, 2012.

[89] Nisbett, K. J., and Budynas, R. G., *Shigley's Mechanical Engineering Design*, The McGraw-Hill Companies, New York, NY, 2014.

[90] Edwards, B. T., Jensen, B. D., and Howell, L. L., "A Pseudo-Rigid-Body Model for Initially-Curved Pinned-Pinned Segments used in Compliant Mechanisms," *ASME Journal of Mechanical Design*, Vol. 123(3): pp. 464-472, 2001.

[91] Lodagala, V., Karthik, K., Midha, A., "Limitations in the Use of Small-Length Flexural Pivot in a Pseudo-Rigid-Body Model," *ASME International Design Engineering Technical Conferences and Computers and Information in Engineering Conference, 39th Mechanisms and Robotics Conference*, Vol. 5A, DETC2015-47914: pp. V05AT08A026: 1-11, Boston, MA, August 2-5, 2015.

[92] Lodagala, V., Midha, A., and Krutika, K., "Design Elucidation and Validation of Pseudo-Rigid-Body Model for Small-Length Flexural Pivots in Compliant Mechanisms," *Manuscript under preparation (2023).*

[93] Gere, J. M., *Mechanics of Materials*, Brooks/Cole – Thomson Learning, Belmont, CA, 2004.

[94] Column Buckling, https://mechanicalc.com/reference/column-buckling#intermediate-columns, July 2022.

[95] Midha, A., Schloss, P., Stensby, T., Frankllin, M., Laurentius, P., "Class Notes," ME 261: Engineering Design, Missouri University of Science and Technology, Rolla, Missouri, 2006.

[96] DynaFlex® Canted Coil, https://www.npisprings.com/dynaflex, July 2022.

[97] Erdman, A. G., Sandor, G. N., *Mechanism Design: Analysis and Synthesis*, Vol. 1, 3rd Ed., Prentice Hall, Upper Saddle River, NJ, 1997.

[98] Murphy, M. D., Midha, A., and Howell, L. L. "Methodology for the Design of Compliant Mechanisms Employing Type Synthesis Techniques with Example," *Proceedings of the ASME Mechanisms Conference*, DE-Vol. 70: Mechanism Synthesis and Analysis. pp. 61-66, 1994.

[99]   Midha, A, & Bagivalu Prasanna, P., "Mode Shapes in Compliant Mechanisms, and a Procedure to Identify Appropriate Pseudo-Rigid-Body Model Type," *Proceedings of the ASME 2015 International Design Engineering Technical Conferences and Computers and Information in Engineering Conference*, Volume 5A: 39th Mechanisms and Robotics Conference, V05AT08A024, Boston, Massachusetts, August 2–5, 2015.

[100]   Lodagala, V., and Midha, A., "Canted Spring," *Research Notes*, Missouri University of Science and Technology, Rolla, MO. 09-June-2015.

[101]   Bagivalu Prasanna, P., "Mobility Analysis and Topology Synthesis of Compliant Mechanisms Using Compliance Number and Pseud-Rigid-Body Model (PRBM)," Ph.D. Dissertation, Missouri University of Science and Technology, Rolla, MO, 2022.

[102]   Gallego, J, A., and Herder, J., "Synthesis Methods in Compliant Mechanisms: An Overview." *Proceedings of the ASME IDETC/CIE*. DETC2009-86845. pp. 1-10, San Diego, CA, August 30 – September 2, 2009.

[103]   Her, I., and Midha, A., "A Compliance Number Concept for Compliant Mechanisms, and Type Synthesis," *ASME Journal of Mechanisms, Transmissions and Automation in Design*, Vol. 109 No. 3: pp. 348-355, 1987.

[104]   Paul, B., *Kinematics and Dynamics of Planar Machinery*, Prentice-Hall, Inc., Englewood Cliffs, NJ, 1979.

[105]   Howell, L. L., and Midha, A., "A Loop-Closure Theory for the Analysis and Synthesis of Compliant Mechanisms," *ASME Journal of Mechanical Design*, Vol. 118(1), pp: 121-125, 1996.

[106]   Bapat, S. G., Midha, A., and Koli, A. B., "On a Generalized Approach for Design of Compliant Mechanisms Using the Pseudo-Rigid-Body Model Concept," *Proceedings of the IMECE,* IMECE2014-38788: pp. V014T06A001: 1-11, Montreal, Quebec, Canada, November 14-20, 2014.

[107]   Midha, A., and Lodagala, V., "Constant-Force Applications: Solving Indeterminacy in Structures," *Research Notes*, Missouri University of Science and Technology, Rolla, MO, June 2019.

[108]   Miyamoto, A., "Minimizing Indeterminacy by Incorporating Constant-Force Mechanisms into Simply-Supported Structures," M.S. Thesis, Missouri University of Science and Technology, Rolla, MO. *Manuscript under preparation (2023).*

[109] Grujicic, M., Pandurangan, B., Arakere, G., Bell, W. C., He, T., Xie, X., "Seat-Cushion and Soft-Tissue Material Modeling and a Finite Element Investigation of the Seating Comfort for Passenger-Vehicle Occupants," *Elsevier Journal of Materials and Design*, Vol. 30: pp. 4273-4285, 2009.

[110] Siefert, A., Pankoke, S., Wolfel, H.-P., "Virtual Optimisation of Car Passenger Seats: Simulation of Static and Dynamic Effects on Drivers' Seating Comfort," *Elsevier Journal of Industrial Ergonomics*, Vol. 38: pp. 410-424, 2008.

VITA

Vamsi Lodagala was born in Khammam, India, and raised in Visakhapatnam, India. He received a Bachelor of Technology (B.Tech) degree in Mechanical Engineering from MVGR College of Engineering, Jawaharlal Nehru Technological University – Kakinada, India, in June 2012. He moved to the USA after his bachelor's to pursue a master's degree in the Department of Mechanical Aerospace Engineering (MAE) at Missouri University of Science and Technology, Rolla, MO, in August 2012. He converted his degree program to a Ph.D. program in January 2016 upon his research advisor's offer. He worked as a graduate teaching assistant from the Spring semester of 2013 and as a co-lead coordinator from the Fall semester of 2016 for the capstone senior design course (ME 4761) till the Spring of 2022 in the Department of Mechanical and Aerospace Engineering. He received the AMAE (Academy of Mechanical and Aerospace Engineers) Senior Design Leadership Award in October 2021 for his sustained and exemplary contributions to the course. He was awarded a Master of Science in Mechanical Engineering in July 2022 and a Doctor of Philosophy in Mechanical Engineering in May 2023 from the Missouri University of Science and Technology, Rolla, MO.